AN EXPERIMENTAL STUDY OF THE FLOW AROUND SURFACE-MOUNTED RECTANGULAR FLAT PLATES

A Thesis Submitted to the

College of Graduate and Postdoctoral Studies

in Partial Fulfillment of the Requirements

for the degree of Master of Science

in the Department of Mechanical Engineering

University of Saskatchewan

Saskatoon

By

Everardo Montes Gómez

Permission of Use

In presenting this thesis in partial fulfillment of the requirements for a Postgraduate degree from the University of Saskatchewan, I agree that the Libraries of this University may make it freely available for inspection. I further agree that permission for copying of this thesis in any manner, in whole or in part, for scholarly purposes may be granted by the professor who supervised my thesis work or, in his absence, by the Head of the Department or the Dean of the College in which my thesis work was done. It is understood that any copying or publication or use of this thesis or parts thereof for financial gain shall not be allowed without my written permission. It is also understood that due recognition shall be given to me and to the University of Saskatchewan in any scholarly use which may be made of any material in my thesis.

Requests for permission to copy or to make other uses of materials in this thesis in whole or part should be addressed to:

Head of the Department of Mechanical Engineering
College of Engineering
University of Saskatchewan
57 Campus Drive
Saskatoon, Saskatchewan S7N 5A9
Canada

Dean of the College of Graduate and Postdoctoral Studies
116 Thorvaldson Building
University of Saskatchewan
110 Science Place
Saskatoon, Saskatchewan S7N 5C9
Canada

Disclaimer

Reference in this thesis to any specific commercial products, process, or service by trade name, trademark, manufacturer, or otherwise, does not constitute or imply its endorsement, recommendation, or favoring by the University of Saskatchewan. The views and opinions of the author expressed herein do not state or reflect those of the University of Saskatchewan, and shall not be used for advertising or product endorsement purposes.

Abstract

An experimental study was carried out to study the mean wake of a surface-mounted finite-height three-dimensional rectangular flat plate. Four different flat plates were used in the experiments, with aspect ratios of AR = 0.5, 1, 2 and 3. For each aspect ratio, the incidence angle α was varied from $\alpha = 0°$ to 90° in increments as low as 5°. The experiments were conducted in a low-speed wind tunnel, at a Reynolds number of Re = 3.8×10^4 and with a boundary layer thickness of δ/W = 1.14 (where W is the width of the plate). Time-averaged velocity measurements in the wake of the plate were made with a seven-hole pressure probe. Wake measurements were performed in the vertical cross-stream plane (normal to the freestream) at x/W = 6 downstream of the plate, and in the vertical plane on the wake centreline (parallel to the freestream). The data were compared with results from similar experiments for surface-mounted finite-height square prisms and cylinders at similar flow conditions and of similar aspect ratios.

When the flat plate is located normal to the flow, with $\alpha = 0°$, the streamwise length of the mean recirculation zone and the strength of the downwash on the wake centreline both increase with AR. The recirculation zone of the flat plate is longer than those of the finite-height square prism and the finite cylinder, owing to differences in the body shape and flow separation.

Flat plates of AR = 0.5 and 1 have a single pair of time-averaged counter-rotating streamwise vortex structures in the wake, referred to as ground plane vortex structures. As the incidence angle increases, these vortex structures become asymmetric and of different size, strength, and location. The streamwise vortex produced by the leading edge of the plate located further upstream overtakes the opposing one and at sufficiently high at α starts behaving like a wing-tip vortex.

Flat plates of AR = 2 and 3 have two pairs of time-averaged counter-rotating streamwise vortex structures, with a set of tip vortices and a set of ground plane vortices. Some additional induced vorticity is also seen for the flat plate of AR = 3. At high incidence angles, the wakes of these flat plates have a single wing-tip vortex type structure.

A comparison between the wakes of the flat plate of AR = 0.5 and a finite square prism of AR = 0.5 showed that induced vorticity, with opposite rotation to the ground plane vortices near the centerline, was only present for the square prism. This feature is attributed to the interaction of the main vortex structures with the top x-y face (free end) of the afterbody. A comparison between the wakes of the flat plate of AR = 3 and a finite square prism of AR = 3 showed a dual wake boundary peak for the square prism while the flat plate shows a single wake boundary. The differences are attributed to the presence of the afterbody on the square prism. Both wakes denote a different behaviour when varying α. The finite square prism shows its largest asymmetry between α = 10º - 15º and regaining its symmetric features at α = 45º while the flat plate shows an increasingly asymmetric wake behaviour up to α = 90º.

Acknowledgements

The amount of gratitude owed to my supervisor, Dr. David Sumner, cannot be fully expressed in words. Your direction, extensive knowledge on fluid mechanics, thoroughness and motivation were imperative for the conclusion of this program, you are an inspiration and an example on how one should conduct professionally and most importantly as a human being. You went above and beyond helping me to pursue my academic goals and for that I will be grateful forever.

I would also like to thank Shawn Reinink for his time, knowledge, dedication and troubleshooting skills with the experimental setup which were imperative in the prompt fulfillment of this thesis despite the unexpected setbacks due to the ongoing pandemic. The help from Engineering Shops on the development of the flat plate models is very much appreciated.

A special thank you is owed to the members of my advisory committee, Dr. Donald Bergstrom and Dr. Jim Bugg, who accompanied me throughout my entire journey in this institution with their lectures, support, observations and invaluable advice.

I want to thank Barbara da Silva for her shared knowledge and friendship throughout my postgraduate degree as well as the experimental data she provided for the fulfillment of this thesis. The experimental data provided by Dylan Hahn are very much appreciated as well.

Finally, I would like to thank the Department of Mechanical Engineering and the Natural Sciences and Engineering Research Council of Canada (NSERC) for the financial support throughout this program.

Dedication

I don't think you'd understand
In the quest to be a man
You start to learn you need your family
It wasn't for them, I'd be way closer to insanity

- Rest easy Mac Miller.

I want to dedicate this dissertation to my mother Magdalena and my father Everardo, the two people whose love and support have always been unconditional no matter what I do.

Your immense efforts and guidance throughout my whole life, the sacrifices you've made in order to give me the best opportunities and education have brought me to where I am today. I will always remember that.

I am the outcome of your work, my actions and character are a reflection of your teachings. I hope I made you both proud. I love you mom and dad.

I also want to give a little shout out to my little sister Rebeca, I hope by the time you read this you will have found your path as I have found mine and never look back. You are the kindest most caring person I know and you will always have a special place in my heart. I love you sister.

And last but not least, the love of my life Aileen. I fell for you the moment I saw you. Everything happens for a reason, time will give me perspective. I love you forever, no matter where life takes us I will always be with you.

Table of Contents

Nomenclature

AR	aspect ratio
C_D	mean drag force coefficient
C_L	mean lift force coefficient
C_M	mean aerodynamic moment coefficient
C_N	mean normal force coefficient
C_P	mean pressure coefficient
F_D	mean drag force [N]
F_L	mean lift (side) force [N]
F_N	mean normal force [N]
f	vortex shedding frequency [Hz]
H	height [mm]
L_r	length of recirculation region
Mx	mean aerodynamic moment about the *x*-axis [N·m]
My	mean aerodynamic moment about the *y*-axis [N·m]
Mz	mean aerodynamic moment about the *z*-axis [N·m]
P_o	stagnation pressure [kPa]
P_∞	freestream static pressure [kPa]
q_∞	freestream dynamic pressure [Pa]
R	ideal gas constant [J/kg·K]
Re	Reynolds number
S	constant in Sutherland's law [K]
St	Strouhal number
t	thickness [mm]
t/W	thickness ratio
T_∞	freestream temperature [K]
T_o	constant in Sutherland's law [K]
U_∞	freestream velocity [m/s]
U_h	velocity of the approach flow at windbreak height H [m/s]
U_τ	friction velocity [m/s]

u	mean streamwise velocity component [m/s]
$u/U_{\infty\ \mathrm{min}}$	minimum relative streamwise velocity
v	mean transverse velocity component [m/s]
W	width [mm]
w	mean vertical (wall-normal) velocity component [m/s]
x	streamwise coordinate [mm]
y	transverse coordinate [mm]
z	vertical (wall-normal) coordinate [mm]

α	incidence angle [°]
β	inclination angle [°]
δ	boundary layer thickness [mm]
δ/W	boundary layer thickness ratio
δ^*	displacement thickness [mm]
δ^*/θ	shape factor
θ	momentum thickness [mm]
μ_∞	freestream dynamic viscosity [N·s/m^2]
μ_o	constant in Sutherland's law [N·s/m^2]
ρ_∞	freestream density [kg/m^3]
ω_x	mean vorticity component about the *x*-axis [s^{-1}]
ω_y	mean vorticity component about the *y*-axis [s^{-1}]
ω_z	mean vorticity component about the *z*-axis [s^{-1}]

Chapter 1 – Introduction

1.1 Motivation

Flow around a simple rectangular flat plate (Fig. 1.1) is encountered in many engineering applications. Flat plates immersed in flow are used for improving the rate of heat transfer in solar chimneys [1] and as heat exchanger fins [2] [3] [4] [5] where they lead to improved thermal mixing. They can be used as windbreaks [6] and shelterbelts [7], reducing wind speed to avoid soil erosion or enhancing wind turbine power [8]. As vortex generators [2] and turbulence generators [2] [9], flat plates can be used to alter the flow around vehicles, improving their aerodynamic performance, or as spoilers on an airfoil [10]. These are some of the examples of their implementation and are some of the reasons why the study of the flow around this particular body has drawn attention from the scientific community.

The aerodynamic behaviour of a flat plate oriented normal to the flow classifies this shape as a bluff body, a category of aerodynamic shapes that includes square prisms [11] [12] and cylinders [13]. The flow separation that occurs along the edges of the flat plate results in a large wake behind the plate and a high drag coefficient, which are characteristics it shares with other bluff bodies. However, when varying the incidence angle α of a flat plate, from normal to the flow (α = 0º) to parallel to the flow (α = 90º), the effects of flow separation become increasingly less important and the plate eventually behaves as a streamlined body similar to an airfoil; this is a unique feature of flat plates compared to other bluff bodies. When this transition happens, the skin-friction plays a greater role in determining the fluid forces experienced by the flat plate, while the influence of the pressure being applied to the now “streamlined body” decreases to some extent.

At a sufficiently high Reynolds number, the shear layers that separate from the edges of the flat plate enclose a recirculation region downstream of the flat plate. Periodic formation and shedding of vortices into the wake, referred to as Karman vortex shedding, may occur. The type of vortices shed downstream and their frequency can depend on the flow regime, the boundary layer thickness (for the case where the plate is mounted normal to a ground plane), the relative dimensions (height, width, thickness) of the bluff body, and the presence of an “afterbody” or lack thereof. The afterbody refers to the downwind or rear shape contour of a bluff body, extending from the centre of the body to the rearmost point. The afterbody shape may be streamlined, curved, triangular, or square in shape. The afterbody helps direct separated flow into the wake, influences the interaction of the separated shear layers, and has an effect on the body's drag coefficient, vortex shedding frequency, and the flow and pressure in the near wake recirculation zone. A familiar example of an afterbody is the streamlined "boat tail" shape at the back of a boat or vehicle. From a bluff body aerodynamics perspective, flat plates are unique in that they do not have an afterbody. The effects of this particular characteristic have not been widely studied and are of fundamental interest to understand the forces experienced by a bluff body and the behaviour of the wake.

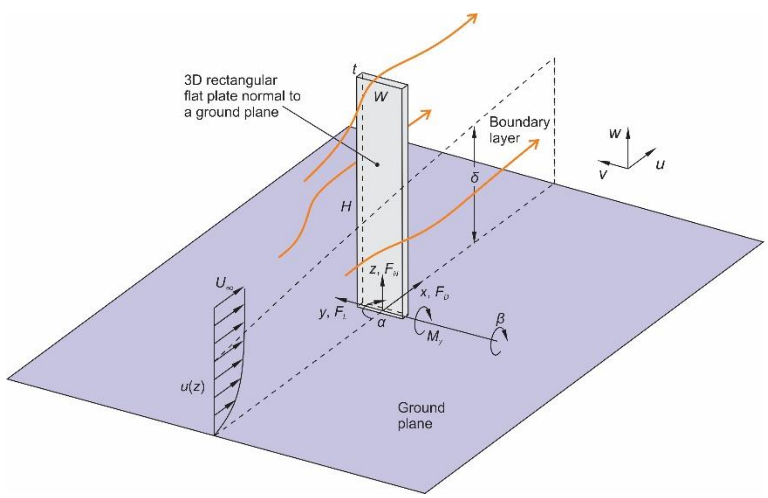

Figure 1.1. Flow around a three-dimensional (3D) rectangular flat plate (of height H, width W, and thickness t) mounted normal to a ground plane, where δ is the boundary layer's thickness, M_y is the bending moment, U_∞ denotes the freestream velocity, and F_N, F_D and F_L are the mean normal force, drag force and lift (side) force, respectively. The mean streamwise velocity profile in the boundary layer is $u(z)$. The coordinate directions x, y, and z, and the velocity components u, v, and w, are in the streamwise, cross-stream (transverse), and vertical (wall-normal) directions, respectively. Two angles are shown: the incidence angle α indicating rotation about the z axis, and the inclination angle β indicating rotation about the y axis.

This thesis is expected to contribute to a better understanding of the behavior of the flow around three-dimensional (3D) rectangular flat plates mounted normal to a ground plane (Fig. 1.1). There are few systematic experimental research studies of this bluff body flow, particular those that have considered the effects of the incidence angle α and the plate's aspect ratio $AR = H/W$ (where H is the height of the plate and W is its width), and how they affect the mean wake.

1.2 Objectives and Approach

The present research is focused on the study of the flow around a thin three-dimensional (3D) rectangular flat plate of height *H*, width *W*, and thickness *t* mounted normal to a ground plane (Fig. 1.1). The coordinate directions (shown in Fig. 1.1) are defined as follows: *x* (streamwise), *y* (cross-stream or transverse), *z* (vertical or wall-normal). The origin is at the half thickness of the flat plate where it meets the ground plane. An experimental approach is adopted using wind tunnel testing.

The objectives of the research are:

- To show how the aspect ratio *AR* and incidence angle α affect the mean wake of the plate.
- To compare the wakes of the flat plates to those of surface-mounted finite-height cylinders and square prisms, in order to determine some effects of afterbody shape on the mean wake of surface-mounted finite-height bluff bodies.

The main focus of the experimental investigation comprises measurements of the time-averaged (mean) velocity field at arbitrary distances downstream of the flat plate with the purpose of determining the wake structure and behaviour. This is primarily achieved in the form of two-dimensional (2D) mean velocity fields at various streamwise locations x/W downstream of the plate (where *x* is the streamwise coordinate measured from the location of the plate, see Fig. 1.1.). From these velocity fields, the mean streamwise vortex structures can be identified. By systematically changing *AR* and α, their effects on the wake can be determined. Table 1.1 summarizes the range of parameters within the scope of the research program.

In the present research, the aspect ratio of the plate is varied by keeping the plate width *W* constant while changing the plate's height *H*. Plates of AR = 0.5, 1, 2, and 3 are studied. A similar *AR* domain has been previously tested with finite-height square prisms [11] [12] [14] [15] and finite-height cylinders [13] under similar flow conditions. This study is expected to work as a comparison with some of the previous works in order to determine differences that may arise between the different bluff bodies.

Table 1.1 Summary of the parameters used in the present research.

Parameter	**Range**
Aspect Ratio, *AR*	0.5, 1, 2, 3
Incidence Angle, α	0° to 90° ± 0.25° (the specific values of α are found in Appendix A)
Reynolds Number, Re	$3.8 \pm 0.1 \times 10^4$
Boundary Layer Thickness, δ/W	1.14 ± 0.1
Inclination Angle, β	0°

Another relevant characteristic is the thickness ratio t/W of the flat plate. The thickness ratio needs to be sufficiently small such that the body behaves as a thin flat plate rather than a thicker rectangular prism. However, experimentally, the plate must be sufficiently thick for structural rigidity, so the plate will not bend or vibrate. In the present research, a single value of $t/W = 1.5$ is used for all of the plates. The dimensions of the flat plates were selected in order to avoid the effects of blockage in the wind tunnel and to achieve similar experimental conditions as in [11] and [12].

The Reynolds number for a 3D rectangular flat plate is defined based on the width of the plate W, as $\mathrm{Re} = \rho_\infty U_\infty W/\mu_\infty$, where ρ_∞ is the air density, U_∞ is the freestream velocity of the incoming air flow, and μ_∞ is the air's dynamic viscosity. Although the Reynolds number may have an influence on the resulting flow field, its effects are relatively small because of the fixed separation points along the edges of the plate, and all of the experiments in the thesis research are conducted at a single value of Reynolds number, $\mathrm{Re} = 3.8\times10^4$; this approach is consistent with previous work on surface-mounted bluff bodies conducted by the research group [11] [12].

The plate may be rotated around the z-axis (see Fig. 1.1) at an incidence angle α, where $\alpha = 0°$ corresponds to the area of the plate being oriented normal to the flow. The plate may also be tilted forward or backward about the y-axis (see Fig. 1.1) at an inclination angle β, where $\beta = 0°$ corresponds to the plate oriented vertical and normal to the ground plane. In this research, only the incidence angle α is varied, from $\alpha = 0°$ to 90°, while the inclination angle is fixed at $\beta = 0°$.

As shown in Fig. 1.1, a boundary layer (with a mean streamwise velocity profile of $u(z)$) is formed on the ground plane with a thickness δ at the location of the plate. In the present research, a naturally developing and relatively thin flat-plate turbulent boundary layer, originating from the leading edge of the wind tunnel's test section ground plane, is used for all of the experiments. This ensured a fully developed turbulent flat-plate (ground plane) boundary layer at the location of the flat plate (test models) with a nearly zero pressure gradient.

The ratios of δ/W and δ/H are known to influence the flow around a surface-mounted finite-height cylinders and prisms, and are therefore expected to have similar effects on surface-mounted flat plates. These effects include a reduction in the mean drag force coefficient C_D, mean normal force coefficient C_N, and Strouhal number St with thicker boundary layers due to a larger portion of the bluff body being surrounded by a lower-momentum flow within the boundary layer [16]. In the present study, the value of $\delta/W = 1.5$ is fixed for all of the experiments while the value of δ/H varies with the different flat plates, similar to the studies of finite-height square prims by Unnikrishnan et al. [11] and Sumner et al. [12].

A complete description of the experimental plan for the research can be found in Appendix A.

1.3 Outline of the Thesis

The present thesis is divided into five main chapters. Chapter 2 reviews the available literature on the different flat plate set-ups (Section 2.2). This includes a more detailed focus on the 3D flat plate that is the emphasis of the present thesis research, along with a brief explanation of important flow parameters for a bluff body, such as the mean drag coefficient C_D (Section 2.3) and Strouhal number St (Section 2.4). This is followed by a brief discussion on the relation between the afterbody of a bluff body and the wake (Section 2.5). A brief review on the effects of the incidence angle is presented in Section 2.6.

Chapter 3 details the wind tunnel setup (Section 3.2), the flat plate models used in the experiments (Section 3.3), as well as the instruments used for measurements and the methodology for data collection (Section 3.4). An uncertainty analysis is presented in Section 3.5 while the boundary layer measurements and calculations are described in Section 3.6.

Chapter 4 comprises a discussion and analysis of the experimental data starting with a comparison of the experimental conditions (Re and δ/W) of previous work with the current research (Section 4.1). Section 4.2 contains an analysis on the studied flat plates (AR = 0.5, 1, 2, and 3) normal to the flow ($\alpha = 0°$) divided into measurements made in the vertical symmetry (x-z) planes (Section 4.2.1) and the vertical cross-stream (y-z) planes (Section 4.2.2). Section 4.3 discusses the results made in the vertical cross-stream (y-z) planes with the plates at a non-zero angle of incidence α and compares them with results for a finite cylinder and a finite square prism.

Chapter 5 includes a summary of the conclusions and contributions of the present work (Section 5.1). It also lists some recommendations and possible paths the current research could take (Section 5.2).

Chapter 2 – Literature Review

2.1 Introduction

Flat plates can be classified as both two-dimensional (2D) and three-dimensional (3D). For the 2D flat plate, the main distinction is a characteristic dimension that is considerably greater compared to the other dimension such that the flow around one end of the plate does not "communicate" or interfere with the flow around the other end of the flat plate. This plate is often referred to as an "infinite" plate, where the flow at the centre of the plate (farthest from the two edges) is purely 2D and the end conditions do not appreciably influence the flow over most of the plate. In a wind tunnel experiment, a 2D flat plate would be one that spans the entire width of the wind tunnel test section, such that no flow occurs around the ends of the plate.

For the 3D flat plate, the ends of the plate are either sufficiently close to each other, or close enough to the centre of the plate, such that their influence is felt everywhere in the flow. Flow now occurs around the ends of the plate.

The width-to-height ratio W/H (the reciprocal of the aspect ratio $AR = H/W$) can be used as a guideline to determine whether the plate will behave as a 2D or 3D flat plate. Fail et al. [17] conducted a series of experiments involving 3D flat plates in uniform flow where they varied the W/H ratio from 1 to 20 and also tested with a plate of $W/H = 29$. They concluded that the transition from 3D to 2D flow behaviour occurred for $W/H > 20$. Several studies have defined a 2D flat plate at lower aspect ratios: Fage et al. [18] used a trapezoidal 2D flat plate of $W/H = 14.1$, Sakamoto et al. [19] [20] used a flat plate of $W/H = 12$ for their 2D plate experiments, while Mazharoglu [21] used a 2D flat plate of $W/H = 16.6$. The current literature does not agree on an AR where the change from 2D to 3D behaviour occurs. Fail et al. [17] suggested in their study that a flat plate of $AR = 10$ is the largest body to noticeably present three-dimensional features, with an argument based on a drastic increase in the drag coefficient, a significant drop in base pressure, and a drastic reduction in size of the recirculation zone or "bubble" formed behind the flat plate on any flat plate of $W/H > 10$. That being said, the domain of that study presented a big gap from $W/H = 10$ to $W/H = 20$ meaning further wake analysis over a wider range of flat plates could be of interest for future research in order to establish this definition more accurately.

2.2 Flat Plate Configurations

Due to the different applications and other fundamental differences, a classification of rectangular flat plates and the flow around them is necessary for the present study. The flow around a thin rectangular flat plate takes on four different configurations, types A through D, that are described in the following subsections.

2.2.1 Flat Plate Type A

Flat plate type A is a three-dimensional (3D) rectangular flat plate in a uniform flow (Fig. 2.1) where the flow can pass around all four sides. Applications include flow around road signs [22].

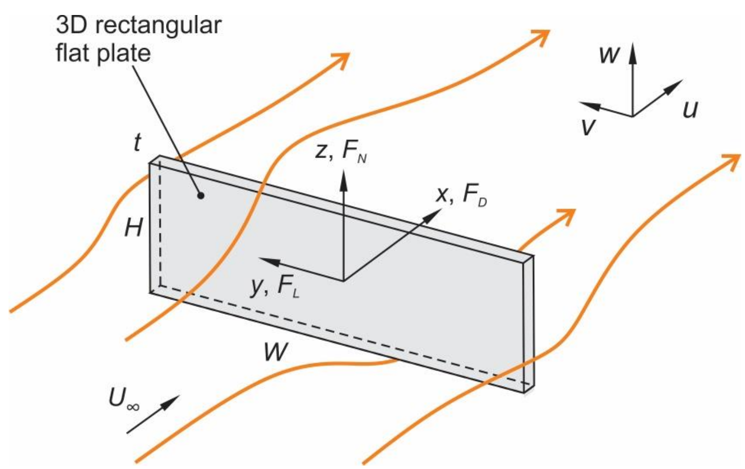

Figure 2.1. Flat plate type A: a three-dimensional (3D) rectangular flat plate in a uniform flow, where the flow can pass around all four sides of the plate.

A good example of this configuration is the work by Fail et al. [17] with a series of low-speed wind tunnel experiments on the wake characteristics of a flat plate normal to an air stream.

2.2.2 Flat Plate Type B

Flat plate type B is a two-dimensional (2D or infinite) rectangular flat plate in a uniform flow (Fig. 2.2) where $W >> H$ and the flow can pass only above or below the plate. Applications involving the type B flat plate include flow around long-span structural elements, such as I-beams used in building construction [10] [20].

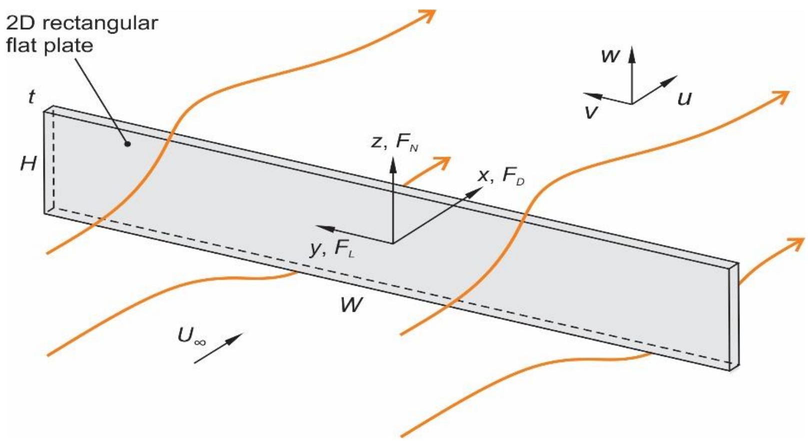

Figure 2.2. Flat plate type B: a two-dimensional (2D) infinite flat plate in a uniform flow, where the flow can only pass over the top and bottom sides of the plate.

This type of plate was also used by Fail et al. [17] to study vortex shedding from the plate, where the vortex shedding frequency f is given in dimensionless form by the Strouhal number $St = fW/U_\infty$. Fage et al. [18] examined the vortex shedding frequency and strength at the edges of a similarly arranged plate, but varied the inclination angle β.

2.2.3 Flat Plate Type C

Flat plate type C is also a two-dimensional (2D or infinite) rectangular flat plate, but differs from type B by being mounted normal to a ground plane, where the plate is fully or partially immersed in the boundary layer on the ground plane (Fig. 2.3). Here, $W >> H$ but because of the ground plane the flow can only pass over the top of the plate. Applications involving a type C flat plate include flow over a wall [23], fence [20] [24], or shelterbelt [7].

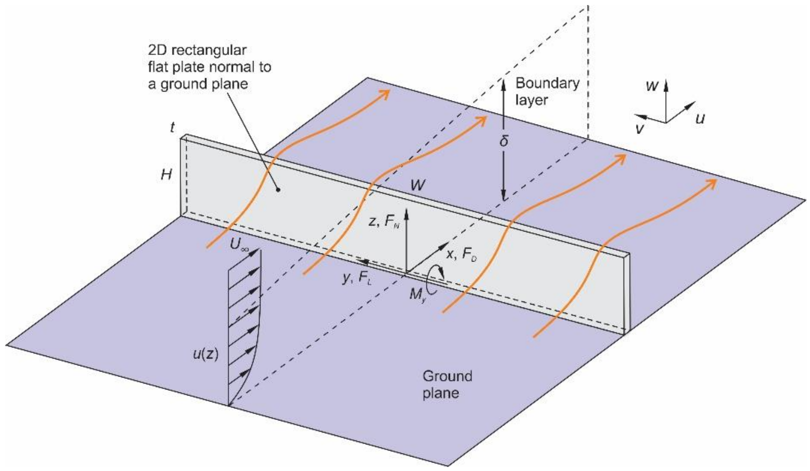

Figure 2.3. Flat plate type C: a two-dimensional (2D or infinite) rectangular flat plate normal to a ground plane, where the flow can only pass over the top edge of the plate.

Sakamoto et al. [19] conducted research with this configuration towards the study of the pressure distributions on a flat plate and the relation between the height of the plate and the drag force. They described a front separation bubble occurring upstream due to an adverse pressure gradient followed by flow separation on the top edge of the flat plate with a recirculation region downstream of the plate. They attributed a significant drag coefficient (C_D) reduction due to this front separation bubble compared to a 2D flat plate in uniform flow (type B, Fig. 2.2). Two years later [20] they used the same plates to visualize the effects of the inclination angle β and the characteristics of the smooth boundary layer on the pressure forces on the plate. They discovered that the "law of the wall" was applicable for a select range of boundary layer thicknesses and proposed a method to calculate the pressure distributions on the front of the plate involving four coefficients that can only be determined with problem-specific empirical information.

2.2.4 Flat Plate Type D

Flat plate type D is a three-dimensional (finite-height) rectangular flat plate mounted normal to a ground plane, where the plate is fully or partially immersed in the boundary layer on the ground plane, and where the flow can go over the top and around the sides of the plate. This type of plate is the focus of the present thesis research and a schematic was shown earlier in Fig. 1.1. Applications include vortex generators, turbulence generators, heat exchanger fins, boundary layer control tabs, etc.

2.2.5 Overview of Studies

A summary of some studies of the flow around rectangular flat plates is presented in Table 2.1. Most of the information available in the literature concerns the study of 2D (infinite) plates mounted normal to a ground plane (type C, Fig. 2.3) and oriented normal to the freestream like Sakamoto et al. [19]. There are some experimental studies that provide data on plates that are inclined (β) towards the downstream direction, such as by Sakamoto et al. [20]. Some of the more recent articles mostly use computational fluid dynamics (CFD) [3] [5] [25] or have studied flexible plates, to analyze their properties as heat transfer enhancers [2], or flow-induced motions of flexible plates [9] [26]. Studies by Yamada et al. [27] and Yamada et al. [28] viewed vortex structures around a 3D flat plate normal to a ground plane (type D, Fig.1.1), but what is generally lacking on the subject are the effects of the aspect ratio ($AR = H/W$) and the incidence angle (α) on the behavior of the flow around a solid flat plate. Few measurements have been made revealing the appearance of the wake behind this body. Sakamoto et al. [10] showed that in addition to the aspect ratio, the relative thickness of the boundary layer on the ground plane (δ/H) is also a key influencing parameter for the flow over 3D flat plates.

2.3 Drag Coefficient

For type D flat plates specifically, i.e., three-dimensional rectangular flat plates mounted normal to the ground plane, the mean drag coefficient C_D is defined as

$$C_D = \frac{F_D}{\frac{1}{2}\rho_\infty (U_\infty)^2 HW}, \tag{2.1}$$

where F_D is the mean drag force and the frontal area of the plate HW is used as the reference area. The drag coefficient is dependent on the aspect ratio $AR = H/W$, the thickness ratio t/W, the Reynolds number Re, and the relative thickness of the boundary layer on the ground plane at the location of the plate δ/H. An example of the sensitivity of C_D to AR and δ/H is shown in Fig. 2.4 for the case where the plate is normal to the flow, from the study by Sakamoto et al. [10]. This figure shows a change in slope in the C_D data at an aspect ratio of $AR = 0.2$.

Table 2.1 Summary of selected experimental studies of the flow over a rectangular flat plate.

Study	Type of plate	*t* [mm]	*W* [mm]	*H* [mm]	AR = *H*/*W*	*t*/*W*
Yang , Ting, Ray [2]	3D flat plate (type d)	0.1	12.70	25.4	2	0.008
Yang , Ting, Ray [2]	3D flat plate type d)	0.1	12.70	38.1	3	0.008
Yang , Ting, Ray [2]	3D flat plate (type d)	0.1	12.70	50.8	4	0.008
Fail, Lawford, and Eyre [17]	2D flat plate (type b)	3.3	914.4	31.5		0.004
Fail, Lawford, and Eyre [17]	3D flat plate type a)	3.3	567.7	28.44	0.05	0.006
Fail, Lawford, and Eyre [17]	3D flat plate (type a)	3.3	401.3	40.1	0.1	0.008
Fail, Lawford, and Eyre [17]	3D flat plate (type a)	3.3	285	56.9	0.2	0.012
Fail, Lawford, and Eyre [17]	3D flat plate (type a)	3.3	179.6	90	0.5	0.018
Fail, Lawford, and Eyre [17]	3D flat plate (type a)	3.3	127	127	1	0.026
Sakamoto [20]	2D flat plate (type c)	6	600	50		0.01
Sakamoto [19]	2D flat plate (type c)	6	600	50		0.01
Okamoto [29]	3D flat plate (type d)	Varied	40, 70	40, 70	1	0.06, 0.1
Sakamoto [10]	3D flat plate (type d)	2.5	5 to 300	10 to 30	0.1 to 2	0.008 to 0.5
Sakamoto [10]	3D flat plate (type d)	unknown	1 to 400	8 to 80	0.2 to 8	
Mazharoglu [21]	2D flat plate (type b)	6	30	500		0.2
A.M. Hamed [5]	3D flat plate (type d)	1.6	28	40	0.70	0.057
Tobin N. [6]	3D flat plate (type d)	3	60,120,180,240	12	0.2, 0.1, 0.06, 0.05	.05,.025,.180,.012
Fage A & Johansen [18]	2D flat plate (type b)	4.5-sharp	2133	151.13		.0021-sharp edge
Jin & Kim [26]	3D flat plate (type d)	0.125	10	20	0.5	0.0125
Jin & Kim [26]	3D flat plate (type d)	0.5	60	240	0.260	0.008

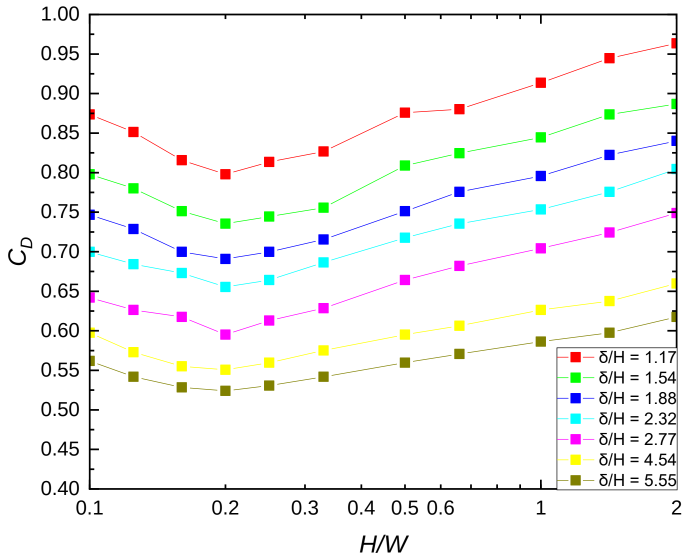

Figure 2.4. Relation between the mean drag coefficient C_D and the aspect ratio $AR = H/W$ for various boundary layer thicknesses δ/H, for a 3D rectangular flat plate mounted normal to a ground plane (type D). Data points are from the study of Sakamoto et al. [10] for $\alpha = 0°$ and $\beta = 0°$.

2.4 Vortex Shedding

Periodic vortex shedding may occur from all four configurations of flat plates (types A, B, C, and D), although this process will be different for the type C flat plate where there is only a single shear layer. For type A, depending on the ratio of H/W, two vortex shedding processes could occur downstream of the body, both with particular frequencies. Fail et al. [17] relate the lower of the two frequencies with the shorter dimension and the higher frequency with the larger dimension.

For type D flat plates, which is the focus of the present research, only a single vortex shedding frequency f will occur. The frequency is represented by the dimensionless Strouhal number based on the width of the plate W.

$$St = \frac{fW}{U_\infty} \tag{2.2}$$

Sakamoto et al. [10] found a relation between the aspect ratio $AR = H/W$ and the Strouhal number where St decreases constantly up to a change in slope with an upwards trend at $AR = H/W = 1.42$

as seen in Fig. 2.5. The same figure also reveals how *St* is a function of the relative thickness of the boundary layer δ/H.

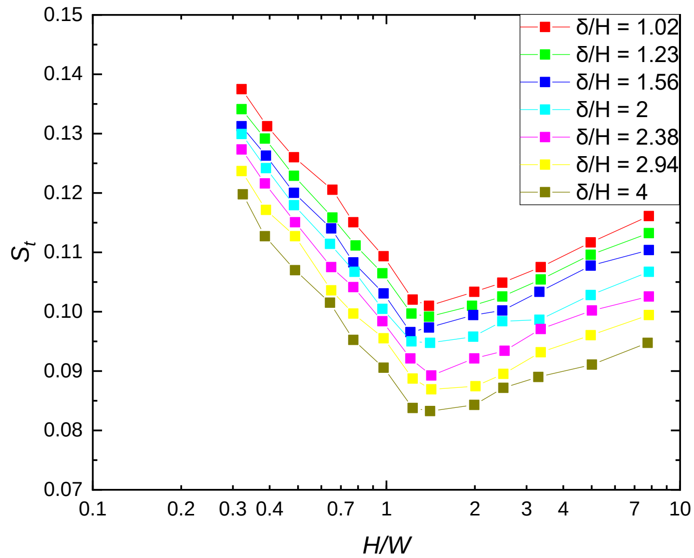

Figure 2.5. Relation between the Strouhal number St and the aspect ratio $AR = H/W$ for various boundary layers thicknesses δ/H, for a 3D rectangular flat plate mounted normal to a ground plane (type D). Data points are from the study of Sakamoto et al. [10] for $\alpha = 0°$ and $\beta = 0°$.

They also state that there are two types of vortices that are formed behind a 3D flat plate normal to the freestream, the von Karman type for $AR \geq 1.4$ while arch-type vortices develop for smaller aspect ratios. This suggests the existence of a "critical aspect ratio", where there is a change in the wake structure and the nature of the vortex shedding, similar to what is found for finite cylinders and square prisms.

2.5 The Contribution of the Afterbody on the Characteristics of the Wake

The role of the afterbody shape in determining the characteristics of the wake of surface-mounted finite-height bluff bodies is not well understood. A flat plate, because it is very thin, has no afterbody and therefore is of fundamental importance and a reference case to compare to finite cylinders [13] [16] and finite-height prisms [11] [12] [14] [15].

Okamoto [29] partially addresses this topic by comparing the flow past bluff bodies of similar squared sections, meaning a constant $AR = 1$. In this case, what changed was the thickness *t*, meaning t/W varied as 0.06, 0.1, 0.5, 1.0 and 1.5. His experiments included measurements of the velocity distributions, static pressures and turbulence intensities for the flow past the bluff bodies, as well as the calculation of the drag and lift coefficients. The results showed a slight decrease in the drag coefficient with an increasing t/W that is more noticeable from 0.5 to 1.5, as shown in Fig. 2.6. He also pointed out the pressure acting on the front face of the flat plate is at its highest on the centre of the flat plate, while on the back the pressure is nearly constant along the flat plate.

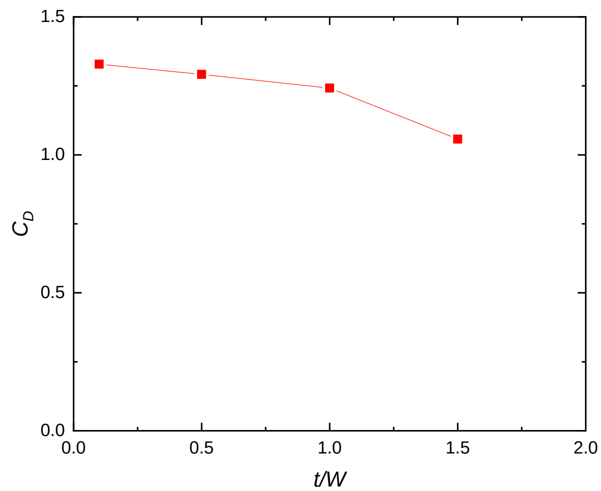

Figure 2.6. Relation between drag coefficient C_D and the thickness-to-width ratio t/W for a 3D finite rectangular prism normal to the ground [29].

Okamoto [29] also looked at the recirculation region behind the body. The outer boundary of this region is the streamline separated from the edge of the plate that reattaches onto the ground plane, forming a region where the fluid recirculates. The length of the recirculation region, which is the distance from the separation to the reattachment, decreases as t/W increases (see Fig. 2.7). What was missing from his paper was the exact transition at which significant differences arise due to the lack of an afterbody, in order to clearly differentiate a flat plate from a prism, given that it focused mainly on the bodies with a t/W of 0.5, 1.0 and 1.5.

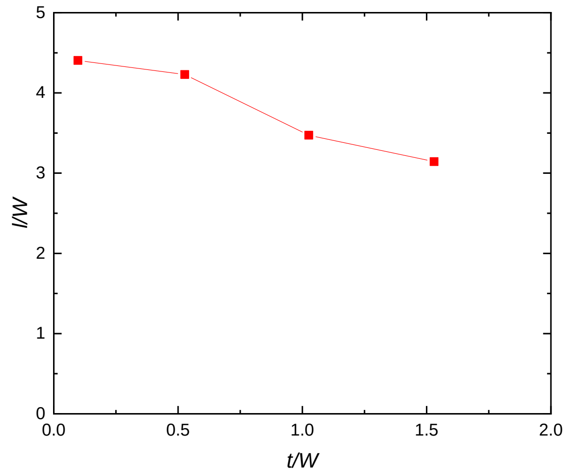

Figure 2.7. Length of the recirculation region (l) for various thickness-to-width ratios t/W for a 3D finite rectangular prism normal to the ground [29].

2.6 Incidence Angle

The effect of incidence angle (α) on the flow around rectangular flat plates has also not been extensively discussed. Tobin et al. [6] provides some information on the impact of the incidence angle and aspect ratio on the wake of a 3D surface-mounted flat plate. They defined a wake moment coefficient

$$C_M = \frac{M}{\frac{1}{2}\rho_\infty W H^2 U_h^2}, \tag{2.3}$$

where M is the wake moment and is dependent on the shape of the obstacle and the force exerted on it, and U_h is the velocity of the approach flow at the windbreak height H. This coefficient is a measurement of the wake strength and is dependent on the front-facing area (which is the area exposed to the normal streamwise direction), meaning both the aspect ratio and the deflection angle are important.

The local force exerted on the flat plate in the direction of α is then denoted as

$$F = \left(\frac{1}{2}\right) \rho_\infty C_D W H U_h^2 \cos^2(\alpha). \tag{2.4}$$

They also proposed a formulation for the near-wake deflection angle θ given as

$$\sin(\theta) = \frac{HW\cos^2(\alpha)\sin(\alpha)\, C_D}{2\left(H + H\sqrt{\frac{2x}{HRe}}\right)\left(W\cos(\alpha) + 2H\sqrt{\frac{2x}{HRe}}\right)}, \tag{2.5}$$

where x denotes a point in the downstream direction.

Chapter 3 - Experimental Approach

3.1 Introduction

The experiments on the flow around the surface-mounted flat plates were conducted in the Department of Mechanical Engineering's low-speed closed-return wind tunnel. The flow around the thin flat plate was not expected to be significantly Reynolds number dependent due to the fixed separation locations along its edges, and therefore all of the experiments were conducted at a single Reynolds number of Re = 3.8×10^4, based on a single freestream velocity of U_∞ = 20 m/s and a single plate width of W = 31.5 mm. This experimental approach was similar to that adopted by Unnikrishnan et al. [11] for the flow around surface-mounted finite-height square prisms, which were also conducted at a single value of Reynolds number. More information on the wind tunnel can be found in Chapter 3.2.

Thin flat plates with four different aspect ratios were tested, of AR = 0.5, 1, 2, and 3. The incidence angle of the plates was varied from α = 0° to 90° in increments of 5° (or larger, depending on the range of interest). The inclination angle was kept constant at β = 0°, meaning the flat plates were always mounted vertical and normal to the ground plane. More information on the flat plate models can be found in Chapter 3.3.

The mean wake of the flat plates was measured using a seven-hole pressure probe, similar to that used by Sumner et al. [12] and Unnikrishnan et al. [11]. Information on the wind tunnel instrumentation, the seven-hole probe, and the measurement grids and planes for the wake measurements, is given in Chapter 3.4. The measurement uncertainty of the experiments is summarized in Chapter 3.5.

The experiments were conducted using a single boundary layer thickness at the location of the flat plates. This resulted in a constant value of relative boundary layer thickness of $\delta/W \approx 1.14$. The use of a single boundary layer on the wind tunnel's ground plane is similar to the finite square prism experiments of Unnikrishnan et al. [11] that were conducted in the same laboratory. Detailed information on this boundary layer is presented in Chapter 3.6.

3.2 Wind Tunnel

Experiments were conducted in the low-speed wind tunnel in the Department of Mechanical Engineering at the University of Saskatchewan. It has a closed-return design as shown in Fig 3.1.

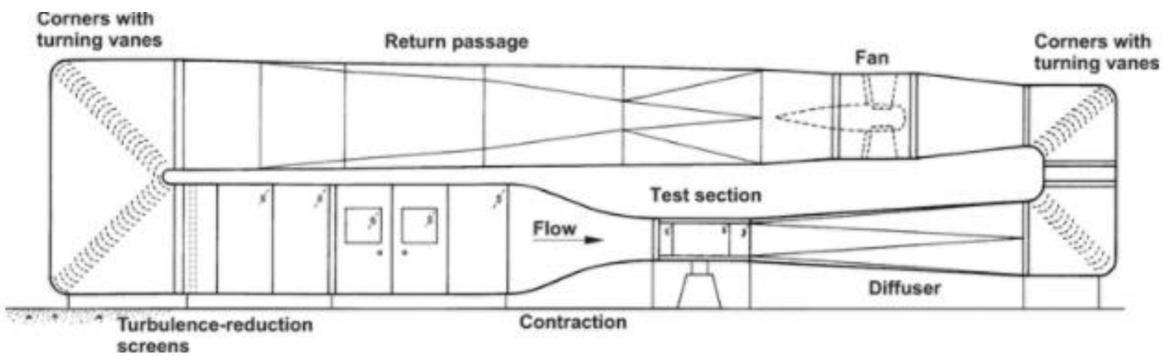

Figure 3.1. Diagram of the low-speed closed-return wind tunnel used for the experiments.

The airstream is supplied by a 100 hp electric motor with a constant-speed fan adapted with a swashplate that allows the blade pitch to be varied; this allows a freestream velocity range of U_∞ = 10 to 50 m/s. Starting from the flow generated by the fan, the air goes through two corners with turning vanes that minimize flow separation and secondary flows, afterwards the flow undergoes through a pair of reduction screens which give uniformity to the flow reducing the turbulence intensity. The airstream then goes through a settling chamber followed by a contraction that accelerates the flow going into the test section. The longitudinal freestream turbulence intensity of the wind tunnel is about 0.6%.

The wind tunnel's test section has the following dimensions: 0.91 m (height) ×1.13 m (width) × 1.96 m (length). The sidewalls are made of acrylic allowing the visualization of the experiments conducted. The test section also contains an aluminum ground plane which has a turntable used to mount test models as well as a traversing wing located inside the test section with a three-axis computer-controlled positioning system for measuring probes. The flat plates (Chapter 3.3) are mounted normal to the ground plane. The turbulent boundary layer on this ground plane, in which the plates are partially or fully immersed, is described in Chapter 3.6.

A computer with a National Instruments PCIe-6259 16-bit data acquisition board and LabVIEW software (used to develop various "virtual instruments") are used to acquire the wind tunnel data, rotate the test model in incidence angle α with the help of a stepper motor, control the swashplate that regulates the wind speed produced by the fan, as well as control three stepper motors that position the probe attached to a traversing wing.

The flat plate models were mounted at the centre of the turntable in the ground plane, and were located 900 mm downstream of the ground plane's leading edge. Figure 3.2 shows the test section of the wind tunnel with the setup of the instruments.

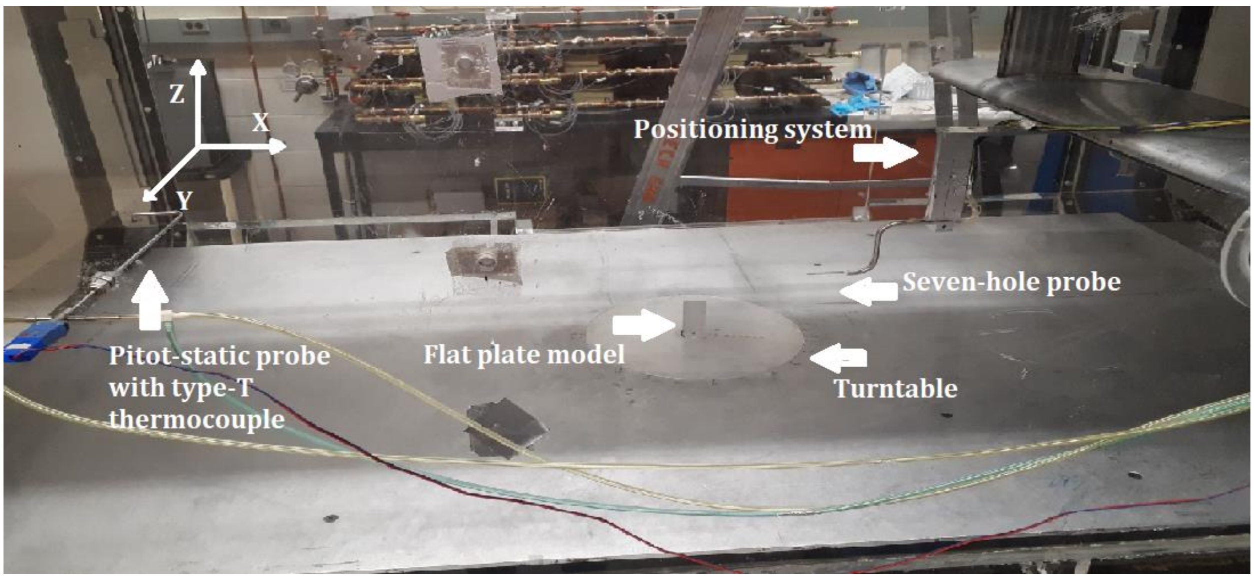

Figure 3.2. Setup of the experiments in the test section of the wind tunnel, showing (from left to right) the Pitot-static probe, the flat plate model, turntable, seven-hole probe and the probe's positioning (traversing) system.

3.3 Flat Plates

The design of the three-dimensional finite-height thin rectangular flat plate models used in the research needed to consider the plate's edge configuration, thickness, and material. Four main flat plate models (Fig. 3.3) with a thoroughly polished smooth surface were cut from cold-rolled steel in the Engineering Shops at the University of Saskatchewan. Using beveled edges like [18], [19] and [20] was avoided.

The same width of W = 31.5 mm was used for each of the four flat plates, but with heights of H = 15.75, 31.5, 63 and 94.5 mm corresponding to flat plates of AR = 0.5, 1, 2 and 3, respectively . This resulted in a small solid blockage ratio of 0.3% for the largest flat plate of AR = 3.

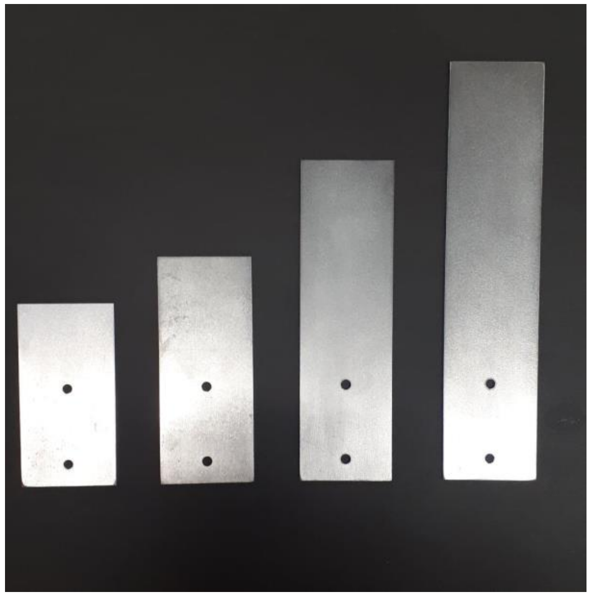

Figure 3.3. Flat plate models used in the experiments (from left to right) AR = 0.5, 1, 2, and 3. Only the upper portion of the plate is immersed in the flow; the lower part of the plate with the pair of mounting holes is located below the ground plane.

The thickness-to-width ratio was kept constant at t/W = 0.024 making it consistent with the literature on flat plates, which has reported values of t/W = 0.05, 0.025, 0.180, 0.0125 [1], t/W = 0.008 [2], t/W = 0.008 to 0.5 [5], t/W = 0.021 [9], and t/W = 0.06 [20] (See Table 2.1), while also being sturdy enough to endure the forces being applied to it without visibly bending or vibrating.

Thermal effects due to the heating of the wind tunnel caused some small upward movement of the ground plane which meant a small disparity (up to 0.7mm) between the height (z direction) of the turntable and the plate holder shown in Fig. 3.4. In order to minimize the flow disturbance caused by this effect, a small shim (Fig. 3.5) with a thickness of 0.5 mm was added between the T-bar of the wind tunnel's force balance (used to securely mount the plate holder only, not to measure the aerodynamic forces) and the mounting plate when the ground plane location increased more than 0.5 mm.

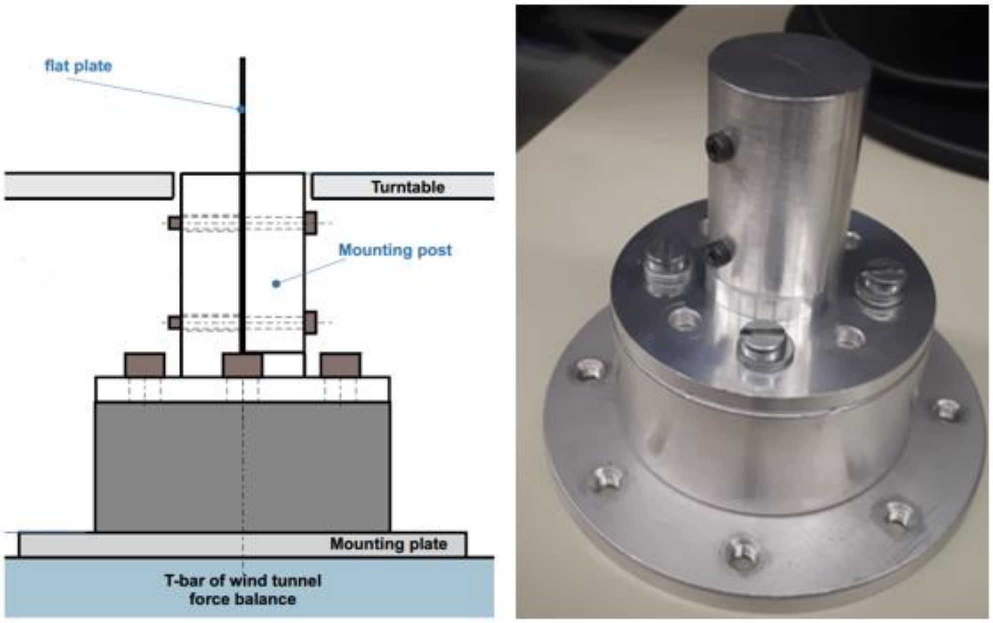

Figure 3.4. Sketch of the plate holder positioned on the force balance's rigid steel T-bar below the ground plane (left) along with a photograph of the plate holder (right, without the flat plate inserted into the holder).

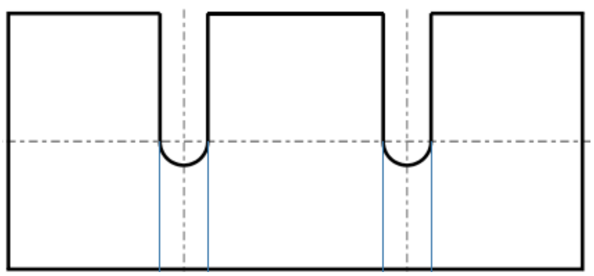

Figure 3.5. Sketch of the shim used to counter dilatation effects of the ground plane.

A small circumferential gap between the mounting post (as shown in Fig. 3.6) and the ground plane was present during the experiments which varied up to 1 mm when turning the flat plate to set different incidence angles (α). The variation of the gap was believed to be due to the ground plane's dilatation. A wake test with a thin aluminum tape cover over the gap demonstrated that no significant interference was being caused by this small opening.

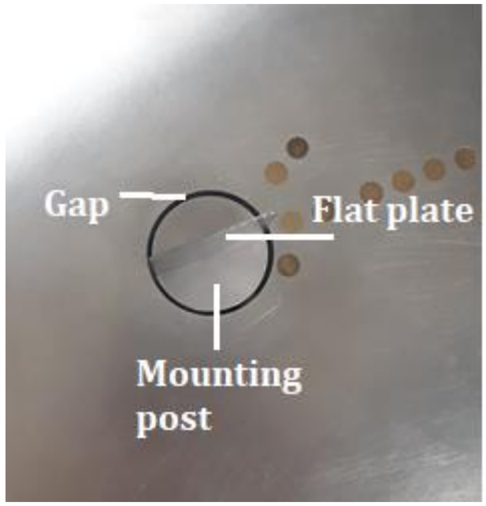

Figure 3.6. Upper view of a rotated flat plate model showing the circumferential gap between the mounting post and the ground plane.

3.4 Instrumentation

3.4.1 Freestream Velocity and Temperature Measurements

The freestream velocity U_∞ is used to calculate the Reynolds number and non-dimensionalize the velocity components (u, v, w) and other wake information like the vorticity components (ω_x, ω_y, ω_z). In these experiments, the freestream velocity was kept close to U_∞ = 20 m/s. The freestream temperature T_∞ was used to compute the air density (ρ_∞) and dynamic viscosity (μ_∞). Temperatures in the experiments did not generally exceed 40ºC.

In order to obtain the freestream measurements, a United Sensor Pitot-static probe (with a diameter of 3.175 mm) with an integrated type-T thermocouple (Fig. 3.7) was used to measure the freestream static pressure (P_∞), stagnation pressure (P_o), and freestream temperature (T_∞). The Pitot-static probe was mounted on the sidewall of the test section and aligned with the freestream at 400 mm from the start of the test section and 340 mm above the ground plane (Fig. 3.2). The static pressure line from the probe was connected to a Datametrics Barocel Type 600 absolute pressure transducer (Model 600A-1000T-513-H21X-4) to measure the absolute value of P_∞. Both pressure lines were connected to a Datametrics Barocel Type 590 differential pressure transducer (Model 590D-10W-2QBVIX-4D) to measure the freestream dynamic pressure (q_∞) as shown in Equation (3.1).

$$q_\infty = P_o - P_\infty \tag{3.1}$$

The density of the air (ρ_∞) was computed using the ideal gas equation as shown in Equation (3.2),

$$\rho_\infty = \frac{P_\infty}{RT_\infty}, \tag{3.2}$$

where R is the specific ideal gas constant for air (R = 287 J/(kg·K)). Knowing the air density, the freestream velocity can be calculated from Equation (3.3).

$$U_\infty = \sqrt{\frac{2q_\infty}{\rho_\infty}} \tag{3.3}$$

Figure 3.7. Pitot-static probe mounted on the sidewall of the wind tunnel with an integrated type-T thermocouple.

The dynamic viscosity of the air (μ_∞) was calculated using Sutherland's law [30],

$$\mu_\infty = \mu_o \left(\frac{T_\infty}{T_o}\right)^{\frac{3}{2}} \left(\frac{T_o + S}{T_\infty + S}\right), \tag{3.4}$$

where μ_o = 1.71x10^{-5} N·s/m^2, T_o = 273 K and S = 110.4 K.

A schematic of the Pitot-static probe arrangement with the pressure transducers is shown in Fig. 3.8.

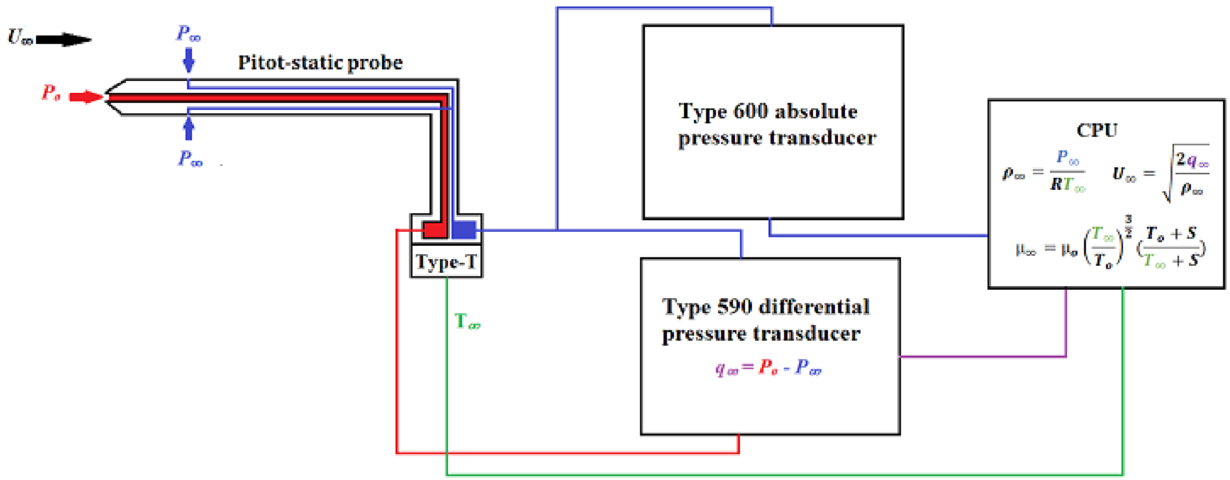

Figure 3.8. Diagram of the Pitot-static probe connected to the pressure transducers, where red and blue lines are tubes and the green line is thermocouple wire.

3.4.2 Mean Wake Measurements (Seven-Hole Probe)

The instrument used to measure the time-averaged wake velocity components is a seven-hole pressure probe (Fig. 3.9) that was manufactured by Engineering Shops at the University of Saskatchewan. It is composed of seven close-packed stainless steel tubes silver-soldered together with a 30° cone angle. The seven tubes are encased in an outer stainless steel tube giving an outer diameter of 3.45 mm. The probe diameter is about 10% of the width W of the flat plates being tested in the experiments. The probe uses the direct-interpolation calibration data reduction method of Zilliac et al. [32] with a calibration grid spacing of 8.1°. According to Sumner [33], the direct-interpolation approach has an improved accuracy for larger flow angles which may be useful when dealing with high flows angles that may occur in the wake region behind a bluff body. The flow angle range of the probe is ±72.9° with an uncertainty of less than 3° for the measured flow angle and 5% of the measured velocity magnitude [11].

The seven-hole probe is used together with a Scanivalve ZOC-17IP/8Px pressure scanner to obtain pressure information from the seven pressure holes on the probe. The pressure lines are connected to differential pressure transducers within the ZOC pressure scanner, each of which use P_∞ as the reference pressure. The ZOC pressure scanner is set to zero itself and calibrate itself automatically every 200 measurements. The calibration checks, which are enabled by the LabVIEW code, compare the ZOC pressure scanner outputs to that of a highly accurate BOC Edwards Model 590DF differential pressure transducer. Both the ZOC pressure scanner and the BOC Edwards transducer are exposed to same pressurized air source from the Engineering Building compressor. Any differences between the individual ZOC transducer outputs and that the of the BOC Edwards transducer result in corrections to the ZOC transducers' calibration curves in LabVIEW. A similar approach is used to check the zero outputs of the ZOC transducers.

The seven measured pressures are used to compute pressure coefficients that are used with the calibration data reduction method to find the yaw angle, pitch angle, local static pressure, and local dynamic pressure of the flow. This information is then used to compute the local velocity components (u, v, w). The seven-hole probe measurements use a sampling frequency of 1 kHz for a period of 10 s, resulting in time-averaged measurements of the local velocity vector and pressure at each measurement location in the wake.

Most wake measurements for the flat plates were performed in vertical transverse (y-z) planes. These planes were located at streamwise locations of $x/W = 2$, $x/W = 4$, and $x/W = 6$ downstream of the flat plate. The grid resolution of these measurements was of $\Delta y = \Delta z = 5$ mm consistent with previous seven-hole probe experiments by Sumner et al. [12] and Unnikrishnan et al. [11]. The grid spacing of 5 mm was selected as a compromise between the spatial resolution and the time duration of the experiments.

Other measurements were performed on a vertical plane parallel to the mean flow (x-z plane) at $y = 0$, with grid resolutions of $\Delta x = 10$ mm and $\Delta z = 5$ mm. These measurement planes were only used when the flat plate was at an incidence angle of $\alpha = 0°$ to measure the size of the recirculation zone. The increased grid spacing in the x direction for the x-z plane was conveyed in order to comply with the scheduled duration of the experiments and due to the reduced variation of the velocity components in the streamwise direction.

The size of each measurement plane was determined experimentally, however the criteria to determine the length and width of each plane was to show the entire extent of the vortex structures. It should be pointed out the shape and size of the recirculation zone was expected to change with the incidence angle α, hence the importance of testing at different x/W distances. The combinations of incidence angles tested at these distances varied depending of the importance of the flow structures (see Appendix A).

Figure 3.9. Seven-hole probe

3.5 Uncertainty Analysis

Every instrument used in the experiments as well as the testing environment carries some uncertainty associated with it. It is important to estimate how significant these accumulative uncertainties are and how do they affect the measurements in order to gauge their accuracy and repeatability. An uncertainty analysis with some level of confidence (95% was deemed appropriate for this research) is necessary for this purpose.

For all of the measurements, the type-A uncertainty (based on the repeatability of many measurements) is small and can be neglected compared to the type-B uncertainty (based on the calibration curves and information from the manufacturers of the instruments, etc.). Sensitivity coefficients are used to propagate the uncertainties of the individual measured quantities into the uncertainty of the result.

For the freestream velocity measurements starting with the Pitot-static probe, there are some uncertainties associated with the pressure transducers, alignment of the probe with the freestream (pitch and yaw misalignments), and Reynolds number effects due to the geometry and size of the probe as well as viscous effects at low probe Reynolds numbers [34]. Another source of uncertainty for the freestream measurements is the longitudinal freestream turbulence intensity.

For the Type 600 pressure transducer used to measure the static pressure (P_∞) an accuracy of ±0.05% and a repeatability of ±0.01% for a full scale of 1000 Torr are considered [35]. For the Type 590 pressure transducer used to measure the dynamic pressure (q_∞) a value of ±0.05% for accuracy and a value of ±0.01% for repeatability were considered [36]. This measurement is also affected by the longitudinal freestream turbulence of the wind tunnel which was measured to be 0.6% at U_∞ = 20 m/s [13]. The Reynolds number effects are only significant at Re < 300 [37], however from the probe Reynolds number calculations considering the probe's internal radius an error of less than 0.5% in the measured dynamic pressure was estimated.

The integrated type-T thermocouple for the freestream temperature measurements (T_∞) later used in the calculation of ρ_∞ and μ_∞ has an estimated error of ±0.5ºC.

Wall solid blockage due to the flat plate models was of 0.3% for the largest prism (AR = 3) which is considered insignificant for the current experiments.

For the seven-hole probe wake measurements the Scanivalve ZOC17 pressure scanner reported an accuracy of 0.2% of the measured pressures [38].

The probe positioning system also carries some error that was estimated to be ±0.5 mm. This assessment is based on a visual inspection of the probe when moving it across the test section during repeated experiments.

The incidence angle is estimated to have an error of ±0.25º based on visual inspection of the experiments and assuming that it corresponds to an error of one step in the servomotors used to move the turntable. The same goes for the alignment of the probe with the flow and plate.

A calculation of the propagated uncertainties with the sensitivity coefficients using the root-sum square approach [39] assuming conservative measured values of the freestream conditions is summarized in Table 3.1.

Table 3.1. Summary of uncertainties for experimental freestream values

Variable	Conservative value	Standard uncertainty	95% confidence level	Error %
P_o	95.215 kPa			
P_∞	95 kPa	0.02796 kPa	0.05592 kPa	0.05%
q_∞	215 Pa	0.62387 Pa	1.24774 Pa	0.5%
T_∞	25 ºC (273 K)	0.2886 ºC	0.5772 ºC	0.2%
μ_∞	$1.8372(10)^{-5}$ kg/(m·s)	$1.369(10)^{-8}$ kg/(m·s)	$2.738(10)^{-8}$ kg/(m·s)	0.1%
ρ_∞	1.1098 kg/m^3	$1.123(10)^{-3}$ kg/m^3	$2.246(10)^{-3}$ kg/m^3	0.2%
U_∞	19.68 m/s	0.030245 m/s	0.06049 m/s	0.3%

The uncertainty in the freestream velocity is approximately 0.30% of the full measurement with a 95% confidence level, which seems to be an acceptable uncertainty for the experiments.

Regarding the seven-hole probe, uncertainty for those measurements are a variation of 3° for the flow angle and 5% of the measured velocity angle [11] [13]. Comparing them to the other measurements involved, they prove to be the major source of uncertainty in the experiments.

3.6 Boundary Layer

The boundary layer thickness δ on the ground plane is a key influencing parameter for the flow around surface-mounted finite-height bluff bodies including 3D flat plates [10]. Only one configuration of boundary layer (thin) was used in the present experiments. This means that no boundary layer trip was installed and the boundary layer formed naturally from the leading edge of the ground plane. The leading edge of the ground plane where the boundary layer originates was 900 mm upstream of the flat plate models. A fully developed turbulent boundary layer was formed over the ground plane with a thickness δ, defined as the point at where the local streamwise velocity $u(z)$ reaches $0.99U_\infty$.

Measurements of the boundary layer were made with a modified United Sensor boundary layer Pitot-probe of 0.85 mm external diameter. The reduced diameter increases the probe's ability to perform measurements closer to the ground plane reducing the interference caused by the probe. The mean streamwise velocity profile $u(z)$ is calculated with the stagnation pressure P_o measured from the boundary layer probe and the static pressure P_∞ measured with the Pitot-static probe. The pressure was measured with a Validyne P55D differential pressure transducer.

Measurements were performed at streamwise locations of $x/W = -6$, -4, and -2 upstream of the flat plate model, at $x/W = 0$ (at the location of the flat plate model), and at $x/W = 2$, 4 and 6 (downstream of the flat plate model). The velocity profiles from the Pitot tube were compared with the 1/7$^{\text{th}}$ power law, and this curve along with selected measurements are shown in Fig. 3.10. Results are summarized in Table 3.2 along with calculations of the displacement thickness (δ^*), momentum thickness (θ), and shape factor (δ^*/θ) obtained from equations (3.5) and (3.6), respectively.

$$\delta^* = \int_0^\delta (1 - \frac{u}{U_\infty}) dz \tag{3.5}$$

$$\theta = \int_0^\delta (\frac{u}{U_\infty})(1 - \frac{u}{U_\infty}) dz \tag{3.6}$$

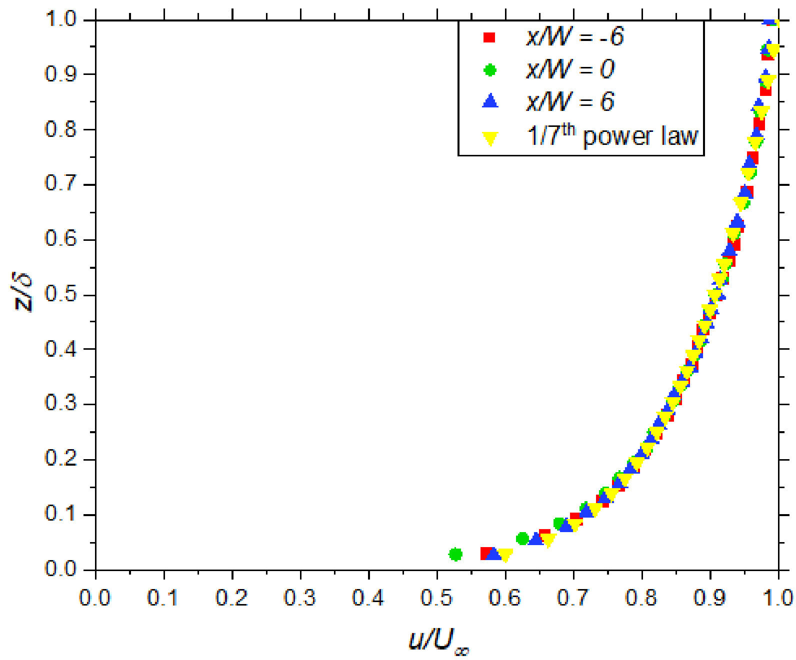

Figure 3.10. Boundary layer mean streamwise velocity profile for a freestream velocity of U_∞ = 20 m/s at $x/W = -6$, $x/W = 0$, $x/W = 6$ and the 1/7th power law at $x/W = 0$.

Table 3.2. Summary of boundary layer characteristics for the 3D flat plate experiments at U_∞ = 20 m/s.

	$x/W = -6$	**$x/W = -4$**	**$x/W = -2$**	**$x/W = 0$**	**$x/W = 2$**	**$x/W = 4$**	**$x/W = 6$**
δ/W	1.02	1.02	1.08	1.14	1.14	1.21	1.27
δ/H (AR = 0.5)	2.04	2.04	2.16	2.28	2.28	2.42	2.54
δ/H (AR = 1)	1.02	1.02	1.08	1.14	1.14	1.21	1.27
δ/H (AR = 2)	0.51	0.51	0.54	0.57	0.57	0.61	0.64
δ/H (AR = 3)	0.34	0.34	0.36	0.38	0.38	0.4	0.42
δ (mm)	32	32	34	36	36	38	40
δ^* (mm)	3.9	4	4.2	4.5	4.5	4.6	4.6
θ (mm)	3.1	3.2	3.3	3.5	3.5	3.6	3.7
δ^*/θ	1.26	1.27	1.27	1.28	1.27	1.27	1.26

Chapter 4 - Results and Discussion

4.1 Introduction

This chapter reviews the effects of aspect ratio (*AR*) and incidence angle (α) on the mean wake of a surface-mounted 3D rectangular flat plates. The results for flat plates oriented normal to the flow (at α = 0º) are presented in Section 4.2. The results for the flow around flat plates oriented at non-zero incidence angles are presented in Section 4.3.

For the case of α = 0º (Section 4.2), measurements were carried out in the vertical (*x*-*z*) symmetry plane (at *y* = 0) and in a vertical cross-stream (*y*-*z*) plane downstream of the flat plate. The measurements in the vertical symmetry plane were used to determine the shape and length of the recirculation zone as well as to examine the strong separated shear layer originating from the top of plate. The boundary of the recirculation zone is defined by the edge of the region where there are no velocity vectors computed from the seven-hole probe measurements. A better and more accurate definition is the shape of the dividing streamline along the boundary of the recirculation zone, which cannot be obtained from the seven-hole probe data. The grid spacing was Δx = 10 mm and Δz = 5 mm, similar to Unnikrishnan et al. [11]. Vertical cross-stream (*y*-*z*) plane measurements were implemented at a streamwise position of x/W = 6, ensuring the measurements would be outside the recirculation zone behind the plate. The measurements in the *y*-*z* plane were used to identify the wake flow patterns and the streamwise vortex structures. The grid spacing was Δy = 5 mm and Δz = 5 mm for this plane, similar to Unnikrishnan et al. [11].

The effects of incidence angle α on the wakes of surface-mounted 3D rectangular flat plates are examined next (Section 4.3). In these experiments, the flat plates were oriented at angles from α = 0º to 90º (typically in increments of 5º depending on the *AR*), and vertical cross-stream (*y*-*z*) plane measurements were made at a position of x/W = 6. The grid spacing was Δy = 5 mm and Δz = 5 mm for these planes.

In both Sections 4.2 and 4.3, the wakes of the 3D rectangular flat plates are compared with those of surface-mounted finite-height cylinders [13] and of surface-mounted finite-height square prisms [11] [12] [15], all from similar wind tunnel experiments conducted at the University of

Saskatchewan. This comparison is made in order to identify possible similarities in the wakes of plates, cylinders, and prisms, as well as any afterbody effects for surface-mounted bluff bodies.

The results depicted in the present research were carried out at a Reynolds number of Re = 3.8×10^4 and a relative boundary layer thickness of $\delta/W \approx 1.14$. The earlier finite cylinder experiments from Sumner et al. [13] were performed at Re = 6×10^4 with a higher boundary layer thickness ratio (using the cylinder diameter as reference) of $\delta/W \approx 2.6$. The finite square prism data from [11] [12] were acquired at a similar Reynolds number to the present thesis research, with Re = 3.7×10^4, but with a slightly thicker boundary layer of $\delta/W \approx 1.5$. Results from [15] for finite square prisms were obtained at Re = 7.5×10^4 and $\delta/W \approx 0.7$.

4.2 Flat Plates Normal to the Flow

This section presents the experimental results for the 3D rectangular flat plates oriented normal to the flow ($\alpha = 0^{\circ}$). Measurements of the velocity components in the *x*-*z* and *y*-*z* planes are analyzed, reviewed and compared with previous work involving finite square prisms and finite cylinders.

4.2.1 Vertical Symmetry (*x*-*z*) Plane

The time-averaged velocity vector fields in the vertical (*x*-*z*) symmetry plane (at $y = 0$) show the in-plane velocity components u (streamwise) and w (vertical), which are normalized by the freestream velocity as u/U_∞ and w/U_∞. Figure 4.1 shows results for the flat plates of AR = 0.5, 1, 2 and 3 from the present experiments. Behind the flat plate is a recirculation zone characterized by high-angled or recirculating flow, which can be seen as the region with an absence of velocity vectors in Fig. 4.1 [40]. This absence of velocity vectors is attributed to the angular range of the seven-hole probe, which can only measure angles up to ±72.9º. It can be seen from Fig. 4.1 that the recirculation zone extends farther in the streamwise direction closer to the ground plane.

For the flat plate, the shape of the recirculation zone boundary is dissimilar for AR = 3 (Fig. 4.1a) compared to lower aspect ratios of AR = 1 (Fig. 4.1c) and AR = 0.5 (Fig. 4.1d), starting with an arch pattern (initially upward-directed flow from the top edge of the plate, followed by a strong downward-directed flow making the shape of an arch), which is followed by a concave portion right above mid-height, and then an abrupt vertical "collapse" of the boundary towards the ground plane near $x/W = 6$. In contrast, the shape of the recirculation zone boundary for the lower aspect ratios (AR = 1 and 0.5) follows an arch pattern that ends on the ground plane; the location on the ground plane where the boundary ends depends on the AR.

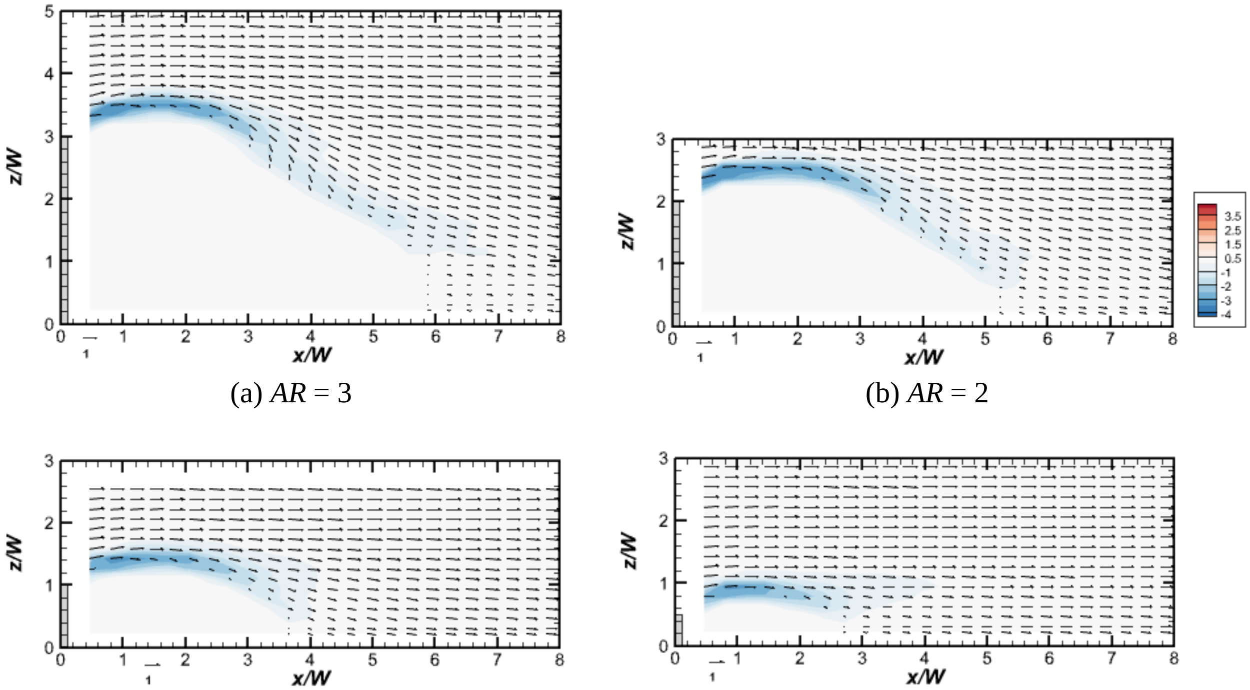

(a) AR = 3

(b) AR = 2

(c) AR = 1

(d) AR = 0.5

Figure 4.1. Mean velocity vector field (showing in-plane velocity vector components u/U_∞, w/U_∞) in the vertical symmetry plane along the wake centerline (y = 0) for 3D rectangular flat plates at α = 0º: (a) AR = 3, (b) AR = 3, (c) AR = 1, and (d) AR = 0.5. Also shown are the in-plane mean transverse vorticity ($\omega_y W/U_\infty$) contours, which show the presence of the separated shear layer originating from the upper edge of the plate. The region where the velocity vectors are absent is where the local flow angle exceeds the angular range of the seven-hole probe or the flow is reversing.

For all four flat plates in Fig. 4.1, the clockwise transverse (y) vorticity shows the separated shear layer that originates from the upper edge of the plate. The shear layer is seen to follow the upper part of the boundary of the recirculation zone. The flat plate of AR = 3 (Fig. 4.1a) has a shear layer that goes along the dividing streamline or boundary separating the recirculation zone from the rest of the wake. The vorticity representing the shear layer loses strength the further it goes from the initial detachment. This shear layer comes to an end before reaching the ground plane at the point where the abrupt vertical "collapse" of the recirculation zone boundary starts, not before extending slightly in the x direction. A similar effect is produced for flat plates with aspect ratios AR = 2, 1 and 0.5 where this feature is more noticeable when decreasing the AR.

The flat plate of *AR* = 2 (Fig. 4.1b) seems to share transitional characteristics from both *AR* = 3 (Fig. 4.1a) and *AR* = 1 (Fig. 4.3c), while not showing an arch shaped recirculation zone boundary like in *AR* = 1 (Fig. 4.1c) and *AR* = 0.5 (Fig. 4.1d), nor a concave zone in the middle as with *AR* = 3 (Fig. 41a). Instead it seems to denote a straight diagonal mid-height shape with a small abrupt vertical "collapse" near the ground plane, possibly denoting *AR* = 2 as a transitional aspect ratio.

Figure 4.2 shows results for a finite cylinder of *AR* = 3 from [13] and finite square prisms of *AR* = 3, 1, 0.7, and 0.5 from [11] [12] [15]. For the case of the cylinder of *AR* = 3 (Fig. 4.2a), the wake shows downwash that reaches the ground plane in a similar fashion as the flat plate with an abrupt vertical "collapse" of the recirculation zone boundary towards the ground plane. The length of the recirculation zone for the cylinder is much smaller than that of the flat plate of *AR* = 3 (Fig. 4.1a) and the finite square prism of *AR* = 3 (Fig. 4.2b); this could be due to the nature of the cylinder's cross-sectional shape which interferes less with the flow than objects with a normal flat front face and sharp edges.

The square prism of *AR* = 3 (Fig. 4.2b) has an arched recirculation zone boundary followed by a concave section predominated by strong downwash similar to the flat plate, with a gradual reattachment to the ground plane instead of the sudden vertical "collapse" of the recirculation zone boundary for the flat plate with the same *AR* (Fig. 4.1a). For the square prisms with lower aspect ratios (*AR* = 1, 0.7 and 0.5) (Figs. 4.2c-e), the shape of the recirculation zone boundary follows an arch pattern that gradually reattaches to the ground downstream similar to the behaviour of the flat plates in the same range of aspect ratio. Unfortunately, there are no studies available of the flow around a square prism of *AR* = 2, which could establish if the transitional behavior seen for the flat plate (Fig. 4.2b) is also found for square prisms.

The shear layer for the finite cylinder (Fig. 4.2a) is weaker than those of the flat plates and the square prisms; this can be attributed to the different leading edge shape for the cylinder free end and reattachment of the flow onto the free end [41]. The shear layers from the leading edges of the finite square prisms of *AR* = 1, 0.7 and 0.5 (Figs. 4.2c-e) are stronger than those of the flat plates of AR = 1 and 0.5 (Figs. 4.1c-d); this may be an effect of the upper surface of the prism (and hence the afterbody), which is not present for the flat plates.

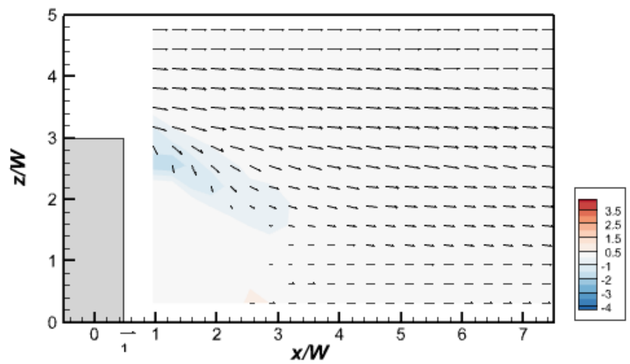

(a) Finite cylinder, AR = 3

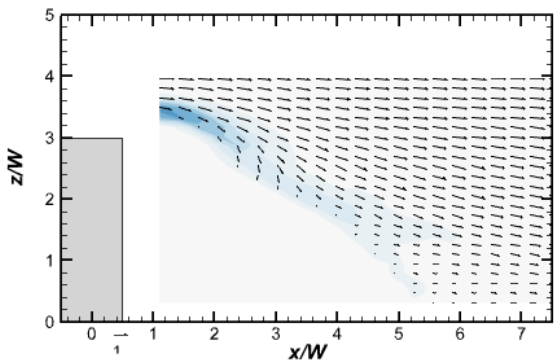

(b) Finite square prism, AR = 3

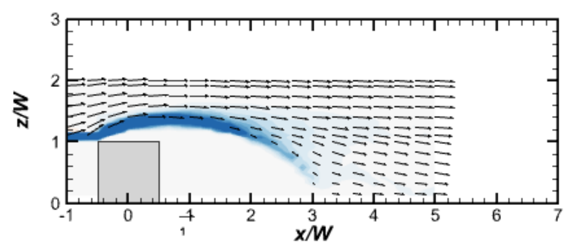

(c) Finite square prism, AR = 1

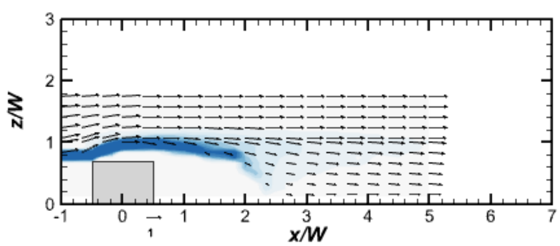

(d) Finite square prism, AR = 0.7

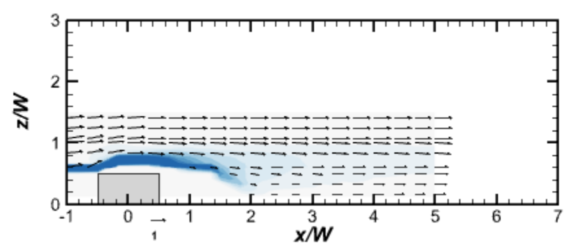

(e) Finite square prism, AR = 0.5

Figure 4.2. Mean velocity vector field (showing in-plane velocity vector components u/U_∞, w/U_∞) in the vertical symmetry plane along the wake centerline (y = 0): (a) finite cylinder, AR = 3, Re = 6×10^4, δ/W = 2.6, from [13]; (b) finite square prism at α = 0º AR = 3, Re = 3.7×10^4, δ/W = 1.5, from [11]; (c) finite square prism at α = 0º, AR = 1, Re = 7.5×10^4, δ/W = 0.7, from [15]; (d) finite square prism at α = 0º, AR = 0.7, Re = 7.5×10^4, δ/W = 0.7, from [15]; (e) finite square prism at α = 0º, AR = 0.5, Re = 7.5×10^4, δ/W = 0.7, from [15]. Also shown are the in-plane mean transverse vorticity ($\omega_y W/U_\infty$) contours, which show the presence of the separated shear layer. The region where the velocity vectors are absent is where the local flow angle exceeds the angular range of the seven-hole probe or the flow is reversing.

For the square prisms, the vorticity representing the shear layer becomes more noticeable farther downstream from the body as the aspect ratio is lowered from AR = 1 (Fig. 4.2c) to AR = 0.5 (Fig. 4.2e). A stronger shear layer strength for the finite prisms (compared to the flat plates) could explain why this effect is more noticeable.

The length of the recirculation region L_r in the streamwise direction x can be defined as the distance from the center of the bluff body to the point of reattachment of the recirculation zone boundary onto the ground plane. This is equivalent to the location of the first velocity vector from the rear of the bluff body, along the lowest row of vectors closest to the ground plane.

The maximum streamwise length of the recirculation zone is shown to be dependent on the aspect ratio, as shown in Fig. 4.3. The tendency shows a growth of L_r/W when the aspect ratio increases. For a flat plate of AR = 0.5, the mean recirculation zone extends downstream to a maximum of L_r/W = 2.7. Meanwhile for AR = 1, 2 and 3 the recirculation zone length reaches its limit downstream at L_r/W = 3.7, L_r/W = 5.2 and L_r/W = 5.9, respectively. A study by Okamoto [29] for a 3D flat plate of AR = 1 reported a value of L_r/W = 4.3, which is a little bit longer than that reported in the present work (L_r/W = 3.7). The differences in these values may be attributed to the boundary layer thicknesses ($\delta/W \approx 1.14$ for current work and $\delta/W \approx 4.8$ for Okamoto) and the method used to estimate L_r/W. The present research used the smaller (3.45 mm) seven-hole probe while Okamoto [29] used a larger (6 mm) and more rudimentary cylindrical yawmeter. Another thing to take in consideration is the definition used by Okamoto [29] for the recirculation zone length, which was the distance from the initial separation of the streamline of the leading edge to the point of reattachment downstream.

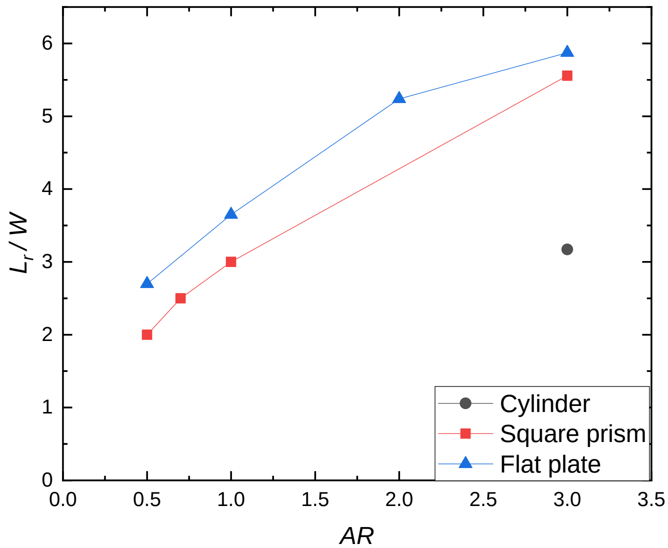

Figure 4.3. Maximum streamwise length of the recirculation zone (L_r/W) for a finite cylinder, finite square prism, and a 3D rectangular flat plate of different aspect ratios (AR).

The behaviour of L_r/W with AR is consistent with the information presented by Unnikrishnan et al. [11] and [15] for finite square prisms. This behaviour is also shown for finite cylinders by Sumner et al. [13]. From Fig. 4.3 it can be pointed out that when the AR is the same, L_r/W is the largest for the flat plate, followed by the finite square prism (which is consistent with the research performed by Okamoto [29]), and finally the finite cylinder, which has a noticeably smaller recirculation zone.

One thing to point out is how similar the streamwise distances are, between the initial separation of the flow from the top edge of the plate, to the reattachment onto the ground plane downstream, for the cases of the flat plate and the square prism (Fig. 4.4). By making this change in how L_r is defined, Fig. 4.4 now shows there is some collapse of the data initially presented in Fig. 4.3. This could imply the effects of the afterbody on the length of the recirculation zone are not as significant as previously thought, and possibly more dependent on a combination between shape of the leading edges and the front face overall.

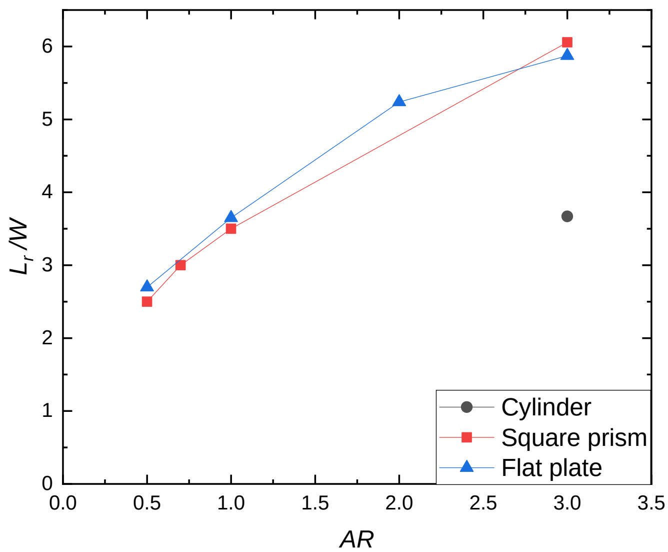

Figure 4.4. Adjusted streamwise length of the recirculation zone considering the initial separation of the flow from the top edge of the plate, to the point of reattachment onto the ground plane.

4.2.2 Vertical Cross-Stream (*y*-*z*) Plane

The time-averaged velocity vector fields in the vertical plane (*y*-*z*) normal to the flow show the in-plane velocity components *v* (horizontal) and *w* (vertical), which are normalized by the freestream velocity as v/U_∞ and w/U_∞. Figure 4.5 shows results for the wake behind 3D finite rectangular flat plates of AR = 3, 2, 1, and 0.5 from the present experiments at α = 0º. Also shown in Fig. 4.5 are contours of the normalized streamwise velocity u/U_∞. Every plane in Fig. 4.5 is located at the same streamwise location of x/W = 6. One thing to note is the small amount of asymmetry in the data at α = 0º due to small misalignments in the plate and probe, which were discussed in Section 3.5.

The boundary of the wake at x/W = 6 can be approximated by the u/U_∞ = 0.9 or 0.95 contour lines. The wake boundary of the 3D flat plate at x/W = 6 is characterised by one peak for all four aspect ratios (Fig 4.5). The wake boundary broadens as flat plate's AR is lowered. Farther from the flat plate and the centreline in the *y* direction, however, the streamwise velocity contour lines become horizontal and instead show the boundary layer on the ground plane rather than the wake of the flat plate.

Each flat plate produces a strong downwash (downward-directed velocity vectors) on the wake centerline. This downwash reaches the ground plane for the flat plates of AR = 2, 1, and 0.5 (Fig.

4.5a-c) but not for AR = 3 (Fig. 4.5a). The location of maximum downwash velocity above the ground plane at x/W = 6 occurs at z/H = 0.68, 0.63, and 0.79 for AR = 3, 2, and 1, respectively (see Table 4.1). The case of the flat plate of AR = 0.5 (Fig 4.5d) is notably different regarding the location of the peak value of downwash, which at x/W = 6 is located above the flat plate at z/H = 1.58 (see Table 4.1). This significant shift in location can be attributed to this plate's closeness to the ground plane. The magnitude of the maximum downwash velocity seems to decrease with the aspect ratio in a quasi-linear behaviour (see Table 4.1).

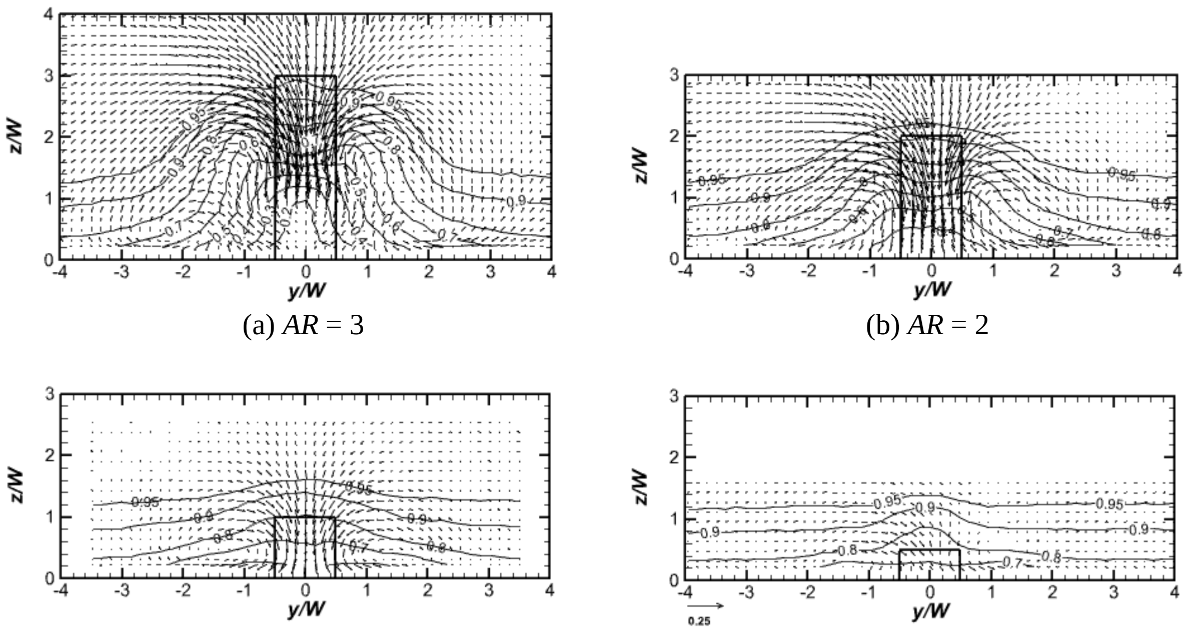

(a) AR = 3 (b) AR = 2

(c) AR = 1 (d) AR = 0.5

Figure 4.5. Mean velocity vector field (showing velocity vector components v/U_∞, w/U_∞) with streamwise mean velocity contours (u/U_∞) in the vertical cross-stream (y-z) plane for 3D rectangular flat plates at α = 0º: (a) AR = 3, (b) AR = 2, (c) AR = 1, and (d) AR = 0.5, from the present experiments, Re = 3.8×10^4, x/W = 6, δ/W = 1.14.

At x/W = 6, the minimum streamwise velocity $(u/U_\infty)_{min}$ becomes smaller when the aspect ratio of the flat plate is increased (Fig. 4.19). A greater velocity deficit occurs for the taller plates. These minimum velocities are $(u/U_\infty)_{min}$ = 0.19, 0.33, 0.58, and 0.65, for the flat plates of AR = 3, 2, 1, and 0.5, respectively.

Figure 4.6 shows results for the wake velocity field behind 3D finite square prisms of *AR* = 3, 1 and 0.5 at α = 0º from [11] [12] [15] and a finite cylinder of *AR* = 3 from [13]. Included in this figure are contour lines for the u/U_∞ streamwise velocity field, similar to Fig. 4.5.

Table 4.1. Critical values in the wake of the 3D flat plate (at α = 0º) in the *y-z* plane at x/W = 6.

	***AR* = 0.5**	***AR* = 1**	***AR* = 2**	***AR* = 3**
Vertical location of maximum vorticity (z/H)	0.44	0.22	0.63	0.63
Horizontal location of maximum vorticity ($\pm y/W$)	1.03	0.71	0.63	0.79
Maximum vorticity ± ($\omega_x W/U_\infty$)	0.30	0.42	0.43	0.53
Location of maximum downwash at centerline (z/H)	1.58	0.79	0.63	0.68
Maximum downwash ($-w/U_\infty$)	0.03	0.11	0.22	0.26

Regarding the wall normal mean velocity w/U_∞ in the *y-z* planes, the finite square prisms with AR = 3 and 1 (Fig. 4.6b-d) denote a strong downwash on the wake centerline which is a shared characteristic with flat plates (Fig. 4.5). Results show strong similarity for the maximum downwash between bluff bodies with *AR* = 0.5 and *AR* = 1 (Table 4.1 and 4.2). The result shown for the finite square prism of *AR* = 3 (Fig. 4.6b) is not necessarily comparable due to the different streamwise location for the measurements (x/W = 8 instead of x/W = 6). The vertical locations of the maximum downwash relative to their height seem to be slightly more elevated for the flat plate than the finite square prism, which is especially the case for *AR* = 0.5 as previously depicted. One thing to point out is the location of the maximum downwash for the finite square prism of *AR* = 0.5, which is concentrated in two points near the side edges and ground plane, instead of being situated on the wake centerline (y/W = 0) like the rest of the studied bluff bodies.

Regarding the wake boundary, the finite square prism of *AR* = 3 (Fig. 4.6.b) denotes two peaks, same as the finite cylinder of *AR* = 3 (Fig 4.6a), unlike the flat plate with only one peak (Fig. 4.5a). The dual peak shape for the wake boundary for the prism and cylinder may relate to the different afterbody shape. In contrast, the wake boundary for the flat plate and finite square prism of *AR* ≤ 1 are almost identical, with only a single peak. The minimum streamwise velocity for the finite square prisms shows a similar tendency to the flat plates where (taken from [12]) $(u/U_\infty)_{min}$ = 0.62 for *AR* = 1 and $(u/U_\infty)_{min}$ = 0.66 for *AR* = 0.5.

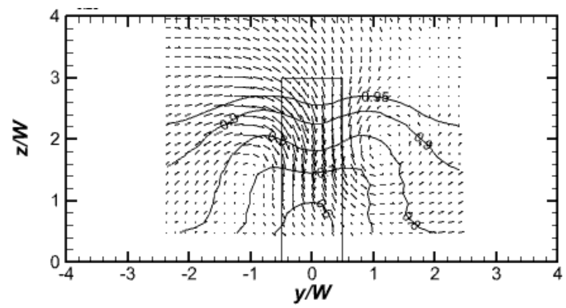

(a) Finite cylinder, AR = 3, x/W = 6

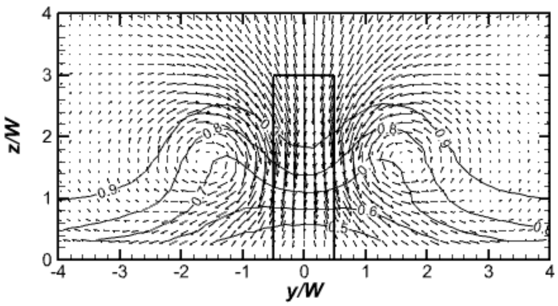

(b) Finite square prism, AR = 3, x/W = 8

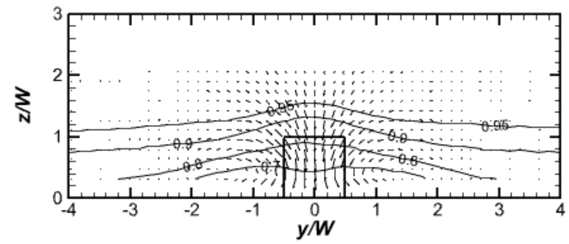

(c) Finite square prism, AR = 1, x/W = 6

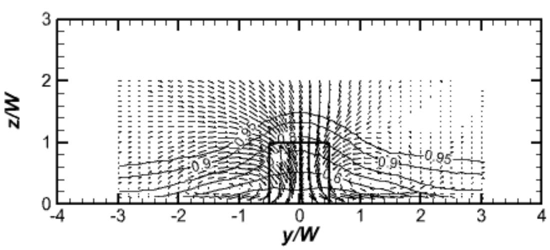

(d) Finite square prism, AR = 1, x/W = 4

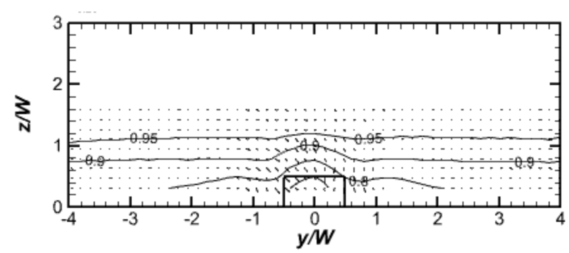

(e) Finite square prism, AR = 0.5, x/W = 6

Figure 4.6. Mean velocity vector field (showing velocity vector components v/U_∞, w/U_∞) with streamwise mean velocity contours (u/U_∞) in the vertical cross-stream (y-z) plane: (a) finite cylinder, AR = 3, Re = 6×10^4, δ/W = 2.6, from [13]; (b) finite square prism at α = 0º, AR = 3, Re = 3.7×10^4, δ/W = 1.5, from [11]; (c) finite square prism at α = 0º, AR = 1, Re = 3.7×10^4, δ/W = 1.5, from [12]; (d) finite square prism at α = 0º, AR = 1, Re = 7.5×10^4, δ/W = 0.7, from [15]; (e) finite square prism at α = 0º, AR = 1, Re = 3.7×10^4, δ/W = 1.5, from [12].

The normalized streamwise vorticity ($\omega_x W/U_\infty$) contours in the y-z planes are shown in Fig. 4.7. Concentrations of vorticity can help identify vortex structures in the wake. The rotation within the velocity fields seen in Fig. 4.5 now shows itself as large concentrations of vorticity on either side of the wake centreline in Fig. 4.7. The left side of the plane (-y) shows concentrations of clockwise (CW) vorticity while the right side (+y) shows concentrations of counter-clockwise (CCW) vorticity. Two sets of symmetrical streamwise vortices can be identified for the 3D flat plates of AR = 3 (Fig. 4.7a) and AR = 2 (Fig. 4.7b). One set is shown by the closed contour lines in the upper part of the wake. The other set is found closer to the ground plane farther from the wake centreline. For the flat plates of *AR* = 1 (Fig. 4.7c) and *AR* = 0.5 (Fig. 4.7d) only one pair of streamwise vortices is found in the upper part of the wake. The pair of counter-rotating vorticity concentrations in the upper part of the wake seems to be the main cause of the downwash located at the centerline ($y/W = 0$) and shown in Fig. 4.5, similar to what is seen for finite cylinders and finite square prisms [11] [12].

Table 4.2. Critical values in the wake of a finite square prism (at $\alpha = 0°$) in the *y-z* plane at $x/W = 6$.

	***AR* = 0.5**	***AR* = 1**	***AR* = 3***
Vertical location of maximum vorticity (z/H)	0.63	0.31	0.58
Horizontal location of maximum vorticity ($\pm y/W$)	1.03	0.71	1.26
Maximum vorticity ± ($\omega_x W/U_\infty$)	0.12	0.30	0.35
Location of maximum downwash at centerline (z/H)	0.63**	0.63	0.58
Maximum downwash ($-w/U_\infty$)	0.03	0.09	0.19

* Square prism of *AR* = 3 had *y-z* plane measurements performed at $x/W = 8$
** The maximum downwash for the finite square prism of *AR* = 0.5 was not located on the wake centerline; instead it was located at two separate points near the ground plane ($\pm y/W = 0.63$)

For the cases of *AR* = 3 (Fig. 4.7a) and *AR* = 2 (Fig. 4.7b) the upper pair of streamwise vortices represents the familiar tip vortex structures (seen in the wakes of surface-mounted finite-height cylinders and square prisms), while the lower set will be named as “ground plane vortex structures”. The latter structures have the same rotational direction as the arms of the horseshoe vortex, but by $x/W = 6$ these would no longer be present.

Table 4.1 shows the maximum strength and location of the vorticity for every plate; for the case of *AR* = 3 (Fig. 4.7a) and *AR* = 2 (Fig. 4.7b) this corresponds to the location of the tip vortices, while for the lower aspect ratios (*AR* = 1 (Fig. 4.7c) and *AR* = 0.5 (Fig. 4.7d)) the tip vortices seem to merge with the ground plane vortex structures. From Table 4.1 the relative vertical location (z/W) of the tip vortices is the same for *AR* = 3 (Fig. 4.7a) and *AR* = 2 (Fig. 4.7b).

For the case of *AR* = 3 (Fig. 4.7a), a small amount of induced vorticity [11] (shown by the closed contour lines of $\omega_x W/U_\infty = \pm 0.05$) is formed in the region below the tip vortices. The induced vorticity has an opposite rotation from both the tip vortices and ground plane vortex structures.

This may be caused by an effect similar to a corner induced vortex [42] with the opposite tip vortices acting as “walls” combined with a small interaction by the ground plane vortices on the bottom that whirl in the same direction.

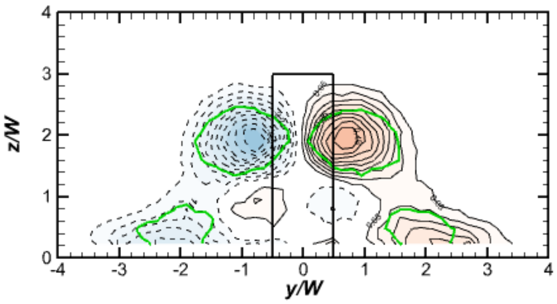

(a) AR = 3

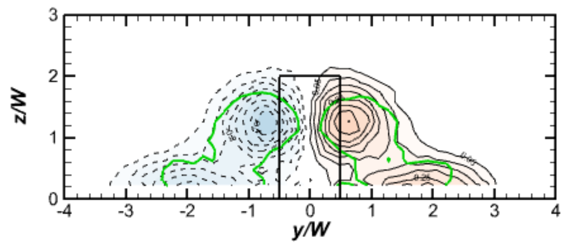

(b) AR = 2

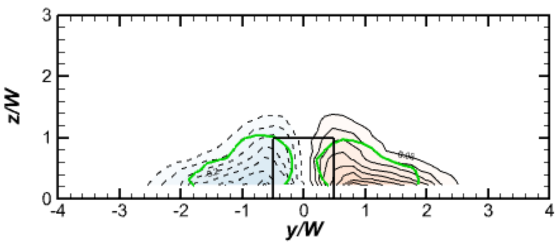

(c) AR = 1

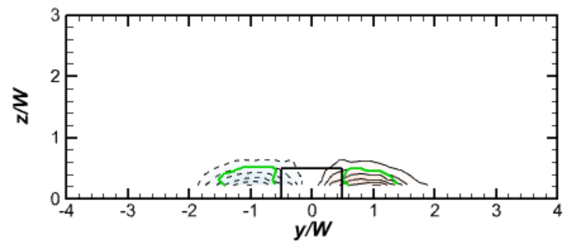

(d) AR = 0.5

Figure 4.7. Mean streamwise vorticity field (contours of $\omega_x W/U_\infty$) in the cross-stream y-z plane with solid green contour lines corresponding to $Q = 0.002$ (identifying streamwise vortices) for 3D rectangular flat plates at $\alpha = 0^o$: (a) $AR = 3$, (b) $AR = 2$, (c) $AR = 1$, and (d) $AR = 0.5$, from the present experiments, Re = 3.8×10^4, $x/W = 6$, $\delta/W = 1.14$. Solid black lines and red coloring represent positive (CCW) vorticity. Dashed black lines and blue coloring represent negative (CW) vorticity.

The Q-criterion [43] is used in Fig. 4.7 and Fig. 4.8 as an indicator of the presence of vortex structures. It relies on the second invariant of the velocity gradient tensor having a positive value ($Q > 0$) and the local pressure being smaller than the ambient pressure (a reasonable assumption if studying a wake) in order to confirm the existence of vortices. To be consistent with [11] a value of $Q = 0.002$ was chosen to identify the main vortex structures. This threshold appropriately distinguished two sets of vortex structures for the flat plate of $AR = 3$ (Fig. 4.7a), one set for $AR = 1$ (Fig. 4.7c) and $AR = 0.5$ (Fig. 4.7d), as well as the merging between the tip vortices and the ground plane vortex structures for $AR = 2$ (Fig. 4.7b). This distinct behavior for $AR = 2$ was noticed earlier in the shape of the recirculation zone boundary, and suggests that the plate of $AR = 2$ may be transitional between two different types of wake flow patterns.

The wake of the finite cylinder of *AR* = 3 (Fig. 4.8a) shows a single pair of circular vortex structures that represent the tip vortices [13]; the "ground plane vortex structures" seen for the 3D flat plate of *AR* = 3 (Fig. 4.7a) are absent. The streamwise location of the finite cylinder wake measurements (at x/W = 6) in Fig. 4.8a compared to the cylinder's recirculation zone length of Lr/W = 3.2 may be the reason why the ground plane vortex structures are absent, as they may have diffused by this location. Another explanation could be the size of the measurement plane employed, which does not extend to the ground plane. The wakes of finite square prisms of *AR* = 5 and *AR* = 7 [11] (not shown here) as well as *AR* = 3 (Fig. 4.8b) denote a similar induced vorticity effect seen for the 3D rectangular flat plate of *AR* = 3 (Fig. 4.7a), where the pair of tip vortices are only barely interacting with the ground plane vortex structures.

The vorticity strength seems to escalate when increasing the height of the bluff bodies. This statement is true for both the 3D flat plates and the finite square prisms for *AR* = 0.5 to 3. Another thing to point out is when comparing both bluff bodies, flat plates tend to have stronger vorticity concentrations compared to square prisms with identical aspect ratios (compare the results presented in Tables 4.1 and 4.2).

The vorticity concentrations of the flat plate of *AR* = 0.5 (Fig. 4.7d) seem to be wider than those of the finite square prism of *AR* = 0.5 (Fig. 4.8e); this relates to the stronger vorticity formed by the flat plate. This difference may also be an effect of the body cross-section on the generation of vorticity in the wake of the body. The wake of the finite square prism of *AR* = 0.5 also shows some additional and unique streamwise vorticity concentrations in the upper wake at x/W = 2 and 4 (not clearly shown in Fig. 4.8e). These structures, which are of opposite sense of rotation from the main streamwise vortex structures, are not present in the wake of the 3D flat plate (Fig. 4.7d), implying that the afterbody shape of the prism may cause their development due to the interaction of the vortex structures with the top face of the square block. At x/W = 6 both bluff bodies have a single pair of streamwise vortices nearly attached to the ground plane (noting that the seven-hole probe could not perform measurements very close to the ground plane).

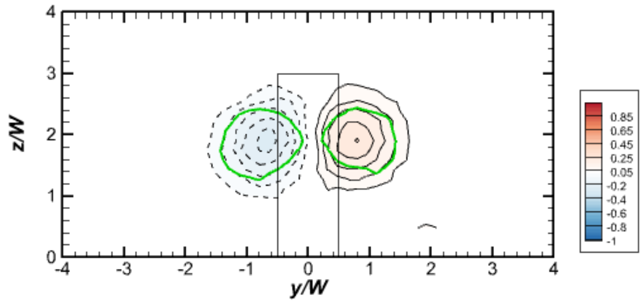

(a) Finite cylinder, AR = 3, x/W = 6

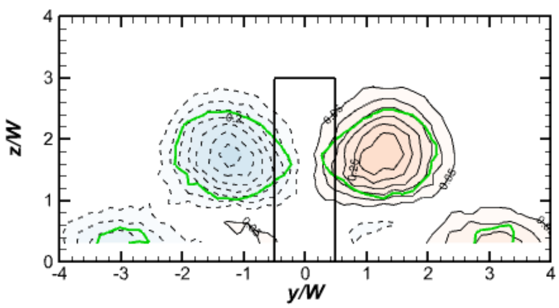

(b) Finite square prism, AR = 3, x/W = 8

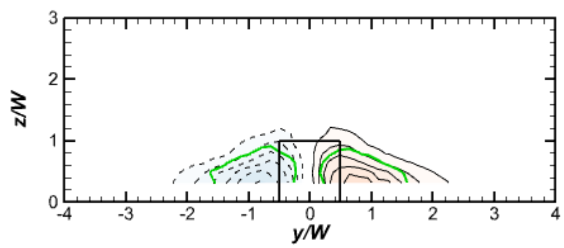

(c) Finite square prism, AR = 1, x/W = 6

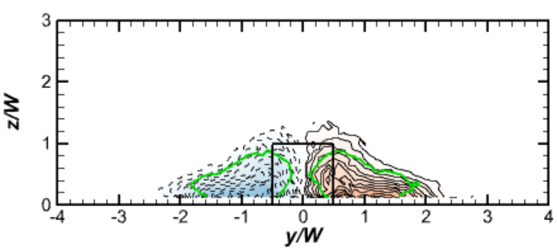

(d) Finite square prism, AR = 1, x/W = 4

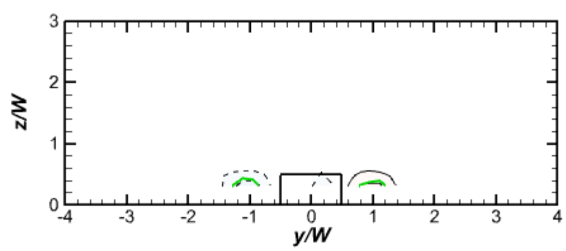

(e) Finite square prism, AR = 0.5, x/W = 6

Figure 4.8. Mean streamwise vorticity field (contours of $\omega_x W/U_\infty$) in the vertical cross-stream (y-z) plane with solid green contour lines corresponding to Q = 0.002 (identifying streamwise vortices): (a) finite cylinder, AR = 3, Re = 6×10^4, δ/W = 2.6, from [13]; (b) finite square prism at α = 0º, AR = 3, Re = 3.7×10^4, δ/W = 1.5, from [11]; (c) finite square prism at α = 0º, AR = 1, Re = 3.7×10^4, δ/W = 1.5, from [12]; (d) finite square prism at α = 0º, AR = 1, Re = 7.5×10^4, δ/W = 0.7, from [15]; (e) finite square prism at α = 0º, AR = 1, Re = 3.7×10^4, δ/W = 1.5, from [12]. Solid black lines and red coloring represent positive (CCW) vorticity. Dashed black lines and blue coloring represent negative (CW) vorticity.

4.3 Flat Plates at an Angle of Incidence

This section summarizes the effects of incidence angle (α) on the wake of the 3D rectangular flat plates of AR = 0.5, 1, 2 and 3. The studied incidence angles range from α = 0° to 90° in intervals of 5° or larger depending on whether the flow was significantly affected by α or not. As depicted in Section 4.1, at $\alpha = 0°$ the flat plate's front face is oriented normal to the freestream and the mean wake is characterized by symmetrical flow separation from the leading edges. At $\alpha = 90°$ the flat plate is parallel to the incoming flow and the wake is extremely thin.

The position of the leading edges with respect to the upstream flow changes when varying α, causing a reshaping of the separating shear layers and the development of the wake overall. The changes come in the form of asymmetry to the pair of streamwise vortex structures. When rotating the plates in the clockwise (CW) direction (looking from the top), the counter clockwise (CCW) vorticity on the right hand (+y) side of the wake becomes dominant.

The experiments were performed at Re = 3.8×10^4 and with a relative boundary layer thickness of $\delta/W \approx 1.14$, the same as the measurements for $\alpha = 0°$ reported in Section 4.2. For these experiments (where α was varied), time-averaged velocity measurements were performed only in the vertical cross-stream (y-z) plane at $x/W = 6$.

4.3.1 Flat Plate of *AR* = 0.5

The results for the flat plate of $AR = 0.5$ are shown in Fig. 4.9. A pair of symmetrical vortex structures, depicted as ground plane vortices, are seen at $\alpha = 0°$ (Fig. 4.9a). This pair of vortices seems to be the cause of the downwash in the middle of the wake and upwash on the outside of the wake. When rotating the flat plate to $\alpha = 5°$ (Fig. 4.9b) the vortex pair becomes slightly asymmetric with the CCW vortex structure on right hand (+y) side starting to slightly displace towards the centre of the plane and growing in size and strength, while the CW vortex on the left hand (-y) side shows an opposite behaviour, reducing in size and strength and appearing to being overtaken by the counter-CCW vortex as the incidence angle increases further. This behaviour is consistent at $\alpha = 10°$, 15°, 20° and 25° (Figs. 4.9c,d,e,f).

Between $\alpha = 25°$ and 30° (Figs. 4.9f,g) a small prominence begins to appear in the CCW vortex structure near the ground plane and far from the plate at around $y/W = 2$. This enlarged region of vorticity keeps growing at $\alpha = 35°$ (Fig. 4.9h) and reaches its maximum size at $\alpha = 40°$ (Fig. 4.9i), almost enough to be considered a small additional vortex structure attached to the growing CCW vorticity (based on the small vortex centre depicted by the green contour line corresponding to Q

= 0.002). At α = 45° (Fig. 4.9j) this small region of vorticity starts to reduce and finally disappears entirely at α = 65° (Fig. 4.9n).

The main CCW vortex grows and reaches its maximum size around α = 40° (Fig. 4.9i). At α = 45° (Fig. 4.9j) the size of the CCW vortex is reduced slightly, however the vortex strength increases dramatically. This trend continues up to between α = 55° (Fig. 4.9l) and 60° (Fig. 4.9m) where the vortex strength reaches its apex. From that point on the mean CCW vortex reduces both in size and strength diminishing up to α = 90° (Fig. 4.9s) where no significant vorticity is present (the small level of vorticity in Fig. 4.9s is attributed to a small misalignment of the plate at α = 90°, noting that the turntable can only rotate the plate within 0.25°).

The CW vortex structure on the left hand ($-y$) of the wake becomes very small as the incidence angle increases, and it vanishes entirely at α = 80° (Fig. 4.9q) where only the CCW structure remains. Between α = 80° (Fig. 4.9q) and 85° (Fig. 4.9r) the remaining main CCW vortex presents a behaviour similar to a wing tip vortex structure produced by a finite wing of very low *AR* and span (at an angle of attack of 10° and 5°, respectively), based on its location (nucleus at the leading edge) and overall circular shape.

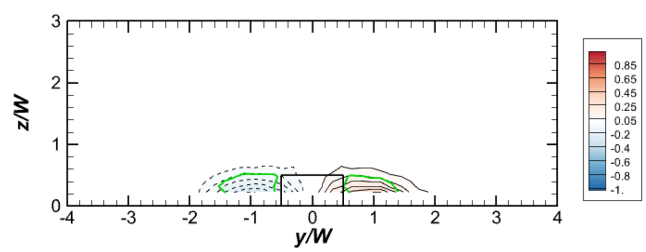

(a) α = 0°

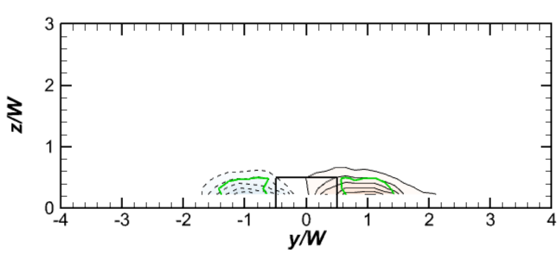

(b) α = 5°

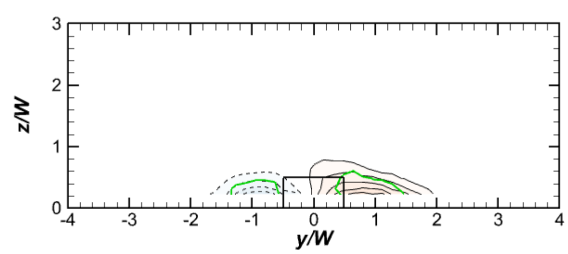

(c) α = 10°

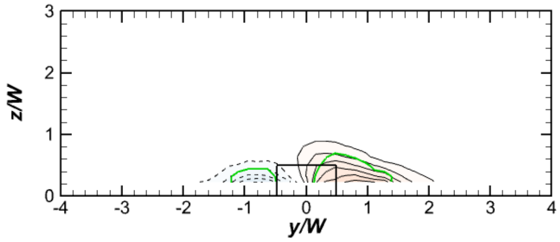

(d) α = 15°

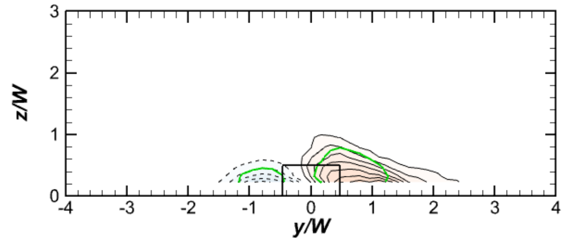

(e) α = 20°

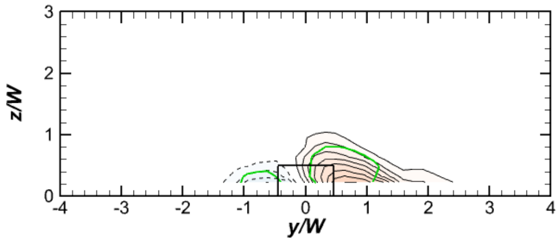

(f) α = 25°

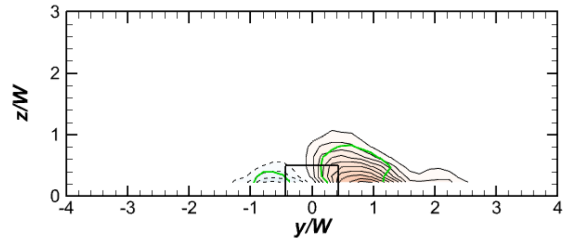

(g) α = 30°

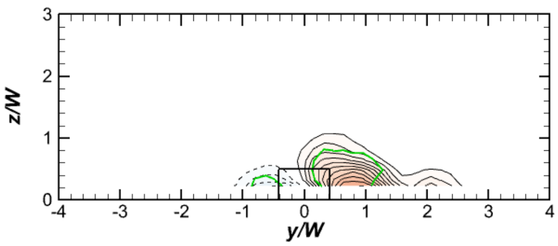

(h) α = 35°

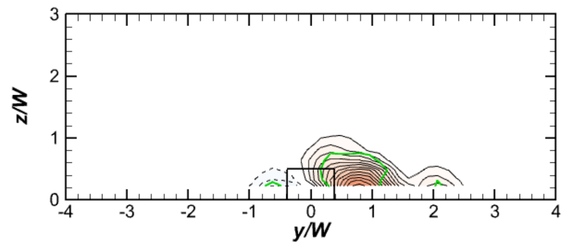

(i) α = 40°

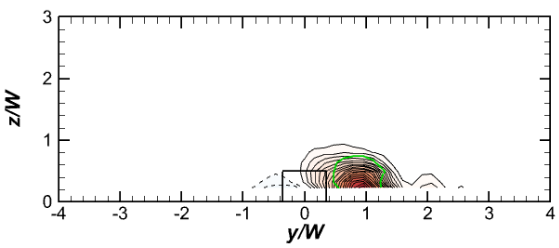

(j) α = 45°

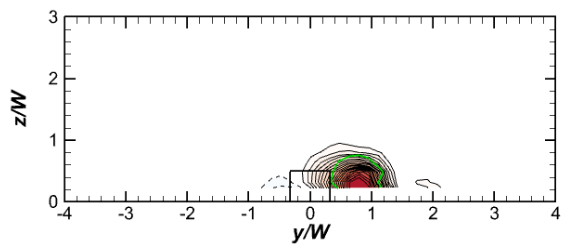

(k) α = 50°

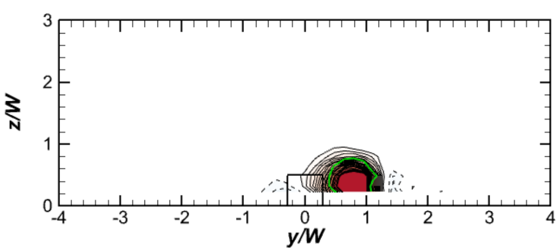

(l) α = 55°

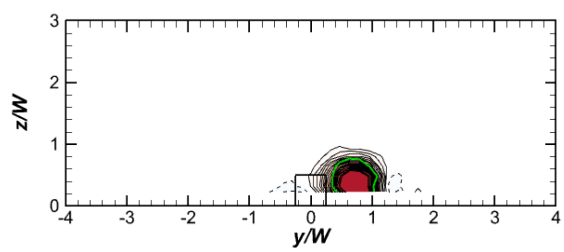

(m) α = 60°

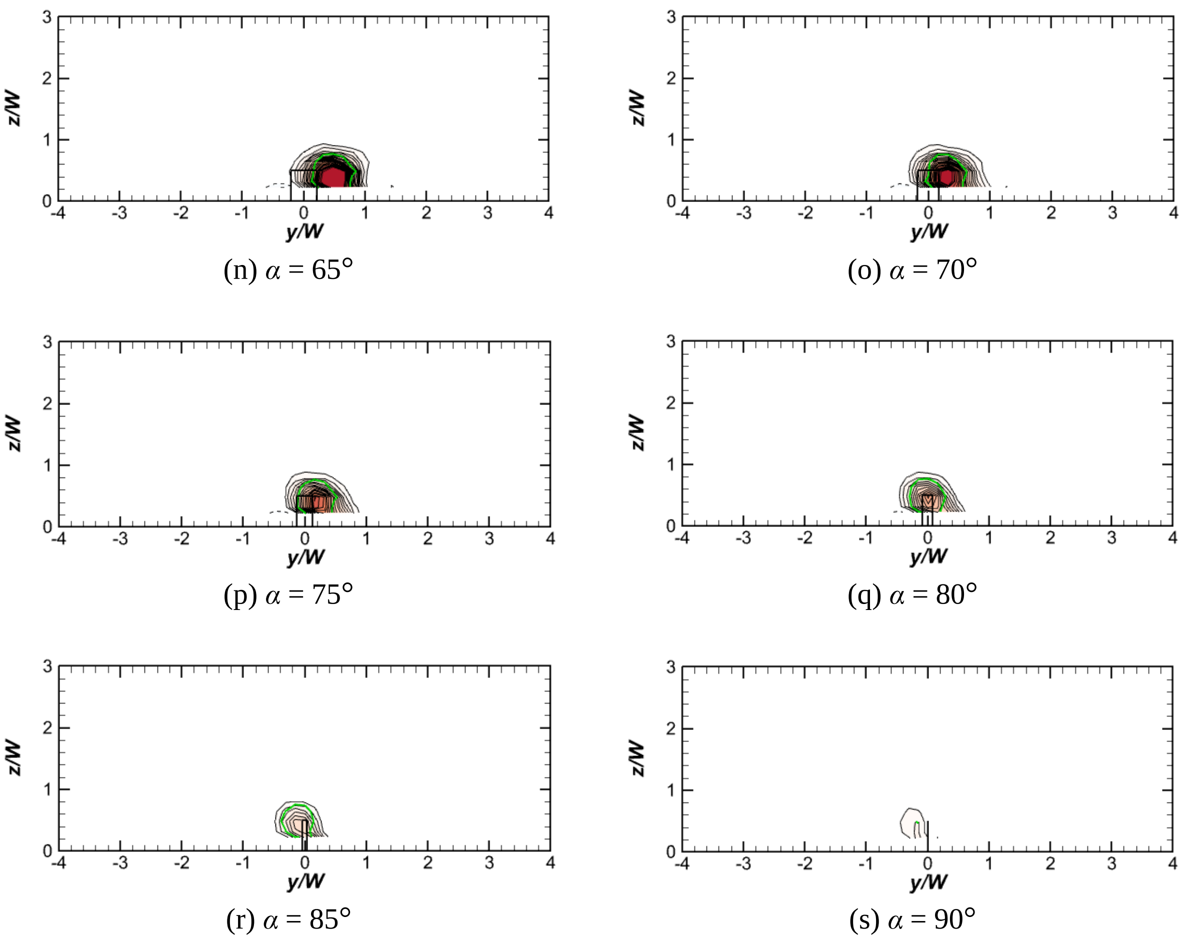

Figure 4.9. Mean streamwise vorticity field (contours of $\omega_x W/U_\infty$) in the vertical cross-stream (*y*-*z*) plane with solid green contour lines corresponding to Q = 0.002 (identifying streamwise vortices) for a 3D rectangular flat plate of *AR* = 0.5: (a) α = 0º, (b) α = 5º, (c) α = 10º, (d) α = 15º, (e) α = 20º, (f) α = 25º, (g) α = 30º, (h) α = 35º, (i) α = 40º, (j) α = 45º, (k) α = 50º, (l) α = 55º, (m) α = 60º, (n) α = 65º, (o) α = 70º, (p) α = 75º, (q) α = 80º, (r) α = 85º, and (s) α = 90º from the present experiments, Re = 3.8×10^4, x/W = 6, δ/W = 1.14. Solid black lines and red coloring represent positive (CCW) vorticity. Dashed black lines and blue coloring represent negative (CW) vorticity.

As depicted in Chapter 4.2, the 3D flat plate of *AR* = 0.5 at an incidence angle of α = 0º shows a symmetric wake boundary with a single peak in the velocity profile. Figure 4.10 shows the in-plane velocity components v (horizontal) and w (vertical), which are normalized by the freestream velocity (as v/U_∞ and w/U_∞) as well as the development of the wake boundary when rotating the flat plate of AR = 0.5 in the CW direction.

At α = 0º (Fig. 4.10a) there is a strong downwash in the mid-section (y/W = 0) of the wake above the height of the flat plate with its peak at z/H = 1.53. When rotating the flat plate in the CW direction the maximum upwash concentrates on the $+y$ side of the plane and steadily increases while maximum downwash stays around the centerline of the flow and near to the ground plane. Figure 4.10l and 4.10m, corresponding to α = 55º and 60º, respectively, show the largest asymmetry for the wake boundary with a single peak on the $+y$ side of the plane and the sharpest slump on the $-y$ side of the wake. This pronounced asymmetry coincides with both the maximum downwash and upwash w/U_∞ (Fig. 4.17), the maximum vorticity $\omega_x W/U_\infty$ (Fig. 4.18), and the largest velocity deficit $(u/U_\infty)_{\min}$ of all the incidence angles (Fig. 4.19) for AR = 0.5. This behaviour could be linked to a critical incidence angle, however further studies focusing on the drag coefficient C_D, lift coefficient C_L, and vortex shedding frequency St, are necessary to confirm this assumption. After α = 60º (Fig. 4.10m) the velocity deficit caused by the flat plate reduces steadily as the wake reverts back into a uniform boundary, where at α = 90º (Fig. 4.10s) the effects on u/U_∞ caused by the flat plate are minimal.

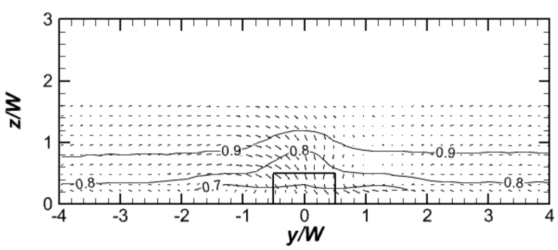

(a) α = 0°

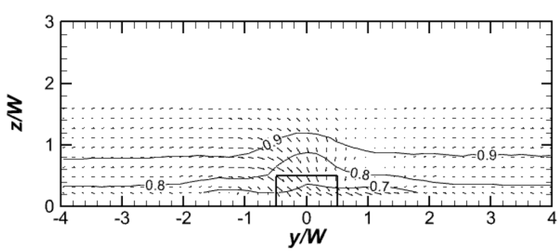

(b) α = 5°

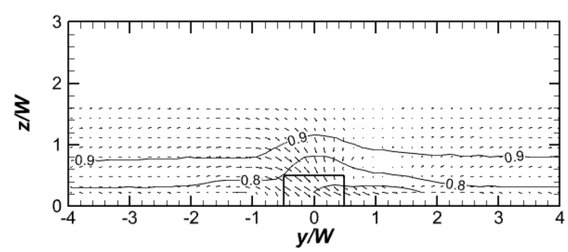

(c) α = 10°

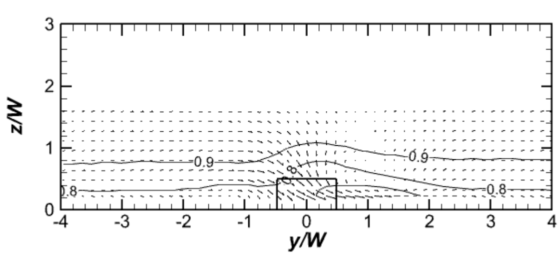

(d) α = 15°

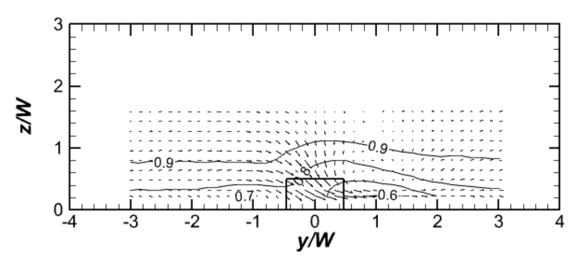

(e) α = 20°

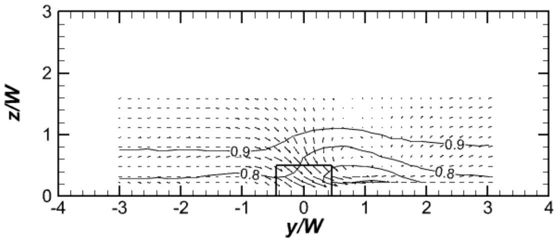

(f) α = 25°

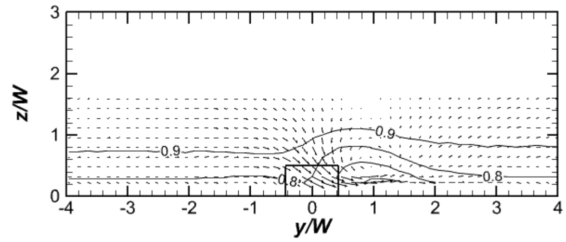

(g) α = 30°

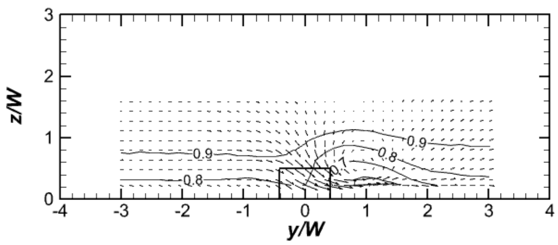

(h) α = 35°

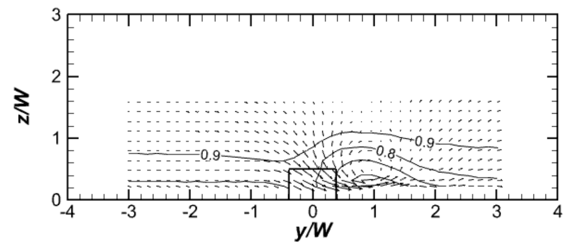

(i) α = 40°

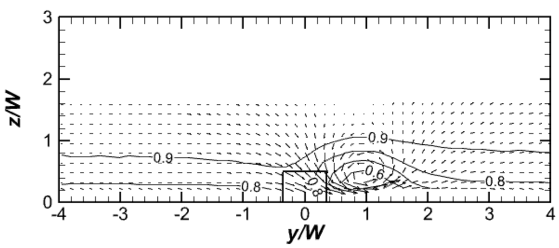

(j) α = 45°

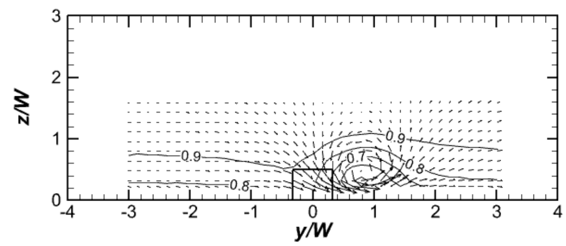

(k) α = 50°

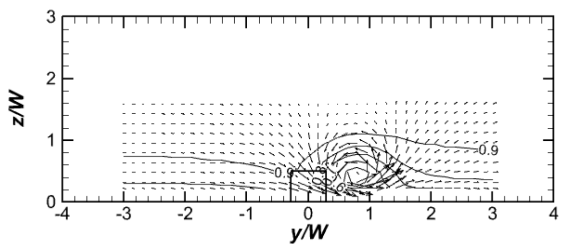

(l) α = 55°

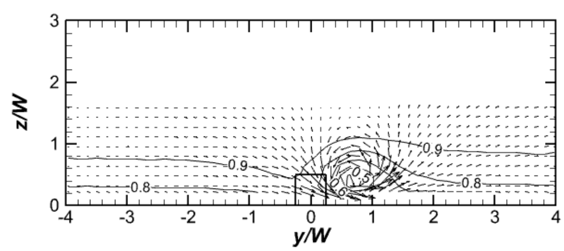

(m) α = 60°

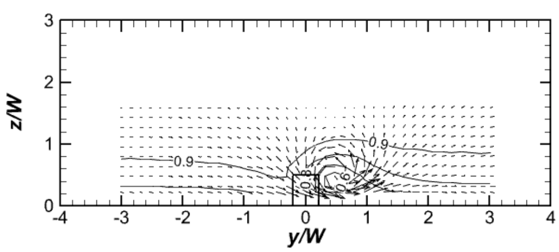

(n) α = 65°

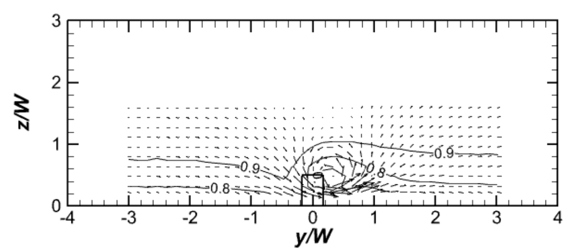

(o) α = 70°

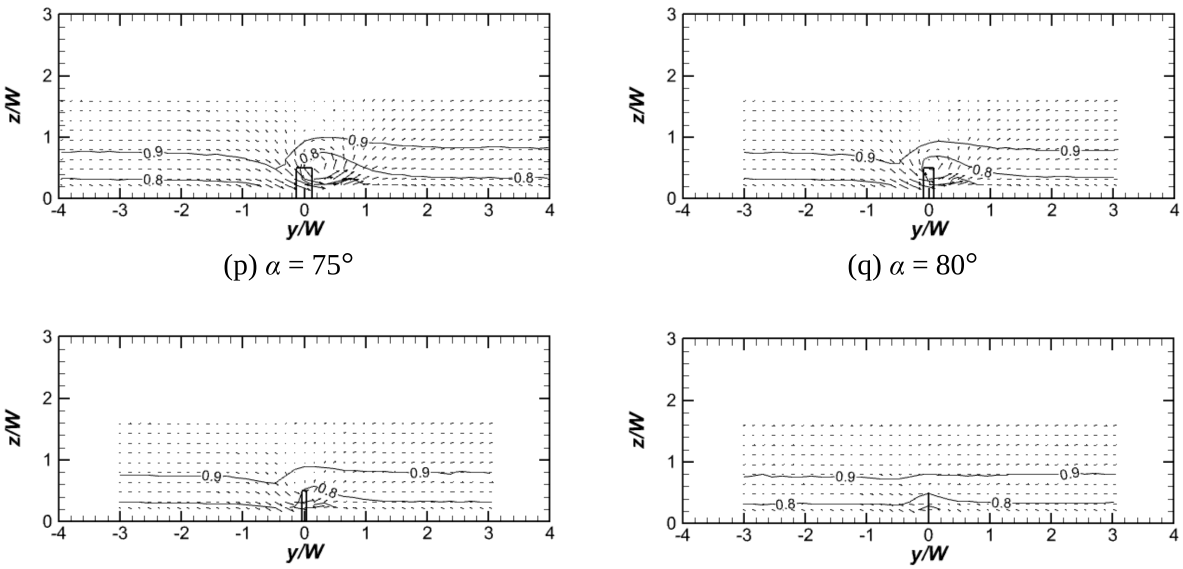

(p) α = 75°
(q) α = 80°
(r) α = 85°
(s) α = 90°

Figure 4.10. Mean velocity vector field (showing in-plane velocity vector components v/U_∞, w/U_∞) with streamwise mean velocity contour lines (u/U_∞), in the vertical cross-stream (y-z) plane, for a 3D flat plate of AR = 0.5: (a) α = 0º, (b) α = 5º, (c) α = 10º, (d) α = 15º, (e) α = 20º, (f) α = 25º, (g) α = 30º, (h) α = 35º, (i) α = 40º, (j) α = 45º, (k) α = 50º, (l) α = 55º, (m) α = 60º, (n) α = 65º, (o) α = 70º, (p) α = 75º, (q) α = 80º, (r) α = 85º, and (s) α = 90º, from the present experiments, Re = 3.8×10^4, x/W = 6, δ/W = 1.14.

4.3.2 Flat Plate of *AR* = 1

At an incidence angle of α = 0º, the wake of the flat plate of AR = 1 (Fig. 4.11a) at x/W = 6 exhibits two symmetric streamwise vortex structures similar to the flat plate of AR = 0.5 (Fig. 4.9a), however the vortices are much larger, slightly stronger (Table 4.1) and shaped differently with a concave edge on the outside region of the vortex as depicted in Fig. 4.7c.

The symmetric arrangement of the streamwise vortex structures at α = 0º is disrupted when increasing the incidence angle (Fig. 4.11). The change in the counter-rotating vortex structures is moderate with small increases in α, showing a similar trend to the flat plate of AR = 0.5 (Fig. 4.9). For α = 5º (Fig. 4.11b) the CW vortex structure reduces in both size and intensity. This trend continues as α (Fig. 4.11c-n) is changed until its eventual disappearance between α = 70º (Fig. 4.11o) and 75º (Fig. 4.11p) where no noticeable CW vorticity is present. When considering the Q criterion, where Q = 0.002 is indicated by a green contour line, this CW streamwise vortex structure fades entirely between α = 45º (Fig. 4.11j) and 50º (Fig. 4.11k).

Meanwhile, the CCW streamwise vortex structure appears to cross slightly from the +y side of the wake towards the centreline of the flow and grows in size and strength. The Q = 0.002 contour line distinguishes a change of this distinct vortex structure from a concave shape on the outside at around the midsection for α = 0º (Fig. 4.11a) to a circular vortex at α = 20º (Fig. 4.11e). Another feature to point out is the brief appearance of a small amount of CCW vorticity separated from the main streamwise vortex, similar to what is seen for the flat plate of AR = 0.5, between α = 65º (Fig. 4.11n) with and 70º (Fig. 4.11o).

Overall, the main CCW streamwise vortex structure reaches its peak size between α = 40º and 50º (Fig. 4.11i-k). At α = 55º (Fig. 4.11l) the vortex starts narrowing while increasing more dramatically its vortex strength. At around α = 65º (Fig. 4.11n) the main CCW vortex structure starts detaching from the ground plane and follows the position of the leading edge located the closest to the upstream flow. It is believed it behaves like a wing tip vortex influenced by the interaction of the separated flow of the shear layer with the leading edge of the flat plate. This vortex structure reaches its maximum strength at α = 70º (Fig. 4.11o), only to reduce both in strength and size from α = 75º to α =85º (Figs. 4.11p-r).

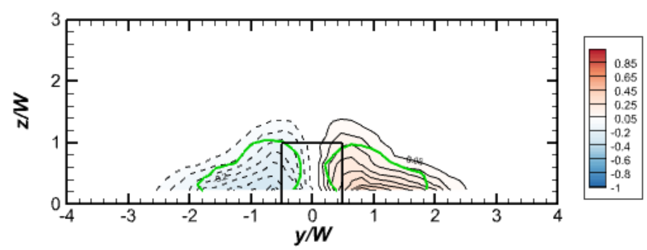

(a) α = 0°

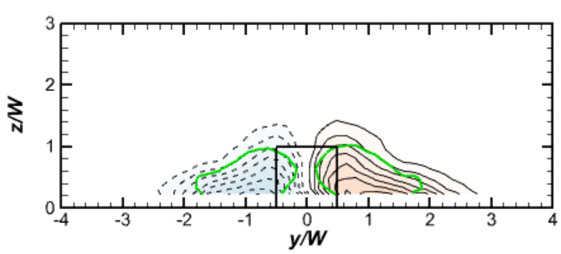

(b) α = 5°

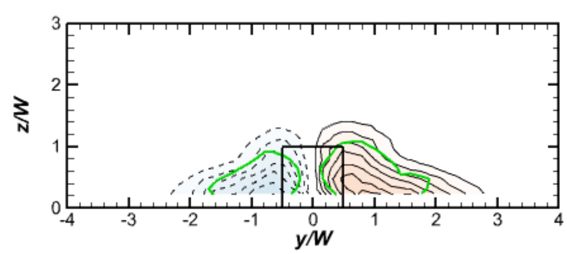

(c) α = 10°

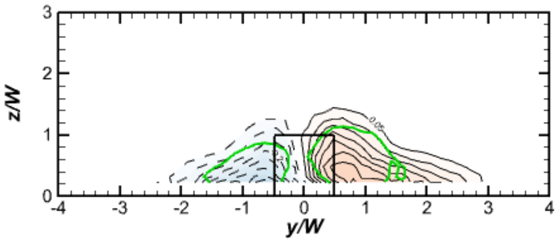

(d) α = 15°

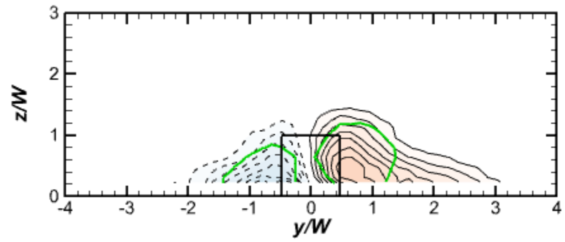

(e) α = 20°

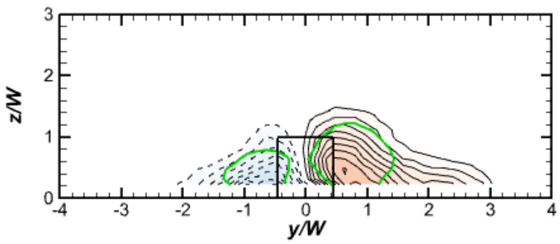

(f) α = 25°

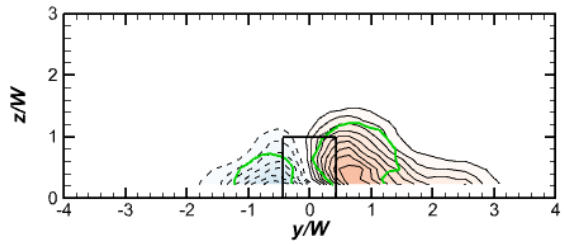

(g) α = 30°

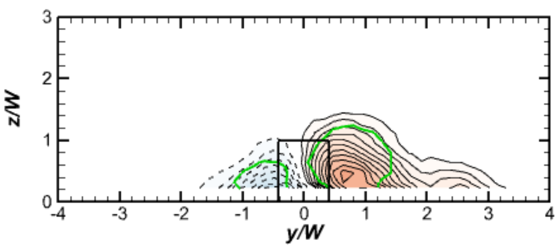

(h) α = 35°

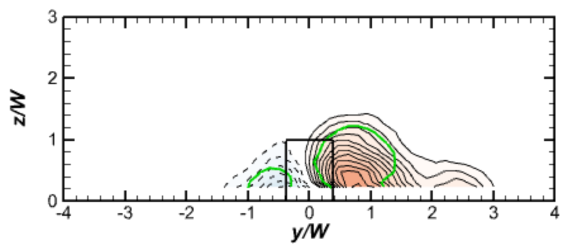

(i) α = 40°

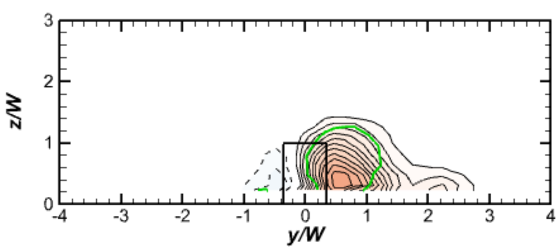

(j) α = 45°

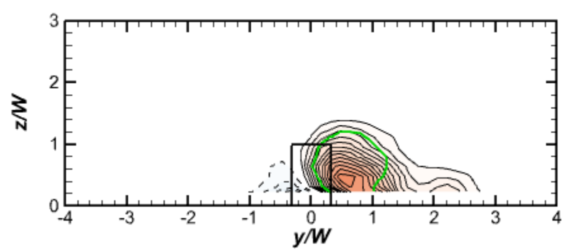

(k) α = 50°

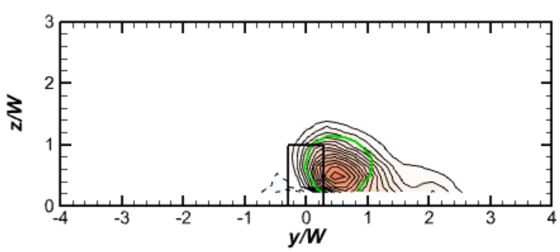

(l) α = 55°

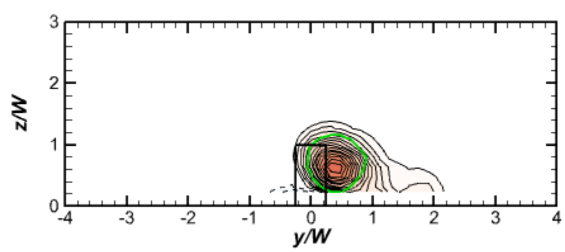

(m) α = 60°

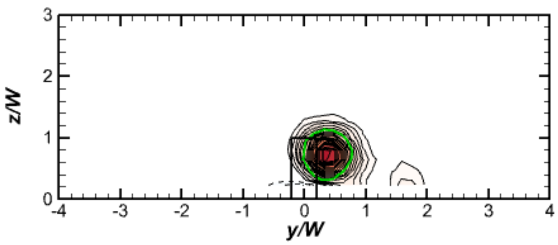

(n) α = 65°

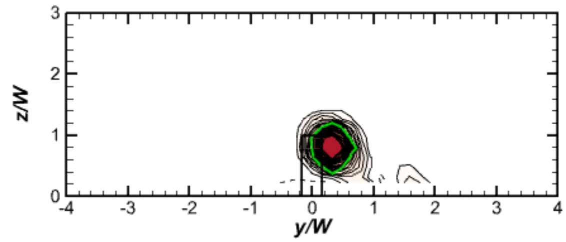

(o) α = 70°

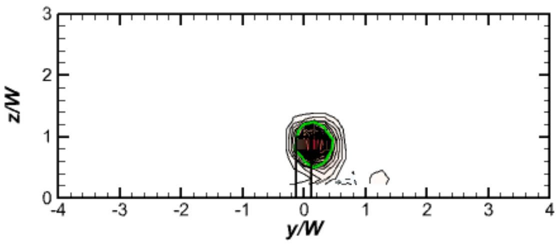

(p) α = 75°

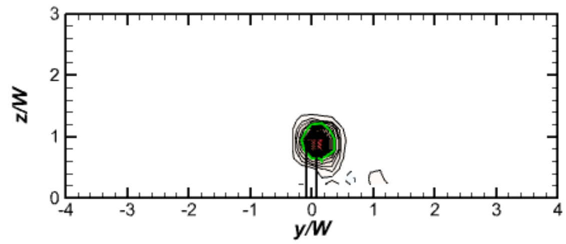

(q) α = 80°

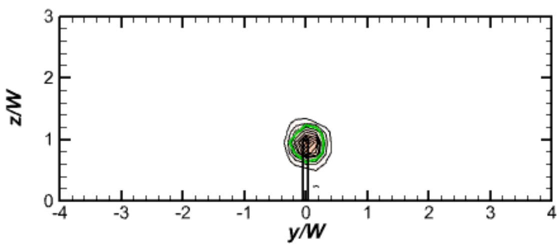

(r) α = 85°

Figure 4.11. Mean streamwise vorticity field (contours of $\omega_x W/U_\infty$) in the vertical cross-stream (y-z) plane with solid green contour lines corresponding to Q = 0.002 (identifying streamwise vortices) for a 3D rectangular flat plate of AR = 1: (a) α = 0º, (b) α = 5º, (c) α = 10º, (d) α = 15º, (e) α = 20º, (f) α = 25º, (g) α = 30º, (h) α = 35º, (i) α = 40º, (j) α = 45º, (k) α = 50º, (l) α = 55º, (m) α = 60º, (n) α = 65º, (o) α = 70º, (p) α = 75º, (q) α = 80º, and (r) α = 85º from the present experiments, Re = 3.8×10^4, x/W = 6, δ/W = 1.14. Solid black lines and red coloring represent positive (CCW) vorticity. Dashed black lines and blue coloring represent negative (CW) vorticity.

Figure 4.12 shows the in-plane velocity components v (horizontal) and w (vertical), which are normalized by the freestream velocity (v/U_∞ and w/U_∞), as well as the development of the wake boundary. As the flat plate is rotated in the CW direction, the upper limit of the wake deflects to the $+y$ side.

The wake boundary of the plate of AR = 1 is similar to the flat plate of AR = 0.5 (Figs. 4.12) with a single peak that shifts to the $+y$ side of the wake as the incidence angle increases. The most noticeable asymmetry occurs between α = 65º and 70º (Fig. 4.12n,o). This coincides with the disappearance of the CW vortex structure, the reshaping of the CCW vortex structure to a circular frame, the appearance of a small amount of CCW vorticity separated from the main vortex (between α = 65º and 70º), the maximum measured vorticity $\omega_x W/U_\infty$ (Fig. 4.18), and the strongest downwash w/U_∞ (Fig. 4.17) at α = 70º (Fig. 4.12o). At larger α, the wake boundary begins to regain its symmetry similar to AR = 0.5 with noticeably smoother u/U_∞ contours.

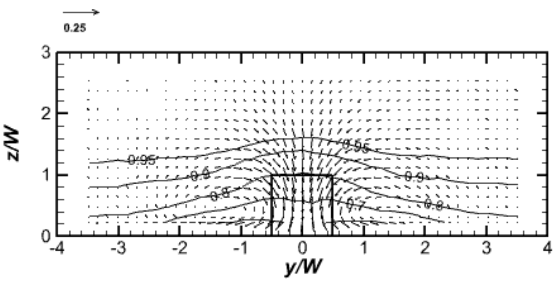

(a) α = 0°

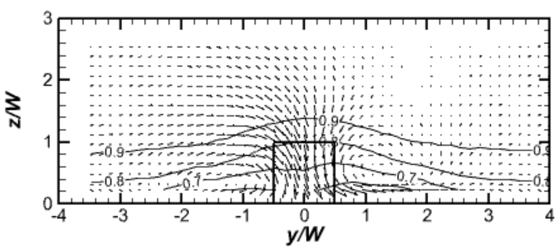

(b) α = 5°

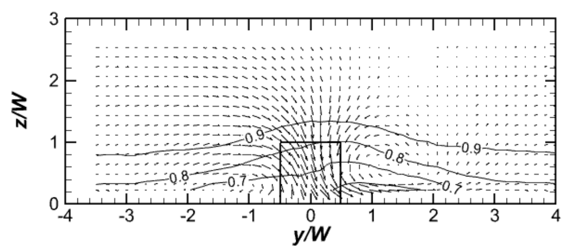

(c) α = 10°

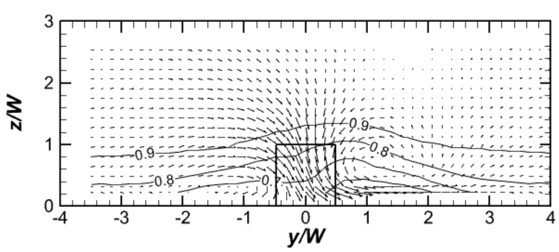

(d) α = 15°

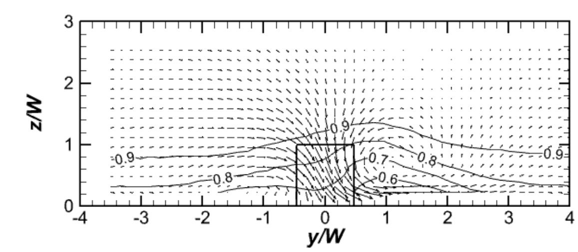

(e) α = 20°

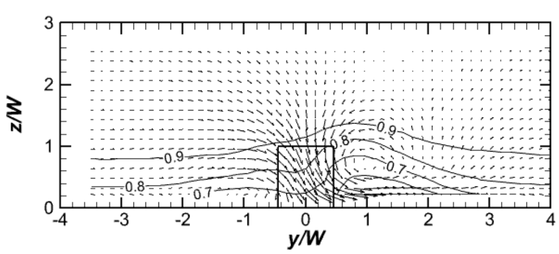

(f) α = 25°

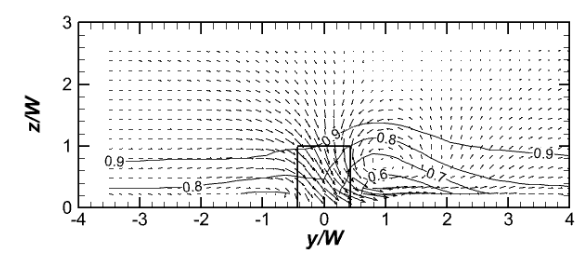

(g) α = 30°

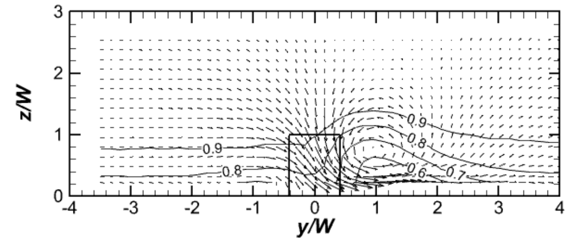

(h) α = 35°

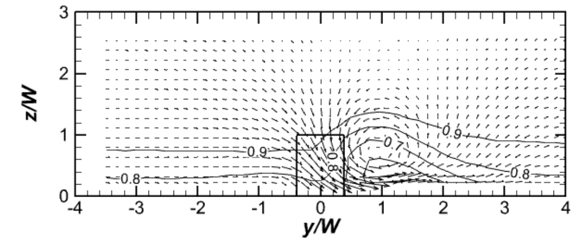

(i) α = 40°

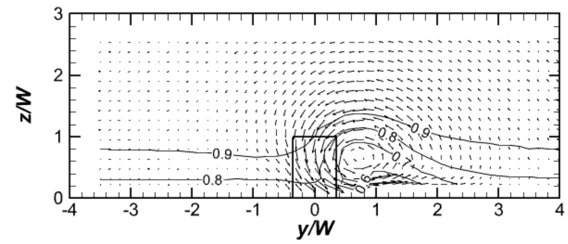

(j) α = 45°

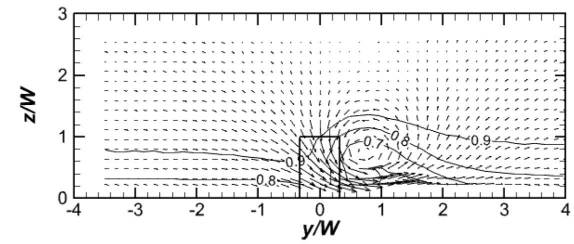

(k) α = 50°

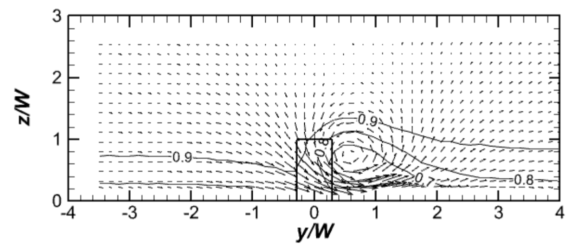

(l) α = 55°

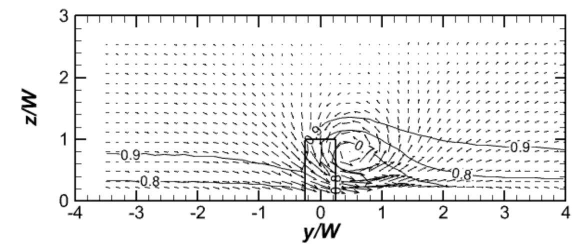

(m) α = 60°

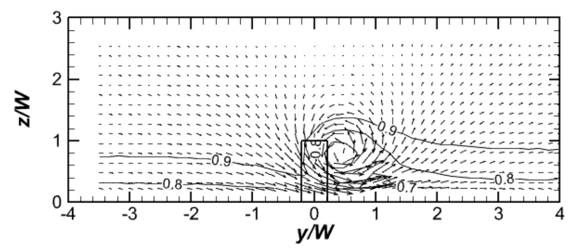

(n) α = 65°

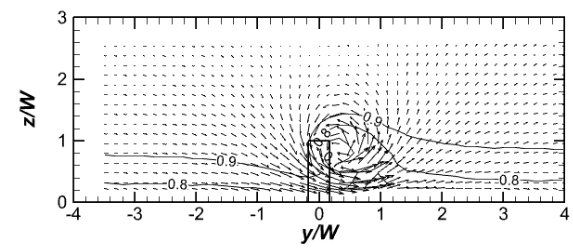

(o) α = 70°

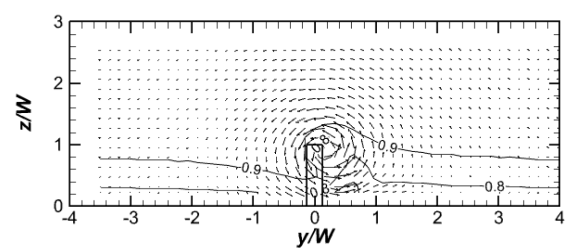

(p) α = 75°

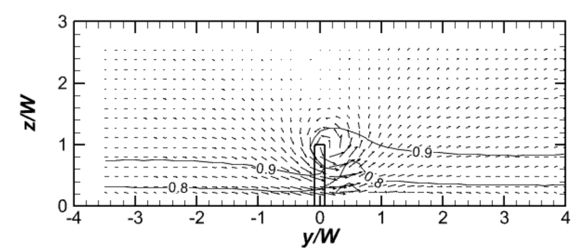

(q) α = 80°

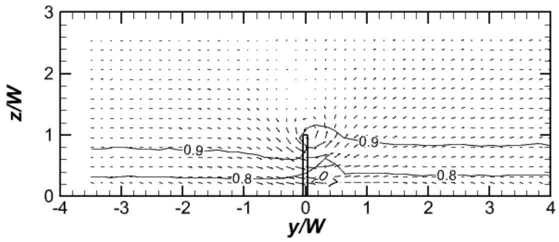

(r) α = 85°

Figure 4.12. Mean velocity vector field (showing velocity vector components v/U_∞, w/U_∞), with streamwise mean velocity contours (u/U_∞), in the vertical cross-stream (*y*-*z*) plane for a 3D flat plate of *AR* = 1: (a) α = 0º, (b) α = 5º, (c) α = 10º, (d) α = 15º, (e) α = 20º, (f) α = 25º, (g) α = 30º, (h) α = 35º, (i) α = 40º, (j) α = 45º, (k) α = 50º, (l) α = 55º, (m) α = 60º, (n) α = 65º, (o) α = 70º, (p) α = 75º, (q) α = 80º, and (r) α = 85º, from the present experiments, Re = 3.8×10^4, x/W = 6, δ/W = 1.14.

As seen from Figs. 4.17 and 4.18 the flat plate of *AR* = 1 shows a trend where both the maximum streamwise CCW vorticity and maximum downwash increase up to α = 70º from where it steadily decreases. The minimum u/U_∞ contours in Fig. 4.19 denote for the case of the flat plate of *AR* = 1 a steady decrease up to α = 35º where then it increases and becomes steady for the rest of the incidence angles except for a small disruption at α = 70º.

4.3.3 Flat Plate of *AR* = 2

The wake of the flat plate of *AR* = 2 contains two sets of main streamwise counter-rotating vortex structures, which is significantly different from what was previously described for the flat plates of *AR* = 0.5 (Section 4.3.1) and *AR* =1 (Section 4.3.2). The development of the vorticity field in the wake at x/W = 6 is shown in Fig. 4.13. It is believed the two contiguous vortex sets correspond to the familiar tip vortices (upper pair of vortices), seen for finite cylinders and square prisms at higher aspect ratios, and the ground plane vortices (lower pair of vortices). The concave shape of the vortex structures for the flat plate of *AR* = 1 (discussed in Section 4.3.2) makes it look as if they come from the merging of both pairs of symmetric streamwise vortex structures present in the wake of the flat plate of *AR* = 2 (which presents both sets of complex vortex structures as in the middle of that merger).

Similar to the previously depicted flat plates, the –*y* side of the wake shows primarily CW vorticity while the +*y* side of the wake presents CCW. The *Q* = 0.002 contour line is again used as a criterion to identify vortex structures, and in Fig. 4.13 it shows the ongoing merging of both vortex structures. At α = 0º (Fig. 4.13a) the wake is symmetric along the centreline (y/W = 0) similar to the rest of the studied plates. At low incidence angles the wake is not very sensitive to changes in α, although the wake becomes asymmetric, as shown for the case of α = 15º (Fig. 4.13b).

The rotation of the flat plate in the CW direction causes an upwards displacement of the CCW tip vortex structure topping the CW tip vortex structure, which is being displaced downwards. This effect starts being more noticeable at α = 30º (Fig. 4.13c), where the CW tip vortex appears to decrease in size and strength while it merges with the CW ground plane vortex structure, due to the downwards displacement, establishing a single weaker CW vortex structure. At the same time, the growing CCW tip vortex begins to separate from the weaker CCW ground plane vortex due to the upwards and centre displacement caused by the increasing incidence angle. This trend continues through α = 45º (Fig. 4.13d) and 50º (Fig. 4.13e).

Between α = 55º (Fig. 4.13f) and 60º (Fig. 4.13g), based on the minimum measurable contour level, the CCW tip vortex structure completely detaches from the weakened ground plane vortex structure while being positioned directly above the now small CW vortex. This tendency continues at α = 65º (Fig. 4.13h) and α = 70º (Fig. 4.13i) where the CW bottom vortex structure is almost extinct as well as the CCW ground vortex. At α = 75º (Fig. 4.13j) and 80º (Fig. 4.13k) the tip vortex is at its apex with its core in the centre of the plane while CW vorticity appears on the +y side of the plane. The cause for this momentary growth of CW vorticity is unknown, however it seems to interact slightly with the tip vortex.

The maximum vorticity $\omega_x W/U_\infty$ (Fig 4.18) for the flat plate of AR = 2 is correlated with the tip vortex structure which grows with an almost exponential tendency reaching its apex at α = 80º only to plunge at higher angles. The maximum downwash (Fig 4.17) shows a gradual decrease up to α = 60º coinciding with the detachment of the CCW tip vortex with the CCW ground plane vortex where it then later increases, reaching its peak at α = 80º, but then plummeting afterwards at a higher α.

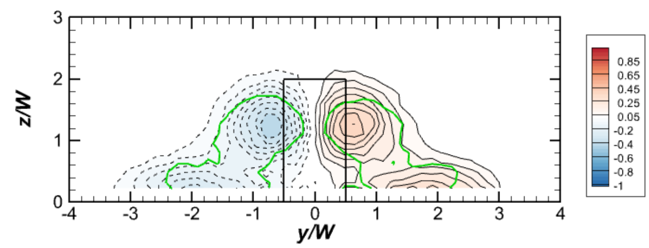

(a) α = 0°

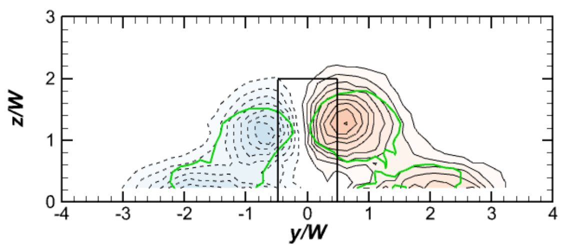

(b) α = 15°

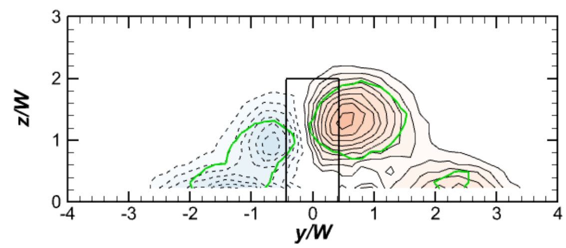

(c) α = 30°

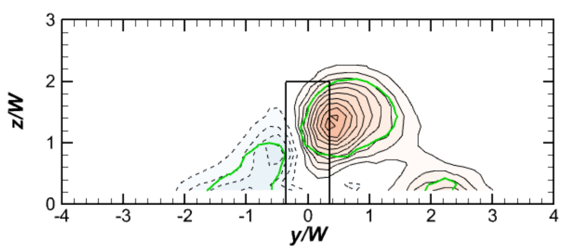

(d) α = 45°

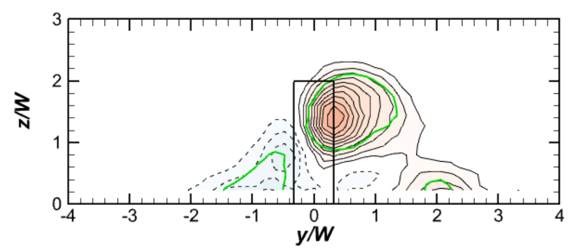

(e) α = 50°

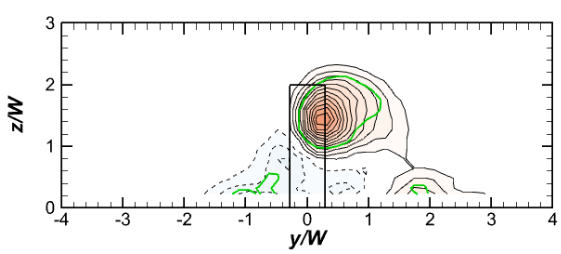

(f) α = 55°

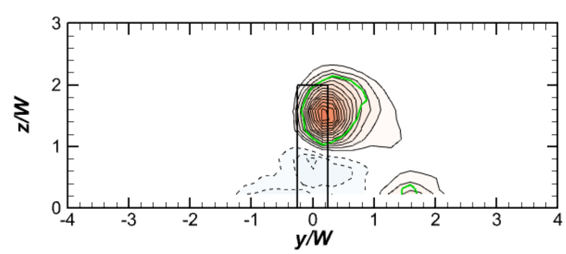

(g) α = 60°

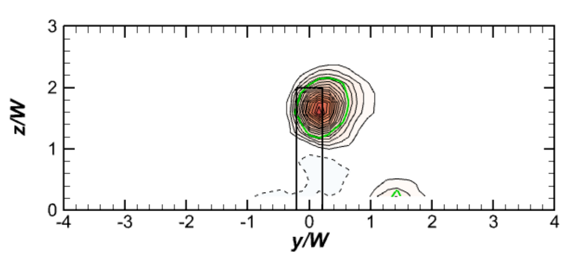

(h) α = 65°

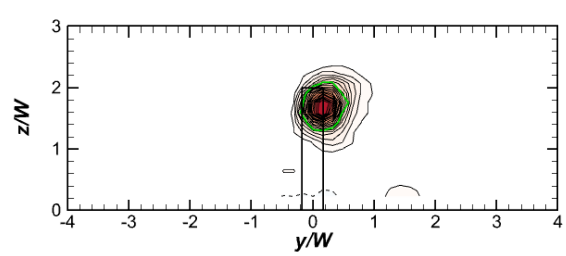

(i) α = 70°

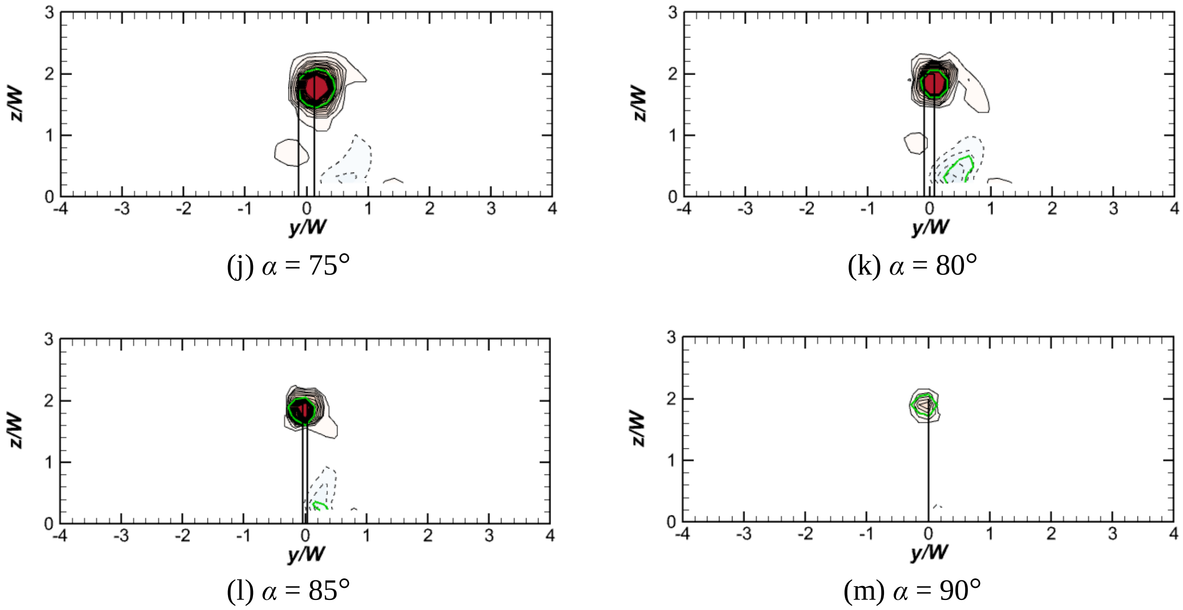

(j) α = 75°   (k) α = 80°

(l) α = 85°   (m) α = 90°

Figure 4.13. Mean streamwise vorticity field (contours of $\omega_x W/U_\infty$) in the vertical cross-stream (y-z) plane with solid green contour lines corresponding to Q = 0.002 (identifying streamwise vortices) for a 3D rectangular flat plate of AR = 1: a) α = 0º, (b) α = 15º, (c) α = 30º, (d) α = 45º, (e) α = 50º, (f) α = 55º, (g) α = 60º, (h) α = 65º, (i) α = 70º, (j) α = 75º, (k) α = 80º, (l) α = 85º, and (m) α = 90º, from the present experiments, Re = 3.8×10^4, x/W = 6, δ/W = 1.14. Solid black lines and red coloring represent positive (CCW) vorticity. Dashed black lines and blue coloring represent negative (CW) vorticity.

The wake boundary for the flat plate of AR = 2 is shown in Fig. 4.14 as the contour of u/U_∞ = 0.9. In the same figure the in-plane velocity components v (horizontal) and w (vertical) normalized by the freestream velocity (v/U_∞ and w/U_∞) are depicted. The wake boundary is similar to the other aspect ratios and denotes a symmetric single peak located at the wake centerline (y/W = 0). Its development with the incidence angle implies a deflection to the +y side of the plane. At the same time the wake thins out denoting sharper edges with the peak adhering to the shape of the more noticeable CCW tip vortex indicated by the velocity vectors. The wake boundary keeps a similar height (z/W = 2, which is the same as the flat plate of AR = H/W = 2) throughout the entire evolution of the wake, up until α = 75º (Fig. 4.14j) to 80º (Fig. 4.14k) where it starts decreasing. For α = 85º and 90º (Figs. 4.14l,m) the effects of the flat plate are minimal and the wake is very small.

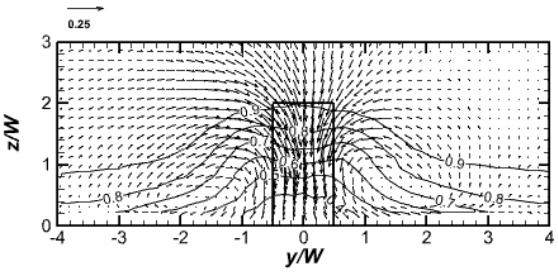

(a) α = 0°

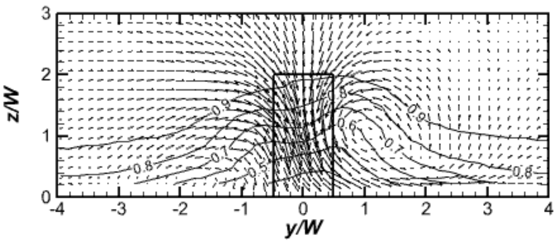

(b) α = 15°

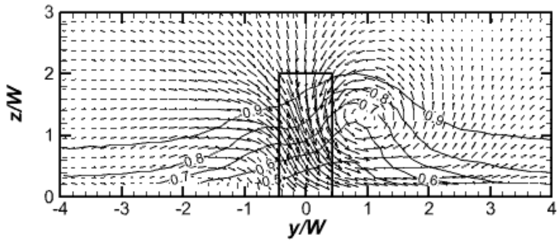

(c) α = 30°

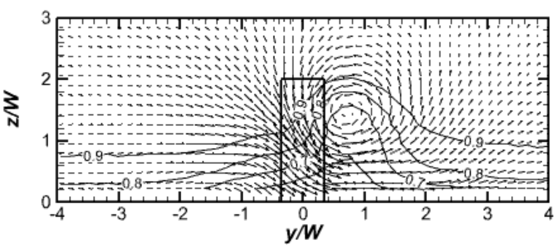

(d) α = 45°

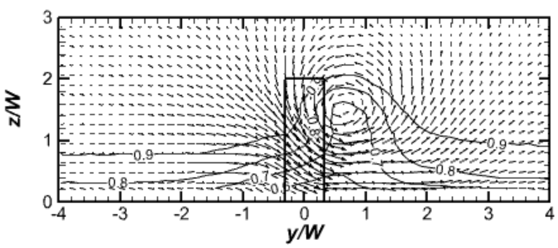

(e) α = 50°

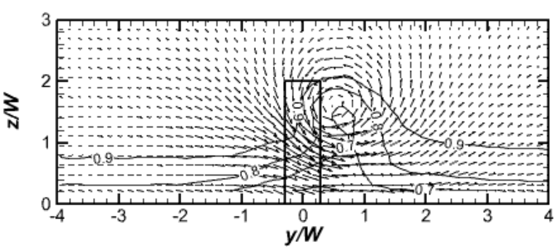

(f) α = 55°

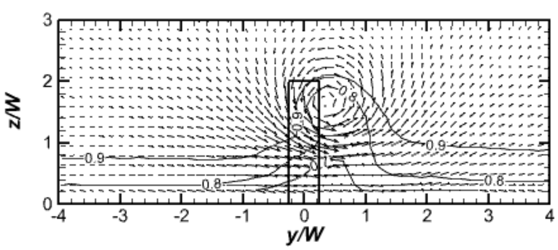

(g) α = 60°

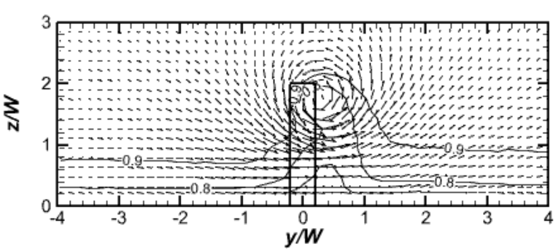

(h) α = 65°

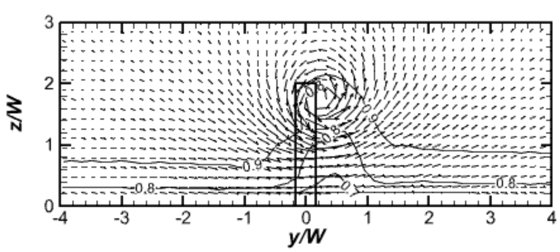

(i) α = 70°

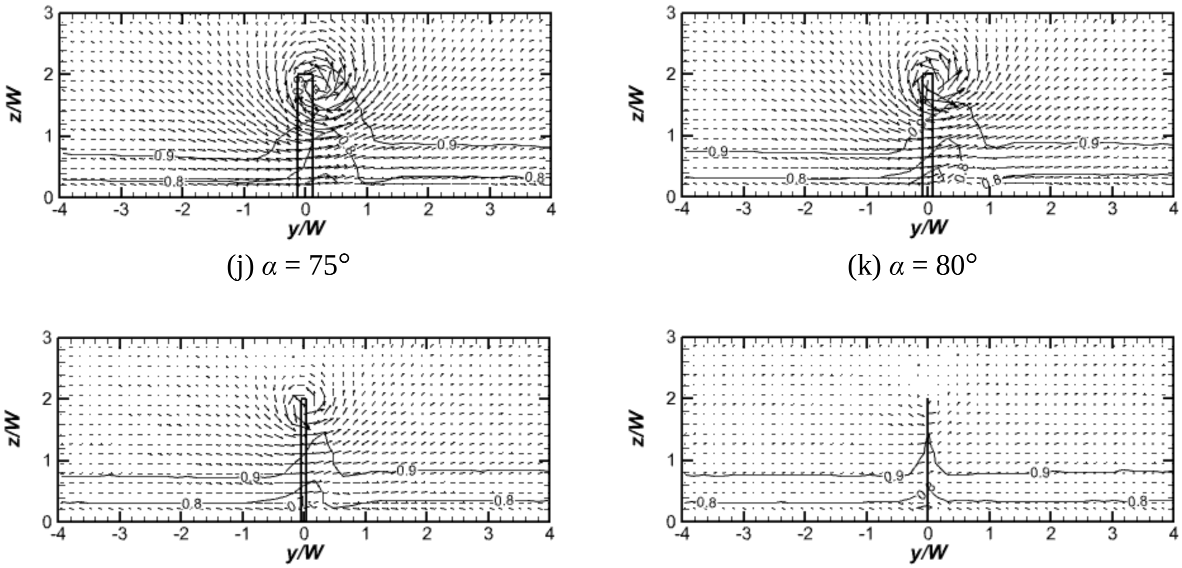

(j) α = 75° (k) α = 80°

(l) α = 85° (m) α = 90°

Figure 4.14. Mean velocity vector field (showing velocity vector components v/U_∞, w/U_∞), with streamwise mean velocity contours (u/U_∞), in the vertical cross-stream (y-z) plane, for a 3D flat plate of AR = 2: (a) α = 0º, (b) α = 15º, (c) α = 30º, (d) α = 45º, (e) α = 50º, (f) α = 55º, (g) α = 60º, (h) α = 65º, (i) α = 70º, (j) α = 75º, (k) α = 80º, (l) α = 85º, and (m) α = 90º, from the present experiments, Re = 3.8×10^4, x/W = 6, δ/W = 1.14.

4.3.4 Flat Plate of *AR* = 3

The case of the flat plate with AR = 3 presents some similarities to the smaller flat plate of AR = 2. Figure 4.15a shows the symmetrical properties of the wake at α = 0º where the streamwise vorticity $\omega_x W/U_\infty$ is shown by the contour lines. Results show the presence of two sets of mirror-like vortices identified as tip vortices (top) and ground plane vortices (bottom), as well as some induced vorticity in between with opposite rotation. This induced vorticity is similar to a corner-induced vortex in a channel, with the opposite tip vortices acting as "walls" combined with the interaction of the ground plane vortices that whirl in the same direction.

The $+y$ side of the wake has a tip vortex and a ground plane vortex both with CCW rotation and shown by solid contour lines and red color. The additional small induced vorticity also located on the $+y$ side of the wake has CW vorticity and is shown by dashed lines and blue color. On the other hand, the $-y$ side of the wake has CW tip and ground plane vortices as well as some induced CCW vorticity.

The development of the mean wake with increasing incidence angle for the flat plate of $AR = 3$ (Fig. 4.15) is similar to $AR = 2$, with the CCW tip vortex moving upwards and to the centre of the plane while the opposite CW tip vortex goes downwards and towards the centreline. The induced CW vorticity located at the $+y$ side of the wake grows as the CCW tip vortex separates from the contiguous CCW ground plane vortex. Additionally, the CCW induced vorticity on the $-y$ side of the wake shrinks due to the increasingly smaller gap between the CW tip and ground plane vortices, which leaves less space for it to expand. This is first noted at $\alpha = 15^{\circ}$ (Fig. 4.15b) and it follows the same development at $\alpha = 30^{\circ}$ (Fig. 4.15c) where the induced vorticity grows enough to touch the ground plane. Both ground plane vortices are diminished as α increases.

At $\alpha = 45^{\circ}$ (Fig. 4.15d) the CW tip vortex starts merging with the growing induced vorticity located on the $+y$ side of the wake near the centerline, while the CCW tip vortex almost detaches entirely from its respective ground plane vortex. The detachment of the CCW tip vortex finally occurs at $\alpha = 50^{\circ}$ (Fig. 4.15e) and at the same time the CW tip vortex positions itself beneath while both ground plane vortices steadily reduce in size. The CW tip vortex and the induced vorticity on the $+y$ side of the wake are fully merged at $\alpha = 55^{\circ}$ (Fig. 4.15f) and simultaneously it separates entirely from the CW ground plane vortex. Between $\alpha = 55^{\circ}$ (Fig. 4.15f) and 60° (Fig. 4.15g) the CCW tip vortex gets significantly stronger, while the CW tip vortex loses strength. New CCW induced vorticity starts appearing on the $-y$ side of the wake between the fading CW tip vortex and its respective ground plane vortex. Between $\alpha = 65^{\circ}$ (Fig. 4.15h) and 70° (Fig. 4.15i) the induced CCW vortex structure gains some strength and is placed below the CW tip vortex, which is underneath the stronger CCW tip vortex creating a vertical "chain" of counter-rotating vorticity. Some minor CW induced vorticity is located next to the CCW induced vorticity, slightly on the $+y$ side of the wake and interacting with the vortex trail. At this point the ground plane vortices are almost non-existent. At $\alpha = 75^{\circ}$ (Fig. 4.15j) and $\alpha = 80^{\circ}$ (Fig. 4.15k) the maximum streamwise vorticity corresponding to the top CCW tip vortex reaches its peak (Fig. 4.18) while the CW tip vortex and the induced CCW vorticity start disappearing. The previously mentioned CW induced vorticity placed at the very bottom reaches the ground plane and grows slightly. At $\alpha = 85^{\circ}$ (Figure 4.15l) the CW tip vortex and the induced CCW vorticity below disappear entirely and only the top CCW tip vortex and the ground CW induced vortices remain. By this point they extend somewhat vertically as if both vortex formations were interacting with each other, similar to AR = 2 at the same α. When α = 90º (Figure 4.15m) only the weakened CCW tip vortex remains.

Regarding the maximum streamwise vorticity, it stays somewhat constant up to α = 45º after which it increases almost exponentially with increasing α. The maximum vorticity attained for the flat plate of AR = 3 occurs within the CCW tip vortex at α = 80º, after which it decreases dramatically tending towards zero. The maximum downwash also occurs at this same incidence angle, similar to the results of the flat plate of AR = 2.

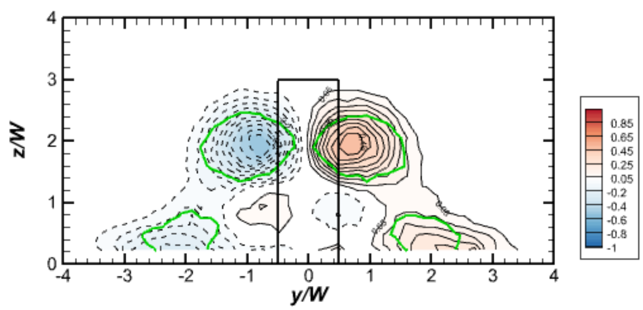

(a) α = 0°

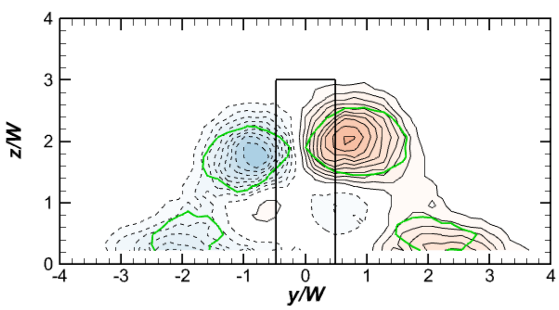

(b) α = 15°

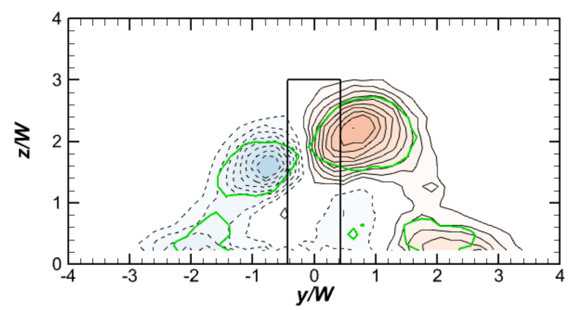

(c) α = 30°

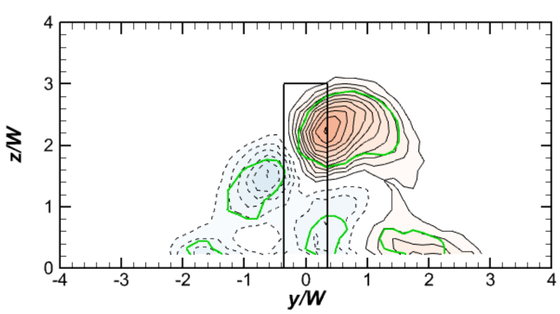

(d) α = 45°

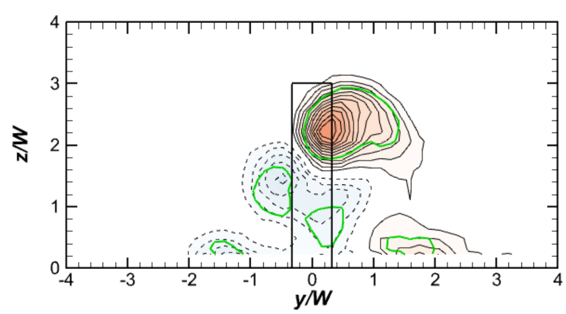

(e) α = 50°

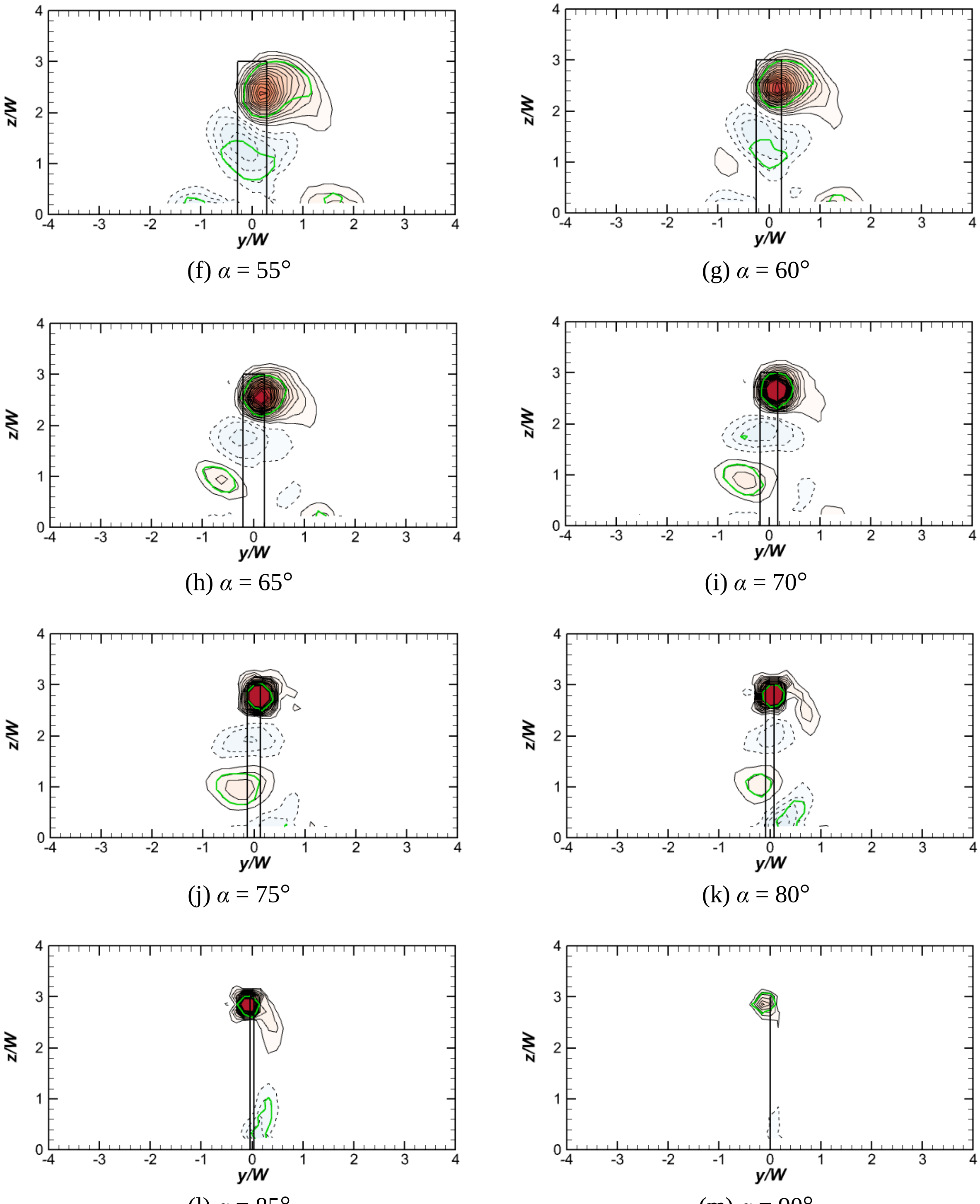

(f) $\alpha = 55°$ (g) $\alpha = 60°$

(h) $\alpha = 65°$ (i) $\alpha = 70°$

(j) $\alpha = 75°$ (k) $\alpha = 80°$

(l) $\alpha = 85°$ (m) $\alpha = 90°$

Figure 4.15. Mean streamwise vorticity field (contours of $\omega_x W/U_\infty$) in the vertical cross-stream (y-z) plane at $x/W = 6$,, with solid green contour lines corresponding to $Q = 0.002$ (identifying streamwise vortices), for a 3D rectangular flat plate of $AR = 3$: (a) $\alpha = 0°$, (b) $\alpha = 15°$, (c) $\alpha = 30°$, (d) $\alpha = 45°$, (e) $\alpha = 50°$, (f) $\alpha = 55°$, (g) $\alpha = 60°$, (h) $\alpha = 65°$, (i) $\alpha = 70°$, (j) $\alpha = 75°$, (k) $\alpha = 80°$, (l) $\alpha = 85°$, (m) $\alpha = 90°$, from present experiments, Re = 3.8×10^4, $\delta/W = 1.14$. Solid black lines and red coloring represent positive (CCW) vorticity. Dashed black lines and blue coloring represent negative (CW) vorticity.

The wake boundary at $x/W = 6$ shows symmetric characteristics and a single peak at $\alpha = 0^\circ$ (Fig. 4.16a). For $AR = 3$ the wake is taller (extending to $z/W = 3$) and slightly wider ($y/W = 4.2$) than the smaller flat plates. A strong region of downwash can be perceived along the wake's centerline ($y/W = 0$) with no apparent significant upwash.

Similar to the rest of the flat plates, the wake deflects to the $+y$ side of the wake when increasing the incidence angle α. The change is very gradual and the first incidence angle at where this is noticeable is $\alpha = 15^\circ$ (Fig. 4.16b). At $\alpha = 30^\circ$ (Fig. 4.16c) there is now a change in the peak in the wake boundary that is now located on the $+y$ side. The asymmetry increases from $\alpha = 45^\circ$ to 70° (Figs. 4.16d to 4.16i) while the wake reduces in width. Between $\alpha = 75^\circ$ (Fig. 4.16j) and 80° (Fig. 4.16k) the wake boundary starts recovering its symmetry while reducing its height and width. Finally at $\alpha = 90^\circ$ (Fig. 4.16m) the wake is fully symmetric once again and the flow is only disturbed by the very small thickness of the flat plate; here, the perceived effects are almost negligible.

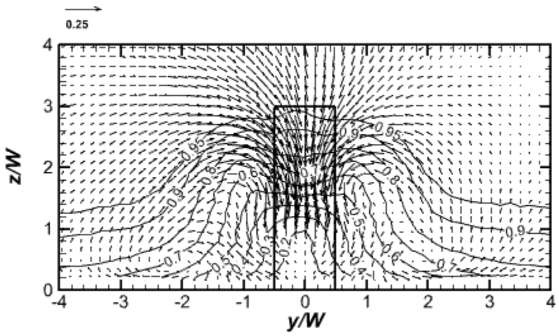

(a) α = 0°

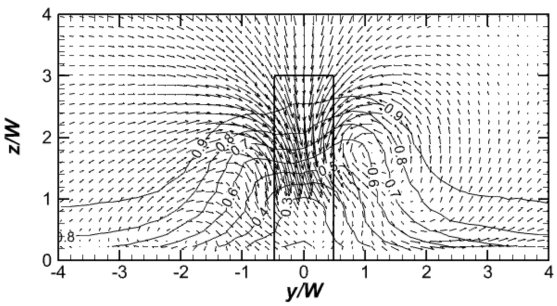

(b) α = 15°

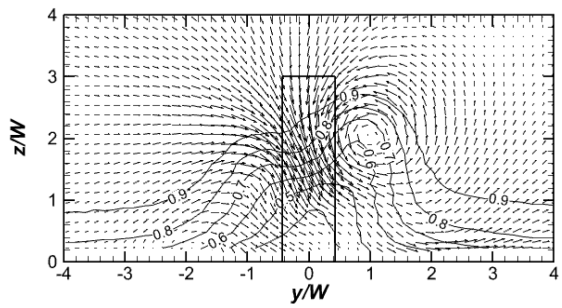

(c) α = 30°

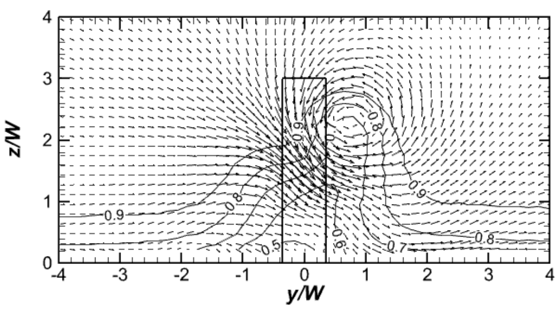

(d) α = 45°

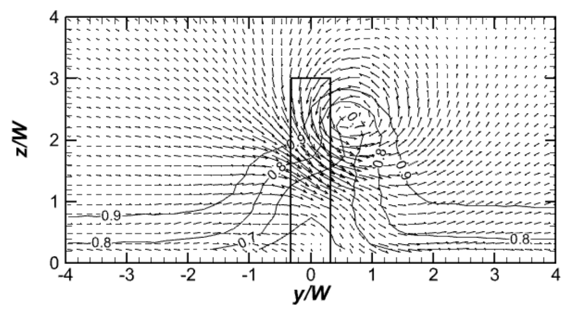

(e) α = 50°

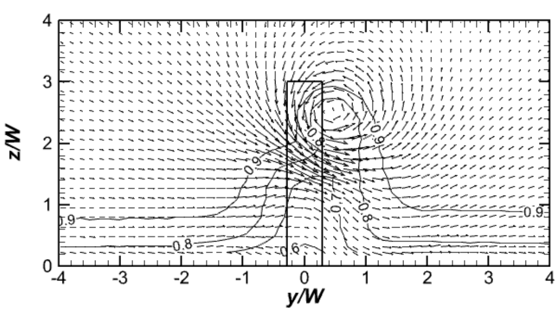

(f) α = 55°

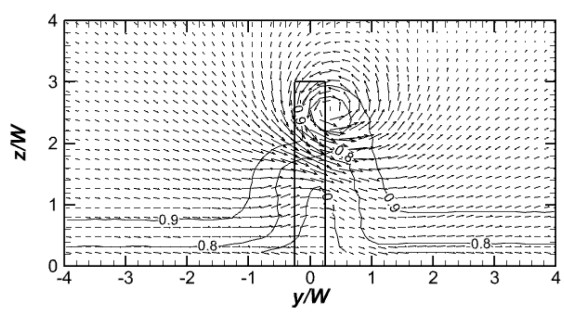

(g) α = 60°

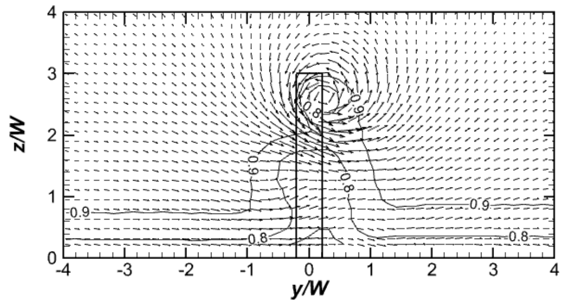

(h) α = 65°

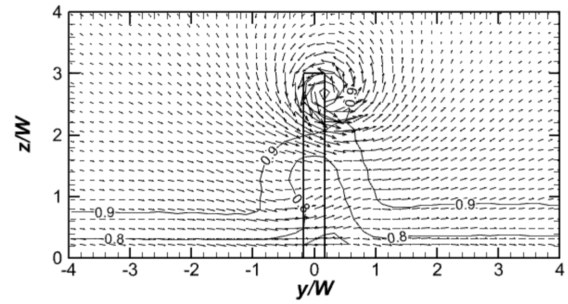

(i) α = 70°

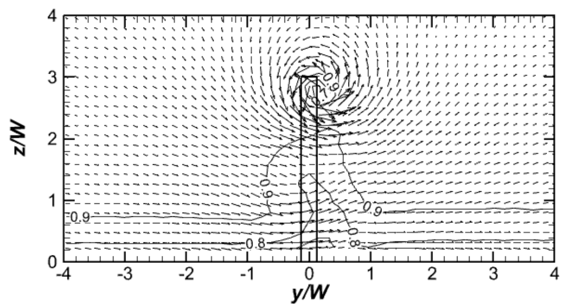

(j) α = 75°

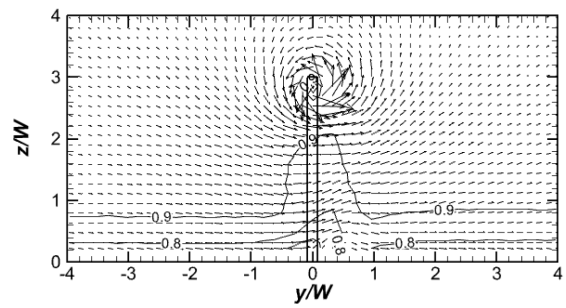

(k) α = 80°

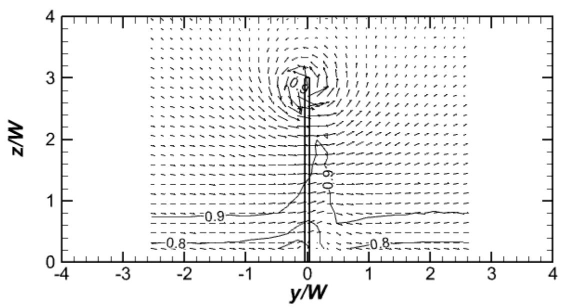

(l) α = 85°

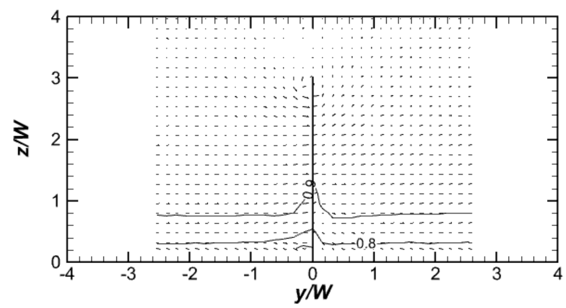

(m) α = 90°

Figure 4.16. Mean velocity vector field (showing velocity vector components v/U_∞ and w/U_∞) with streamwise mean velocity contours (u/U_∞) in the vertical cross-stream (y-z) plane at x/W = 6, for a 3D rectangular flat plate of AR = 3. (a) α = 0º, (b) α = 15º, (c) α = 30º, (d) α = 45º, (e) α = 50º, (f) α = 55º, (g) α = 60º, (h) α = 65º, (i) α = 70º, (j) α = 75º, (k) α = 80º, (l) α = 85º, (m) α = 90º, from present experiments, Re = 3.8×10^4, δ/W = 1.14.

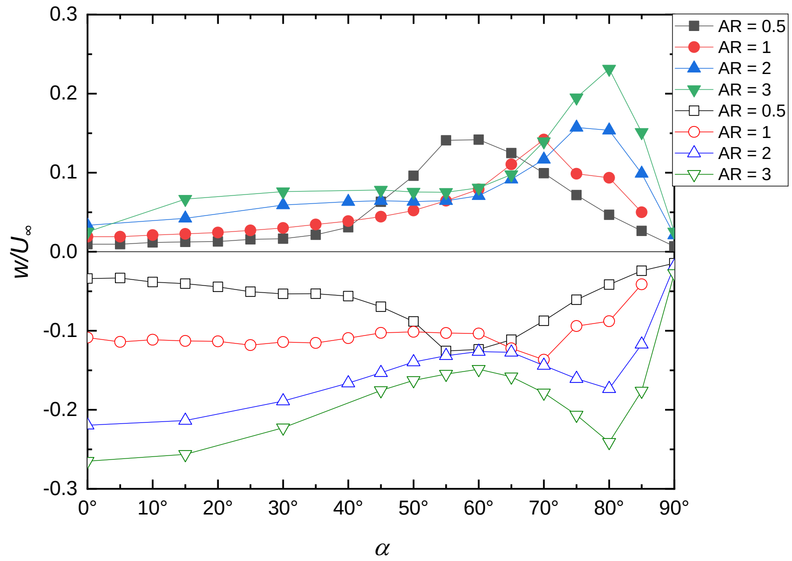

Figure 4.17. Maximum upwash (solid symbols) and maximum downwash (open symbols) w/U_∞ for flat plates of (a) AR = 3, (b) AR = 2, (c) AR = 1, and (d) AR = 0.5 at different incidence angles (α), from the present experiments, Re = 3.8×10^4, x/W = 6, δ/W = 1.14.

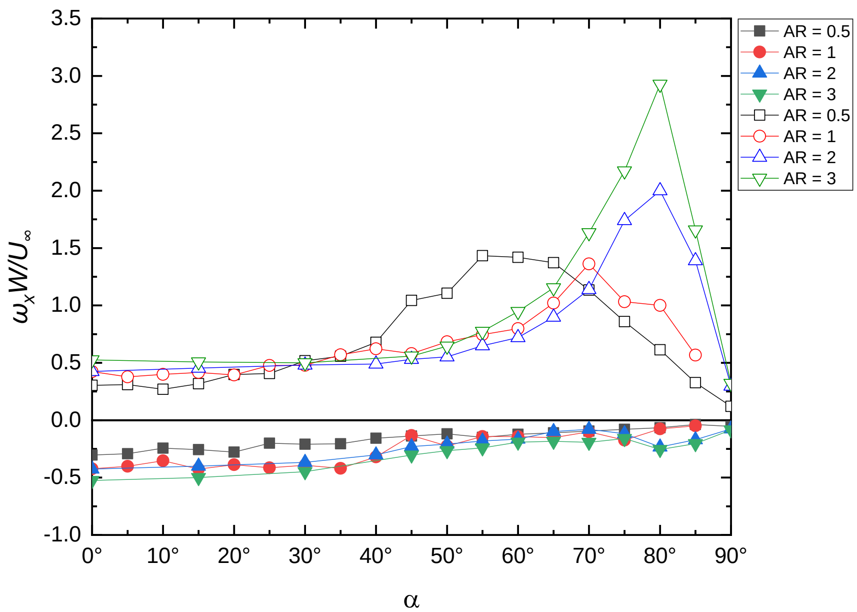

Figure 4.18. Maximum streamwise vorticity $\omega_x W/U_\infty$ in the CW (solid symbols) and CCW (open symbols) directions for flat plates of (a) AR = 3, (b) AR = 2, (c) AR = 1, and (d) AR = 0.5 at different incidence angles (α), from the present experiments, Re = 3.8×10^4, x/W = 6, δ/W = 1.14.

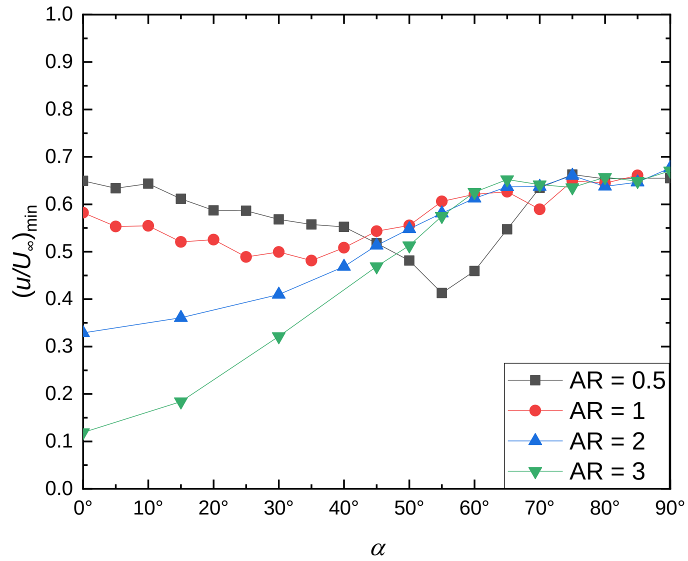

Figure 4.19. Minimum streamwise velocity $(u/U_\infty)_{\min}$ for flat plates of (a) *AR* = 3, (b) *AR* = 2, (c) *AR* = 1, and (d) *AR* = 0.5 at different incidence angles (α), from the present experiments, Re = 3.8×10^4, $x/W = 6$, $\delta/W = 1.14$.

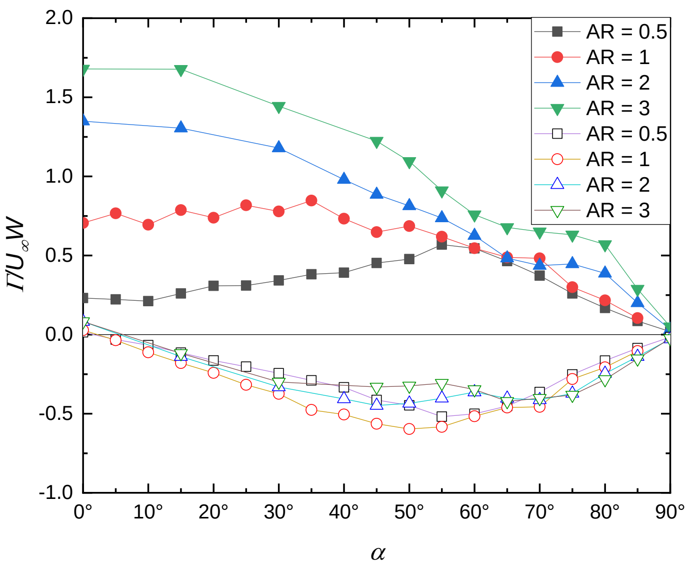

Figure 4.20. Total strength (solid) and strength difference (unfilled) of normalized circulation $\Gamma/(U_\infty W)$ between CW and CCW vorticity for flat plates of *AR* = 3, *AR* = 2, *AR* = 1, and *AR* = 0.5 at different incidence angles (α) from present experiments, Re = 3.8×10^4, $x/W = 6$, $\delta/W = 1.14$.

The total strength was determined by adding the amount of CW and CCW vorticity (absolute values) over the measured area that exceeded the minimum measurable contour. At small α the total circulation strength increases with *AR* (Fig. 4.20). The total strength for the flat plate of *AR* = 0.5 increases slightly with incidence angle up to α = 55º where it reaches its maximum, and thereafter it steadily decreases until reaching zero. The case of the flat plate with *AR* = 1 shows a similar pattern where the total strength is consistent and then diminishes starting from α = 35º. In contrast, the flat plate of *AR* = 2 shows a peak strength at α = 0º that steadily decreases with increasing incidence angle. The case of the flat plate with *AR* = 3 shows a fairly similar pattern to *AR* = 2 starting with its largest total circulation when the flat plate is normal to the flow and decreasing with incidence angle.

The strength difference between the CW and CCW vorticity (Fig. 4.20) behaves in a similar way for all four aspect ratios, with the greatest difference reached around α = 50º, only to decrease when increasing α from that point.

4.3.5 Flat Plates of *AR* = 0.5 and 3 and Comparison with Finite Square Prism

The finite square prism of *AR* = 0.5 depicted in Figs. 4.21 and 4.22 shows several differences from the flat plate with the same aspect ratio. It should be noted the flow conditions for the square prism and flat plate are different, the Reynolds number using the width as reference for the square prism is Re = 7.3×10^4 while for the flat plate Re = 3.8×10^4, the relative boundary layer thickness for the square prism is δ/W = 1.61 and for the flat plate is δ/W = 1.14. The distance downstream where the *y*-*z* plane measurements were performed is also different for both bluff bodies: the wake measurements for the finite square prism were taken at x/W = 3 while for the flat plate at x/W = 6.

The first noticeable difference at *AR* = 0.5 are the two pairs of streamwise vortex structures located close to the centerline for the square prism at α = 0º (Fig. 4.21a). The outer pair can be identified as ground plane vortex structures similar to the flat plate (Fig. 4.21e), however the induced inner vorticity concentrations (with opposite rotation from the ground plane vortices) may be attributed to the interaction of the ground plane vortex structures with the top *x*-*y* face of the square prism.

When the square prism is rotated to α = 15º (Fig. 4.21b) the induced vorticity concentrations become less distinguishable and weaker to the point they are almost gone, while the ground plane vortices become stronger and reach their most noticeable asymmetry. The negative CW vorticity becomes stronger and larger on the –y side of the wake and takes on a distinctive shape with a concave region on the outside section. At α = 30º (Fig. 4.21c) the asymmetry becomes less noticeable with both CW and CCW ground plane vortices seemingly starting to split up into two sets of vortex structures. At α = 45º (Fig. 4.21d) the wakes denote a mirror-like formation of vortex structures, with seemingly two pairs of complex vortex structures that seem much stronger than what is seen at α = 0º (Fig 4.21a). In contrast the flat plate wake increasingly shifts towards the +y side of the plane with the CCW positive ground plane vortex gaining strength while the negative CW ground plane vortex diminishes considerably. Overall, the flat plate exhibits a very different behaviour with the wake increasingly becoming more asymmetric from α = 0º to 45º (Fig. 4.21d-h), where the CCW positive ground plane vortex becomes increasingly larger as α progresses, taking a distinctive shape with a concave outside region, while the CW negative ground plane vortex loses strength and size while moving downwards. Vorticity concentrations for the flat plate are much weaker than those of the square prism. Further analysis on the flat plate for larger α is was presented earlier in Section 4.31.

Finite Square Prism, x/W = 3 | Flat Plate, x/W = 6

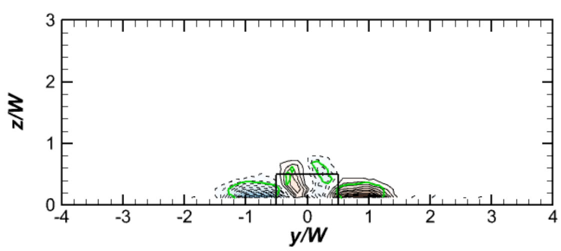

(a) α = 0°

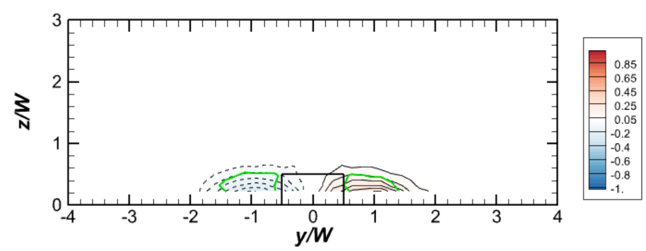

(e) α = 0°

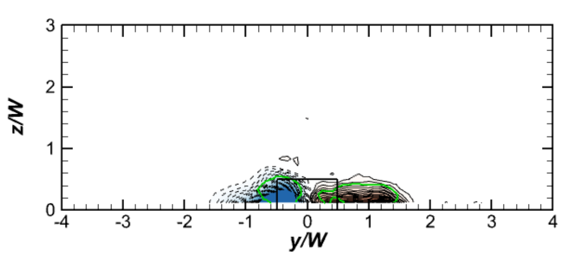

(b) α = 15°

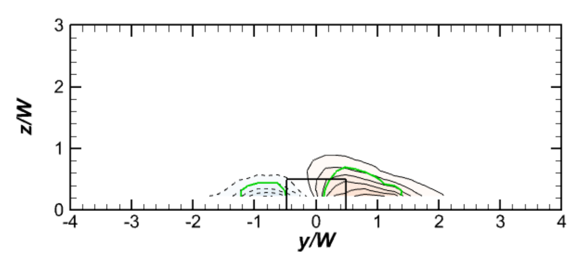

(f) α = 15°

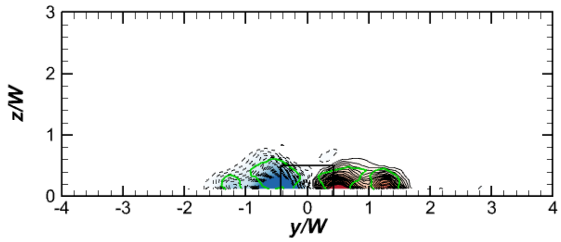

(c) α = 30°

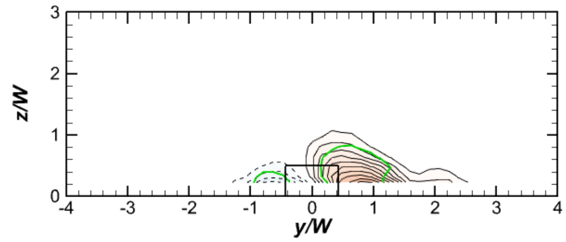

(g) α = 30°

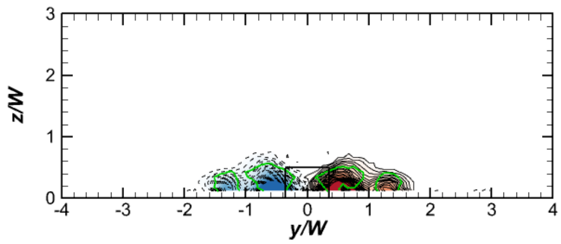

(d) α = 45°

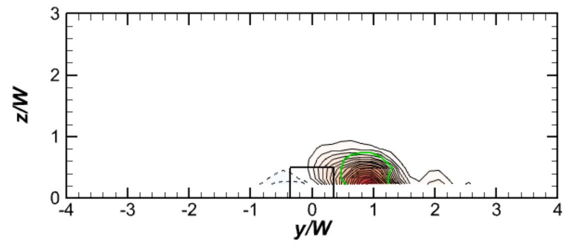

(h) α = 45°

Figure 4.21. Mean streamwise vorticity field (contours of $\omega_x W/U_\infty$) in the cross-stream *y-z* plane with solid green contour lines corresponding to Q = 0.002 (identifying streamwise vortices) for a finite square prism of AR = 0.5: (a) α = 0º, (b) α = 15º, (c) α = 30º, (d) α = 45º at Re = 7.3×10^4, x/W = 3, δ/W = 0.6; and a 3D rectangular flat plate of AR = 0.5: (e) α = 0º, (f) α = 15º, (g) α = 30º, (h) α = 45º from the present experiments, Re = 3.8×10^4, x/W = 6, δ/W = 1.14. Solid black lines and red coloring represent positive (CCW) vorticity. Dashed black lines and blue coloring represent negative (CW) vorticity.

Regarding the wake boundary, the square prism of AR= 0.5 shows a single peak similar to the flat plate while also being characterised by strong downwash in the centerline at α = 0º (Fig. 4.22a). However, when rotating the square prism to α = 15º (Fig. 4.22b) this single peak divides in two asymmetrical ones with the tallest one on the –y side of the wake. At α = 30º (Fig 4.22c) the dual peaks start regaining their symmetry finally becoming the same size at α = 45º (Fig. 4.22d).

The flat plate keeps that single peak and it shifts to the +y side of the wake as α progresses with increasing asymmetry from α = 0º to 45º (Fig. 4.22e-h). Further analysis on larger α was given in Section 4.3.1.

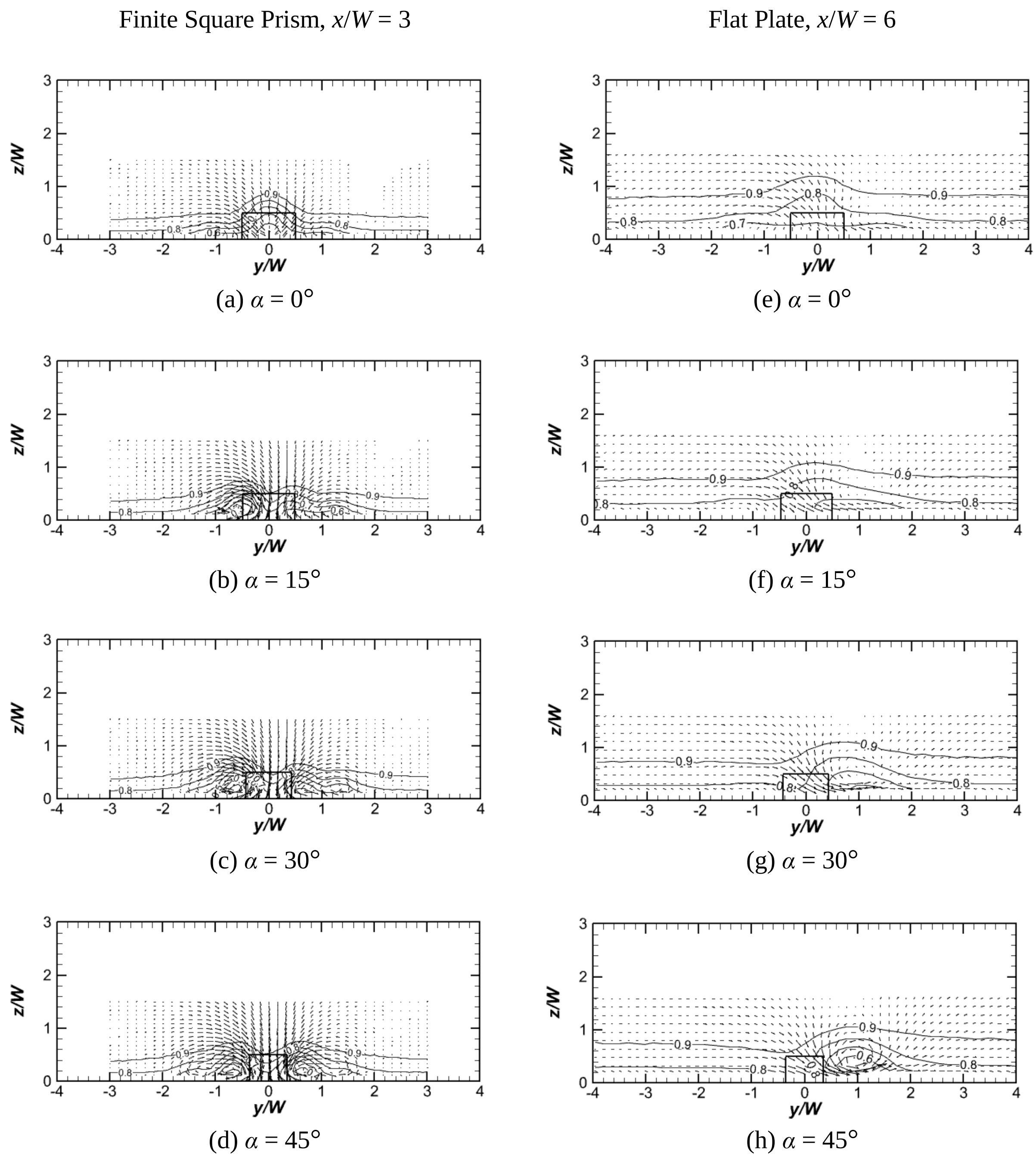

Figure 4.22. Mean velocity vector field (showing velocity vector components v/U_∞, w/U_∞) with streamwise mean velocity contours (u/U_∞) in the cross-stream y-z plane for a 3D finite square prism of AR = 0.5 (a) α = 0º, (b) α = 15º, (c) α = 30º, (d) α = 45º at Re = 7.3×10^4, x/W = 3, δ/W = 0.6; and a 3D rectangular flat plate of AR = 0.5: (e) α = 0º, (f) α = 15º, (g) α = 30º, (h) α = 45º from the present experiments at Re = 3.8×10^4, x/W = 6, δ/W = 1.14.

The comparison between the wake of a 3D rectangular flat plate of AR = 3 and that of a finite-height square prism of AR = 3 will now be described. Results are shown in Figs. 4.23 and 4.24. The flat plate experiments from the thesis research were conducted at a Reynolds number of Re =

3.8×10^4, a boundary layer thickness of $\delta/W = 1.14$, and with measurements performed downstream at $x/W = 6$. The finite-height square prism experiments from [11] had a Reynolds number of Re = 3.7×10^4 (essentially the same), a boundary layer thickness of $\delta/W = 1.5$ (a thicker boundary layer), and with measurements performed downstream at $x/W = 8$ (farther downstream).

In the vertical y-z plane when $\alpha = 0°$, the flat plate of $AR = 3$ (Fig. 4.23e) has a set of symmetrical tip vortices contiguous with ground plane vortex structures on each side of the centerline ($y/W = 0$) and some small induced vorticity with opposite rotation. In contrast, the finite square prism (Fig. 4.23a) has two symmetrical weaker tip vortices and a set of ground plane vortices completely detached and distinguishable, also with a smaller quantity of induced vorticity. Both the tip and ground plane vortex structures of the finite square prism seem to be farther apart from the centerline than those of the flat plate. This variation could be partly explained by the difference in distance downstream at which the wake measurements were performed ($x/W = 6$ for the flat plate and $x/W = 8$ for the finite square prism), which gives the finite square prism's vortices greater opportunity to diffuse and spread. The wake boundary of the finite square prism (Fig. 4.24a) shows two peaks in the velocity contour line, while the wake of the flat plate (Fig. 4.24e) shows a single symmetrical peak of the velocity contour line, a difference perhaps caused by the presence of the top face of the afterbody (x-y plane) of the prism (that is absent for the thin flat plate). Both bluff bodies indicate strong downwash located at the centerline ($y/W = 0$) caused by the symmetrical streamwise vortex structures.

When rotating both the finite square prism and flat plate to $\alpha = 15°$ (Fig. 4.23b and Fig. 4.23f) they show a similar tendency, with the CCW tip vortex (on the $+y$ side of the wake) growing and positioning itself upwards and leftwards creating some space in between its corresponding ground plane vortex structure at $+y$. At the same time, the CW tip vortex loses strength and becomes positioned downwards and rightwards becoming contiguous with its respective ground plane vortex on the $-y$ side of the wake. The main difference up to this point, aside from the position of the main vortex structures, is the growing presence of the CW induced vorticity on the $+y$ side of the wake, which is present only in the wake of the flat plate. The prism shows its largest wake boundary asymmetry between $\alpha = 10°$ and $15°$ (Fig. 4.24b) which corresponds to a critical incidence angle [11] [12] characterized by the lowest C_D, the highest magnitude of C_L, and the largest St.

Between α = 15° and α = 30° the differences between the wakes behind both bluff bodies become more noticeable, with the square prism (Fig. 4.24c) starting to recover its wake symmetry with adjoining sets of tip and ground vortex structures (Fig. 4.23c), while the flat plate (Fig. 4.24g) shows a larger wake asymmetry following the same pattern as in α = 0° to 15°.

Finite Square Prism, x/W = 8

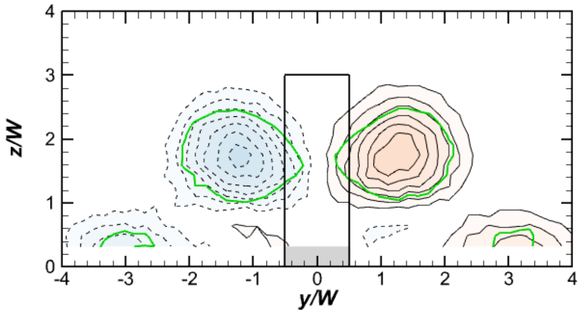

(a) α = 0°

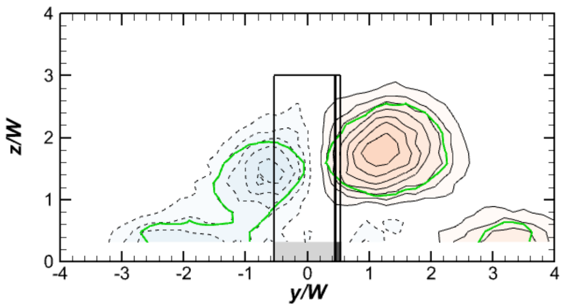

(b) α = 15°

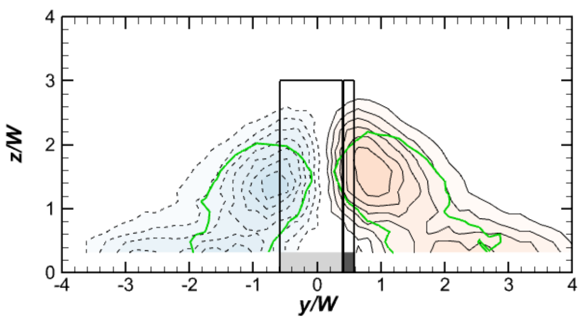

(c) α = 30°

Flat Plate, x/W = 6

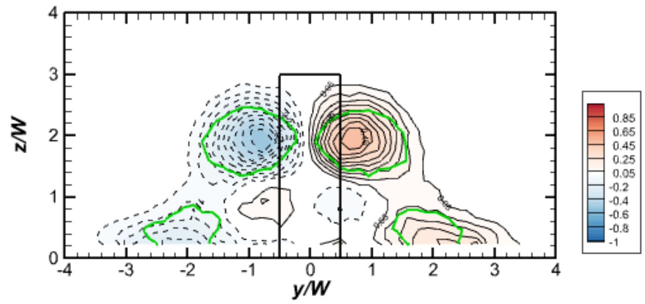

(e) α = 0°

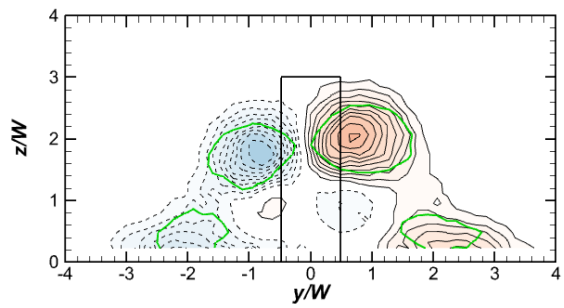

(f) α = 15°

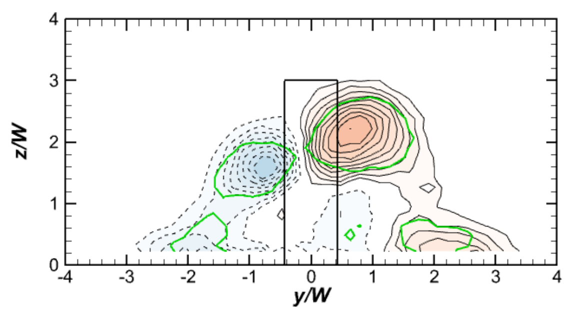

(g) α = 30°

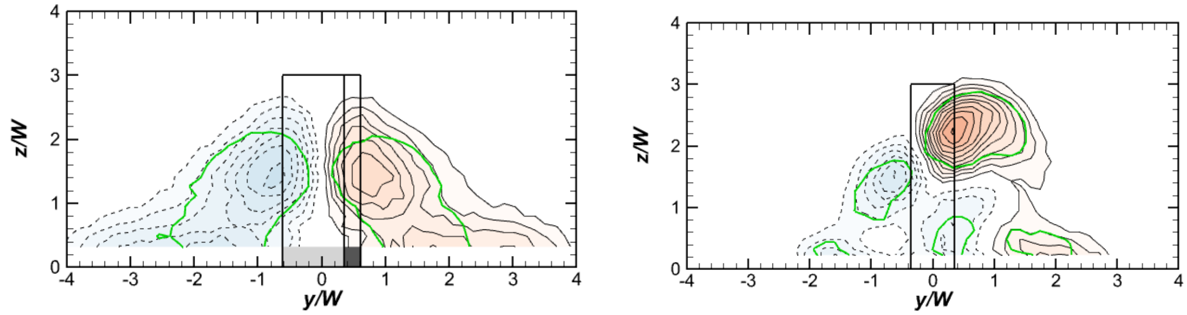

(d) α = 45° (h) α = 45°

Figure 4.23. Mean streamwise vorticity field (contours of $\omega_x W/U_\infty$) in the cross-stream *y-z* plane with solid green contour lines corresponding to Q = 0.002 (identifying streamwise vortices) for a finite square prism of AR = 3: (a) α = 0º, (b) α = 15º, (c) α = 30º, (d) α = 45º at Re = 7.3×10^4, x/W = 8, δ/W = 0.6; and a 3D rectangular flat plate of AR = 0.5: (e) α = 0º, (f) α = 15º, (g) α = 30º, (h) α = 45º from the present experiments, Re = 3.8×10^4, x/W = 6, δ/W = 1.14. Solid black lines and red coloring represent positive (CCW) vorticity. Dashed black lines and blue coloring represent negative (CW) vorticity.

Something to point out about the finite square prism is that it can be rotated only up to α = 45° (Fig. 4.23d and Fig. 4.24d) due to the symmetric features of the bluff body; the wake development is mirror like with larger α. The thin 3D flat plate does not present these symmetric features when varying α due to the lack of afterbody and symmetry to its cross-section. This means the flat plate can rotate up α = 90° and have a distinct wake progression. That being said, at α = 45° the finite square prism shows a symmetrical wake (Fig. 4.24d) and the tip vortices (Fig. 4.23d) at this incidence angle elongate in the vertical direction becoming contiguous with the ground plane vortex structures. On the other hand, the 3D flat plate (Fig. 4.23h) shows the same continuous trend with the positive CCW tip vortex continuing to move upwards and leftwards while detaching from the same side ground plane vortex. The negative CW tip vortex has continued to move downwards while reducing in strength and adjoining the increasing CW induced vorticity located on the +*y* side of the plane.

It should be noted the largest recirculation region for the finite square prism is achieved with this incidence angle, α = 45°. It is assumed that the longest recirculation zone for the 3D flat plate, when considering the plate's geometry and how the flow separates from its two vertical edges and the upper edge, occurs at α = 0º.

The afterbody shape and symmetric cross-sectional shape of the finite square prism constricts the wake development at α = 45° to symmetrical streamwise vortex structures. The lack thereof for the thin 3D flat plate allows its streamwise vortex structures to develop further into a single strong tip vortex with a behaviour similar to a finite wing on an airplane, and allowing it to become a streamlined body at large incidence angles (α = 80° to 90°) based on the steep drop of maximum downwash w/U_∞ (Fig. 4.17) and maximum streamwise vorticity $\omega_x W/U_\infty$ (Fig. 4.18) of the CCW tip vortex.

Finite Square Prism, x/W = 8 | Flat Plate, x/W = 6

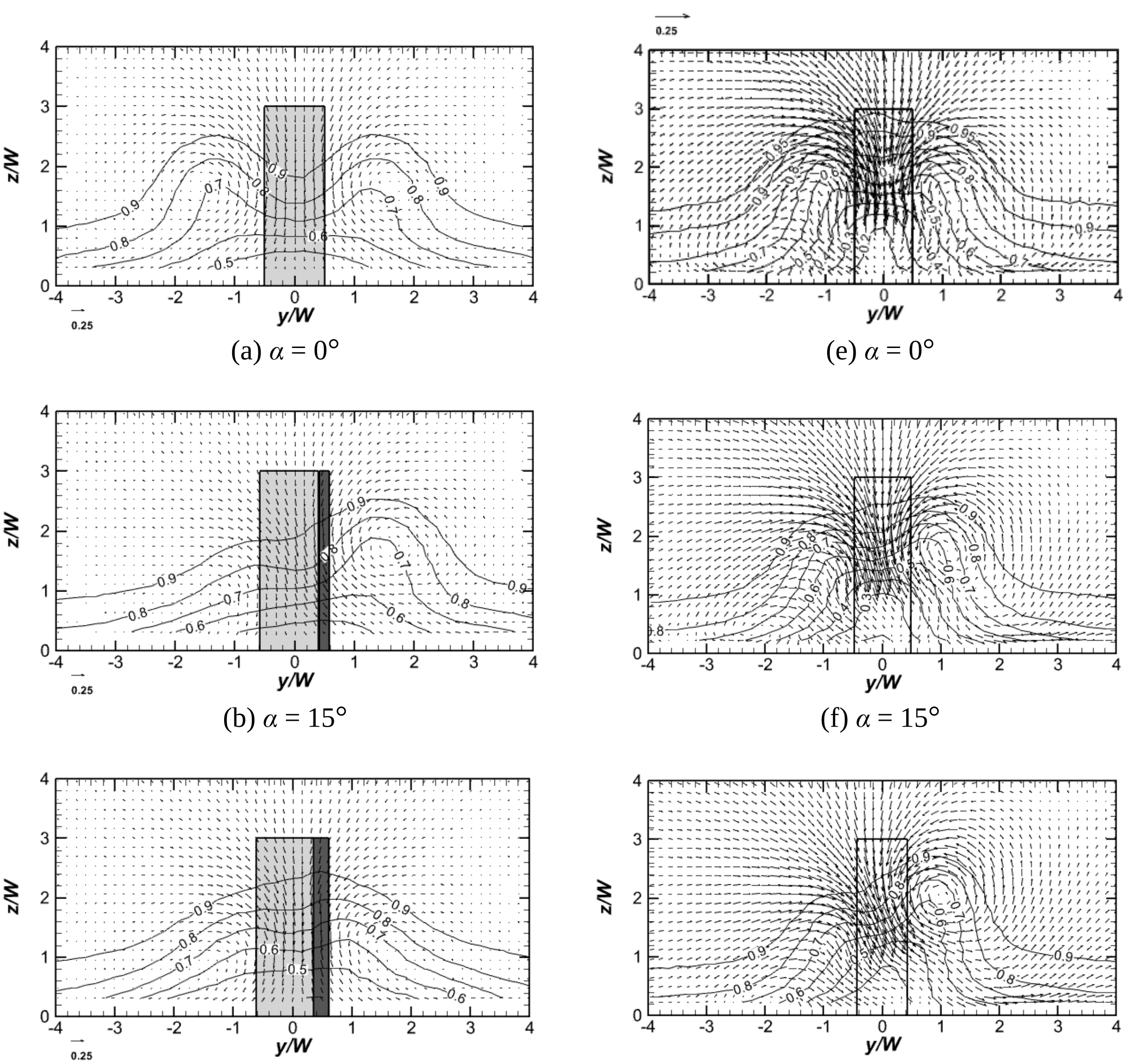

(a) α = 0° (e) α = 0°

(b) α = 15° (f) α = 15°

(c) α = 30° (g) α = 30°

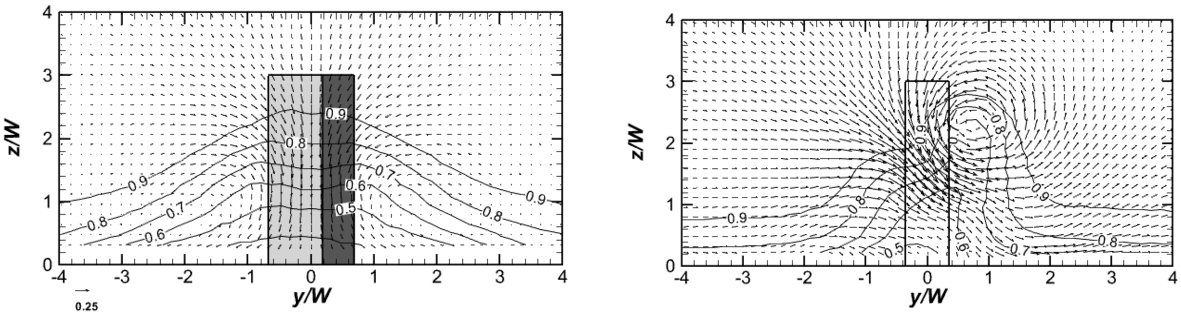

(d) α = 45°　　　(h) α = 45°

Figure 4.24. Mean velocity vector field (showing velocity vector components v/U_∞, w/U_∞) with streamwise mean velocity contours (u/U_∞) in the cross-stream *y*-*z* plane for a 3D finite square prism of $AR = 3$ (a) $\alpha = 0$º, (b) $\alpha = 15$º, (c) $\alpha = 30$º, (d) $\alpha = 45$º at Re = = 3.7×10^4, $x/W = 8$, $\delta/W = 1.5$ from [11]; and a 3D rectangular flat plate of $AR = 3$: (e) $\alpha = 0$º, (f) $\alpha = 15$º, (g) $\alpha = 30$º, (h) $\alpha = 45$º from the present experiments at Re = 3.8×10^4, $x/W = 6$, $\delta/W = 1.14$.

Chapter 5 - Conclusions and Recommendations

5.1 Summary

The purpose of the present research was to learn the effects of aspect ratio (*AR*) and incidence angle (α) on the mean wake of surface-mounted three-dimensional (3D) rectangular flat plates. Of specific interest were the mean streamwise vortex structures and the recirculation zone behind the flat plate.

This study examined the flow around 3D rectangular flat plates of *AR* = 0.5, 1, 2 and 3 with an incidence angle domain of α = 0º to 90º. This research was carried out at a constant Reynolds number of Re = 3.8×10^4 based on the width (*W*) of the plates and the freestream velocity, and a constant relative boundary layer thickness on the ground plane of δ/W = 1.14. Time-averaged velocity measurements in the wakes of the plates were made with a seven-hole pressure probe (the experimental approach was described in Chapter 3). Wake measurements were executed in the form of two types of vertical planes which included vertical *x*-*z* planes along the centreline of the flow (y/W = 0) and vertical *y*-*z* planes at x/W = 6 downstream of the plate.

There are few published experimental or numerical studies of surface-mounted 3D flat plates (as summarized in Chapter 2), and so the data obtained were compared with earlier experiments (in the same wind tunnel, using similar approaches) involving surface-mounted finite-height square prisms [11] [12] [15] and finite-height cylinders [13].

5.2 Conclusions

The first objective of the research was to show the effects of the aspect ratio *AR* and incidence angle α and how they affect the mean wake behind the 3D flat plate. This objective was achieved on account of the experimental setup discussed in Chapter 3 and discussed thoroughly in Chapter 4. The second objective of the research involved comparing the wakes of the 3D flat plates with those of surface-mounted finite-height cylinders and finite-height square prisms of similar aspect ratios, in order to determine some effects of afterbody shape on the mean wake of surface-mounted finite-height bluff bodies; this discussion was found in Chapter 4.

Fulfillment of the proposed objectives led to various conclusions. For flat plates normal to the flow, at $\alpha = 0^{\circ}$:

- The aspect ratio (*AR*) of the flat plate has a noticeable effect on the size and length of the recirculation zone; the streamwise extent of the recirculation zone increases with *AR*.
- The flat plates with the largest *AR* produce the largest velocity deficits, in other words $(u/U_{\infty})_{min}$ becomes smaller when the aspect ratio of the flat plate is increased. A similar trend is present for the case of finite square prisms.
- The flat plates from *AR* = 1 to 3 have a maximum downwash located on the centerline at a height between $z/H = 0.63$ and 0.79 at a streamwise location of $x/W = 0.6$; in contrast, the flat plate of *AR* = 0.5 has its maximum downwash above its height, at $z/H = 1.58$. This result suggests that the plate of *AR* = 0.5 has a distinct wake structure compared to the other plates.
- The aspect ratio influences the number and type of distinguishable complex streamwise vortex structures seen in the wake at $x/W = 6$. For *AR* = 0.5 and 1, a single set of counter rotating vortices are accounted for, while for *AR* = 2 and 3 two sets of main counter rotating vortex structures are identifiable: the pair of tip vortices in the upper part of the wake and the pair of ground plane vortices in the lower part of the wake.
- At $x/W = 6$, the maximum vorticity for the more slender flat plates of *AR* = 2 and 3 is found within the tip vortex structures, which are located above and are distinct from the pair of ground plane vortices. In contrast, for *AR* = 0.5 and 1, the maximum vorticity is found in the core of the single pair of merged tip and ground plane vortices.

For flat plates at an angle of incidence α:

- The relative sizes, strengths, and locations of the streamwise vortex structures, as well as their appearance and existence, change with the incidence angle of the flat plate.
- The total vortex strength at small α increases with *AR*. For *AR* = 0.5 it increases slightly with α up to $\alpha = 55^{\circ}$ and steadily decreases until reaching zero. The vortex strength for *AR* = 1 is consistent up to $\alpha = 35^{\circ}$ where it then shows a similar trend to the smaller flat plate.

Flat plates of $AR = 2$ and 3 behave differently, with a consistent decrease in vortex strength when increasing the incidence angle α.

- The vortex strength difference between the CW and CCW streamwise vortex structures in the wake of the plate behaves in a similar way for all four aspect ratios, with the greatest dissimilarity near $\alpha = 50^{\circ}$.
- The flat plate of $AR = 0.5$ shows some interesting features at $\alpha = 55^{\circ}$ which coincides with the largest wake asymmetry, maximum downwash and upwash, the maximum vorticity concentration, and largest velocity deficit of every incidence angle. It is believed $\alpha = 55^{\circ}$ corresponds to a critical incidence angle for this specific flat plate.
- The flat plate of $AR = 1$ at an incidence angle $\alpha = 70^{\circ}$ denotes interesting flow features that coincide with the largest wake asymmetry, the maximum streamwise vorticity, and the maximum downwash for all incidence angles.
- The flat plate of $AR = 3$ has induced vorticity with opposite rotation from the corresponding tip and ground plane vortices, which is attributed to an effect similar to a corner induced vortex in a channel, where the opposite tip vortices behave like "walls" with a small interaction of the ground plane vortices on the bottom that whirl in the same direction.
- The flat plate of $AR = 3$ shows a particular wake development with increasing incidence angle α. The CCW tip vortex structure overtakes the CW tip vortex (which is also the case for the other aspect ratios), while the ground plane vortex structures (only present for $AR = 2$ and 3) start diminishing in strength and size. The counter-rotating opposite sign induced vorticity (only present for $AR = 3$), while interacting with the CCW tip vortex and the ground plane vortices, creates a vertical "chain" of counter-rotating vorticity. A similar behaviour is seen for the flat plate of $AR = 2$, however it is not as recognizable as in the larger finite flat plate.
- The incidence angle α where the maximum downwash and upwash (w/U_{∞}) reach their peak values increases with the aspect ratio. For the flat plate of $AR = 0.5$ this occurs at $\alpha = 55^{\circ}$ to 60°, for $AR = 1$ this is achieved at $\alpha = 70^{\circ}$, while for $AR = 2$ and 3 this peak is found between $\alpha = 75^{\circ}$ to 80° and $\alpha = 80^{\circ}$, respectively. These incidence angles are also consistent with the occurrence of the peak values of maximum streamwise vorticity. For every case, once the downwash, upwash and streamwise vorticity reach their peak values, they then decrease steadily trending towards zero as α increases to $\alpha = 90^{\circ}$.

- The flat plates of $AR = 1$ to 3 show a similar trend of an increasing minimum streamwise velocity $(u/U_\infty)_{min}$ with escalating incidence angle, most likely due to the reduced front facing area when increasing α. The flat plate of $AR = 0.5$ shows a different trend, however, with a dramatic increase in the velocity deficit at $\alpha = 55^o$ only to follow a similar trend as the other flat plates at larger α. This points to the unique wake structure and behavior for the flat plate of $AR = 0.5$.

When comparing the flat plate to the finite square prism and finite cylinder:

- The maximum length of the recirculation zone, if considered to begin from the leading edge of the body, is practically the same for the finite square prism and the flat plate; however, if the reference point is the bluff body's centerline $(x/W = 0)$, it is longer for the flat plate. The finite cylinder has the smallest recirculation zone of the three bodies considered, and is the only one to exhibit some upwash near the ground plane (for the flat plate and finite square prism, the downwash reaches to the ground plane).
- The wake boundary of the flat plate for every aspect ratio ($AR = 0.5$, 1, 2, 3) contains a single peak; this also is the case for finite square prisms of $AR = 1$ or lower. In contrast, for the finite cylinder and the finite square prism of $AR = 3$, this boundary instead shows two symmetrical peaks, most likely due to the presence of an afterbody.
- The finite square prisms show a stronger separation shear layer encasing the recirculation zone compared to the 3D flat plates, most likely due to the interaction of the separated flow with the free end surface, which is only present due to the afterbody of the prism. The finite cylinder shows the weakest separation shear layer, most likely due to the curved shape of the leading edge of the cylinder's free end surface.
- The finite cylinder of $AR = 3$ does not have the ground plane vortex structures that are seen for the finite square prism and the flat plate, although this might be due to the different measurement locations and lengths of their recirculation zones.
- The finite square prisms ($AR = 0.5$ and 3) show their largest wake asymmetry between $\alpha = 10^o$ and $\alpha = 15^o$, which is considered a critical incidence angle characterized by the lowest C_D, the highest magnitude of C_L, and the largest St. This critical incidence angle is related to the reattachment of one of the separated shear layers onto a side of the prism, a

phenomenon that cannot occur for the thin flat plate. The afterbody of the finite square prism constricts the wake development at α = 45º to symmetrical streamwise vortex structures. The case of the flat plate is different with an increasing asymmetry at larger incidence angles, and a critical incidence angle between α = 55 º and 80 º (as summarized above). For both bluff bodies, however, the flow near the critical incidence angle is characterized by a dominant CCW tip vortex on the +y side of the wake overtaking a reduced CW tip vortex on the –y side of the wake.

- The largest recirculation region for the finite square prism is achieved at α = 45º while it is assumed the longest recirculation zone for the 3D flat plate occurs at α = 0º by considering the plate's geometry and how the flow separates from its two vertical edges.

5.3 Recommendations

To improve the comparison between the wakes of the 3D flat plate with the wakes of the finite square prism and finite cylinder, the latter two bodies need to be studied at additional aspect ratios, including AR = 2 for the finite square prism and AR = 0.5, 1, and 2 for the finite cylinder. Consistent values of Reynolds number, the relative boundary layer thickness, and the measurement locations are also desirable for all the bodies, to aid in comparing the results.

It would also be beneficial to extend the 3D flat plate experiments to higher aspect ratios, such as AR = 5, 7, and 9, where results already exist for the finite square prism and finite cylinder. The challenge in doing so arises from the fabrication of the flat plate test models, which need to be thin enough to discard the afterbody effects but have enough sturdiness so they will not bend or vibrate (and thereby alter the wake behavior). This becomes increasingly difficult when dealing with longer flat plates.

Further studies focusing on the mean drag coefficient C_D, mean lift coefficient C_L, and Strouhal number (dimensionless vortex shedding frequency) St would be considered valuable information to further explain the behaviour of 3D flat plates, which could unravel further understanding on the flow surrounding this bluff body. The force balances currently available at the University of Saskatchewan to measure the forces experienced by the flat plate models are not accurate enough to obtain reasonable results, which is why this approach was omitted in the present research. An alternative could be increasing the overall size of the flat plates in order to increase the force being exerted on the models however, solid wall blockage effects are an important thing to look out for when experimenting in controlled wind tunnel conditions.

The present experiments were all carried out at a single non-tripped boundary layer thickness of $\delta/W \approx 1.14$. The effects of the boundary layer thickness could be explored by varying this flow feature while keeping the other variables constant in order to explore its effects on the wake at different aspect ratios and incidence angles.

Due to time restrictions, the present experiments limited the measured incidence angle to increments of 5°. Smaller angle increments down to 1° could be explored near critical or relevant incidence angles in order to more accurately pinpoint shifts in the wake development.

References

[1] Sheikhnejad, Y., & Gandjalikhan Nassab, S. A. (2021). Enhancement of solar chimney performance by passive vortex generator. Renewable Energy, 169, 437–450. https://doi.org/10.1016/j.renene.2021.01.026

[2] Yang, Y., Ting, D. S. K., & Ray, S. (2020). On flexible rectangular strip height on flat plate heat convection. International Journal of Heat and Mass Transfer, 150, 119269. doi:10.1016/j.ijheatmasstransfer.2019.119269

[3] Ota, T., Takeuchi, E., & Yoshikawa, H. (2002). LES of three-dimensional turbulent separated and reattached flow around a surface-mounted square plate, presented at ASME 2002 Fluids Engineering Division Summer Meeting, Montreal, QC, 2002. doi: 10.1115/FEDSM2002-31096

[4] Yoshikawa, H., Shimizu, K., & Ota, T. (2003). Numerical simulation of three-dimensional separated flow and heat transfer around a surface-mounted square plate. Proceedings of the ASME/JSME 2003 4th Joint Fluids Summer Engineering Conference. Volume 2: Symposia, Parts A, B, and C. Honolulu, Hawaii, USA. July 6–10, 2003. pp. 863-870. ASME. https://doi.org/10.1115/FEDSM2003-45089

[5] Hamed, A. M., Pagan-Vazquez, A., Khovalyg, D., Zhang, Z., & Chamorro, L. P. (2017). Vortical structures in the near wake of tabs with various geometries. Journal of Fluid Mechanics, 825, 167–188. doi:10.1017/jfm.2017.384

[6] Tobin, N., & Chamorro, L. P. (2018). Wakes behind surface-mounted obstacles: impact of aspect ratio, incident angle, and surface roughness. Physical Review Fluids, 3(3), 033801. doi: ARTN 033801 10.1103/PhysRevFluids.3.033801

[7] Wang, H., & Takle, E. S. (1996). On shelter efficiency of shelterbelts in oblique wind. Agricultural and Forest Meteorology, 81(1-2), 95–117. doi: 10.1016/0168-1923(95)02311-9

[8] Tobin, N., Hamed, A. M., & Chamorro, L. P. (2017). Fractional flow speed-up from porous windbreaks for enhanced wind-turbine power. Boundary-Layer Meteorology, 163(2), 253–271. https://doi.org/10.1007/s10546-016-0228-8

[9] Jin, Y. Q., Kim, J. T., Hong, L., & Chamorro, L. P. (2018). Flow-induced oscillations of low-aspect-ratio flexible plates with various tip geometries. Physics of Fluids, 30(9), 097102. doi: Artn 097102 10.1063/1.5046950

[10] Sakamoto, H., & Arie, M. (1983). Flow around a normal plate of finite width immersed in a turbulent boundary-layer. Journal of Fluids Engineering, 105(1), 98-104. doi: Doi 10.1115/1.3240950

[11] Unnikrishnan, S., Ogunremi, A., & Sumner, D. (2017). The effect of incidence angle on the mean wake of surface-mounted finite-height square prisms. International Journal of Heat and Fluid Flow, 66, 137–156. doi: 10.1016/j.ijheatfluidflow.2017.05.012

[12] Sumner, D., Unnikrishnan, S., Teng, M., Beitel, A., Das, A., & Fulton, M. (2016). The mean wake of low-aspect-ratio surface-mounted finite-height square prisms and the effects of incidence angle, presented at 8th International Colloquium on Bluff Body Aerodynamics and Applications, Northeastern University,2016. Boston, MA:BBAA Vlll.

[13] Sumner, D., Heseltine, J. L., & Dansereau, O. J. (2004). Wake structure of a finite circular cylinder of small aspect ratio. Experiments in Fluids, 37(5), 720–730. https://doi.org/10.1007/s00348-004-0862-7

[14] da Silva, B. L., Chakravarty, R., Sumner, D., & Bergstrom, D. J. (2020). Aerodynamic forces and three-dimensional flow structures in the mean wake of a surface-mounted finite-height square prism. International Journal of Heat and Fluid Flow, 83, 108569. doi: 10.1016/j.ijheatfluidflow.2020.108569

[15] da Silva, B. L., Sumner, D., & Bergstrom, D. J. (2021). Mean and dynamic aspects of the wakes of a surface-mounted cube and block. Journal of Fluids Engineering, 144(1). https://doi.org/10.1115/1.4051428

[16] Beitel, A., Heng, H., & Sumner, D. (2019). The effect of aspect ratio on the aerodynamic forces and bending moment for a surface-mounted finite-height cylinder. Journal of Wind Engineering and Industrial Aerodynamics, 186, 204–213. doi: 10.1016/j.jweia.2019.01.009

[17] Fail, R., Eyre, R. C. W., & Lawford, J. A. (1959). Low-speed experiments on the wake characteristics of flat plates normal to an air stream. Aeronautical Research Council Reports and Memoranda. No.3120. London: HMSO.

[18] Fage, A. & Johansen, F. C. (1927).On the flow of air behind an inclined flat plate of infinite span. The Royal Society Publishing. A 116(773), 170–197. https://doi.org/10.1098/rspa.1927.0130

[19] Sakamoto, H., Moriya, M., & Arie, M. (1975). A study on the flow around bluff bodies immersed in turbulent boundary layers : Part 1, on the form drag of a normal plate. Bulletin of the JSME, 18(124), 1126–1133. doi:10.1299/jsme1958.18.1126

[20] Sakamoto, H., Moriya, M., & Arie, M. (1977). A study on the flow around bluff bodies immersed in turbulent boundary layers : Part 2, the pressure forces acting on inclined plates. Bulletin of the JSME, 20(139), 71–78. doi:10.1299/jsme1958.20.71

[21] Mazharoğlu, Ç., & Hacışevki, H. (1999). Coherent and incoherent flow structures behind a normal flat plate. Experimental Thermal and Fluid Science, 19(3), 160–167. doi:10.1016/s0894-1777(99)00017-5

[22] Afgan, I., Benhamadouche, S., Han, X., Sagaut, P., & Laurence, D. (2013). Flow over a flat plate with uniform inlet and incident coherent gusts. Journal of Fluid Mechanics, 720, 457–485. doi: 10.1017/jfm.2013.25

[23] Letchford, C. W., & Holmes, J. D. (1994). Wind loads on free-standing walls in turbulent boundary layers. Journal of Wind Engineering and Industrial Aerodynamics, 51(1), 1–27. doi:10.1016/0167-6105(94)90074-4

[24] Good, M. C., & Joubert, P. N. (1968). The form drag of two-dimensional bluff-plates immersed in turbulent boundary layers. Journal of Fluid Mechanics, 31(03), 547–582. doi:10.1017/s0022112068000327

[25] Najjar, F. M., & Vanka, S. P. (1995). Effects of intrinsic three-dimensionality on the drag characteristics of a normal flat plate. Physics of Fluids, 7(10), 2516–2518. doi:10.1063/1.868698

[26] Jin, Y. Q., Kim, J. T., Fu, S. F., & Chamorro, L. P. (2019). Flow-induced motions of flexible plates: Fluttering, twisting and orbital modes. Journal of Fluid Mechanics, 864, 273–285. doi: ARTN 074301 PII S0022112019000405 10.1017/jfm.2019.40

[27] Yamada, H., & Osaka, H. (1991). Effects of the shedding vortices on the grand wall flow behind a three-dimensional protuberance. Journal of the Visualization Society of Japan, 11(Supplement2), 161–164. doi:10.3154/jvs.11.Supplement2_161

[28] Yamada, H., Yamane, T., & Osaka, H. (1993). Vortex structure behind a square plate protuberance standing on a flat ground wall. Visualization study in the case of a laminar boundary layer. Transactions of the Japan Society of Mechanical Engineers Series B, 59(559), 677–683. doi:10.1299/kikaib.59.677. (In Japanese).

[29] Okamoto, S. (1985). Experimental investigation of flow past bluff body of square section placed on ground plane. Bulletin of the JSME, 28(239), 815–823.

[30] Sumner, D., & Reitenbach, H. K. (2019). Wake interference effects for two finite cylinders: A brief review and some new measurements. Journal of Fluids and Structures, 89, 25–38. https://doi.org/10.1016/j.jfluidstructs.2019.02.004

[31] White, H. F. (2003). Fluid Mechanics, 5th Edition, McGraw-Hill, New York.

[32] Zilliac, G. G. (1993). Modelling, calibration, and error analysis of seven-hole pressure probes. Experiments in Fluids, 14(1-2), 104–120. doi:10.1007/bf00196994

[33] Sumner, D. (2002). A comparison of data-reduction methods for a seven-hole probe. Journal of Fluids Engineering, 124(2), 523–527. doi:10.1115/1.1455033

[34] Bryer, D.W., Pankhurst, R.C. (1971). Pressure-probe methods for determining wind speed and flow direction. London, UK: Her Majesty's Stationery Office.

[35] Datametrics, (1982a). Instruction Manual. Type 600 Barocel Pressure Sensor. Datametrics-Dresser Industries, Inc., Wilmington, MA, USA.

[36] Datametrics, (1982b). Instruction Manual. Type 590 Barocel Pressure Sensor. Datametrics-Dresser Industries, Inc., Wilmington, MA, USA.

[37] Chue, S. H. (1975). Pressure probes for fluid measurement. Progress in Aerospace Sciences, 16(2), 147–223. doi:10.1016/0376-0421(75)90014-7

[38] Scanivalve (2014). Model ZOC17 Temperature Compensated Electronic Pressure Scanning Module, Data Sheet No. G447. Scanivalve Corporation, Liberty Lake, WA, USA

[39] Bell, S. (1999). The Beginner's Guide to the Uncertainty of Measurement, Good Practice Guide 11. National Physical Laboratory, Teddington, Middlesex, UK.

[40] Sumner, D., Rostamy, N., Bergstrom, D.J., Bugg, J.D., (2017). Influence of aspect ratio on the mean flow field of a surface-mounted finite-height square prism. International Journal of Heat and Fluid Flow, 65, 1–20. doi: 10.1016/j.ijheatfluidflow.2017.02.004

[41] Sumner, D. (2013). Flow above the free end of a surface-mounted finite-height circular cylinder: A review. Journal of Fluids and Structures, 43, 41–63. https://doi.org/10.1016/j.jfluidstructs.2013.08.007

[42] Zhao, J., Cai, W., & Jiang, Y. (2019). Study on corner vortex enlarging process of 2D square Rayleigh-Bénard cells filled with air in transient states. International Journal of Heat and Mass Transfer, 129, 599–609. doi:10.1016/j.ijheatmasstransfer.2018.09.095

[43] Hunt, J. C. R., Wray, A. A. & Moin, P. (1988) Eddies, stream, and convergence zones in turbulent flows. Center for Turbulence Research Report CTR-S88, pp. 193–208.

Appendix A – Experimental Plan

A map of the experimental plan for the thesis research experiments is shown in Table A.1. The map summarizes the vertical cross-stream (*y*-*z*) planes where velocity measurements were made for every flat plate used in the present study (AR = 0.5, 1, 2, and 3). Table A.1 also contains every measured combination of incidence angle α (varying from 0º to 90º in the CW direction) and streamwise location x of the measurement planes (x/W = 2, 4, and 6), as well as the type of grid used in each experiment.

Table A.1 Map with every combination of incidence angle (α) and streamwise location (x/W) for every flat plate in the present experimental research. The letters A-K refer to the grid size (see Table A.2) used for each experiment.

		α																		
	x =	0°	5°	10°	15°	20°	25°	30°	35°	40°	45°	50°	55°	60°	65°	70°	75°	80°	85°	90°
AR = 0.5	*2W*	B			B			B			B			B			B			
	4W	B	B	B	B			B			B			B			B			
	6W	A	A	A	A	B	B	A	B	B	A	B	B	A	B	B	A	B	B	B
AR = 1	*2W*	C									C									
	4W	C	C	C	C	C	C	C			C			C			C			
	6W	C	E	E	E	E	E	E	E	E	D	E	E	E	E	E	D	E	E	
AR = 2	*2W*																			
	4W	F			F			F			F			F			F			F
	6W	F			F			F		F	F	F	F	F	F	F	F	F	F	F
AR = 3	*2W*										I			H			H			
	4W	J						J			J			J			J			
	6W	K			J			J			K	J	J	J	J	J	J	J	G	G

For every flat plate the measurements at x/W = 6 were outside (downstream of) the recirculation zone, ensuring a more complete set of data with smaller incidence angle increments of 5º. Some of the low incidence angles for the more slender flat plates (AR = 2, 3) were not studied in order to comply with the experimental research time restrictions; the slow development of the wake with incidence angles below 45º was also a major reason why larger increments in α were used in this range. Measurements at x/W = 4 and x/W = 2 for flat plates of AR = 1, 2, and 3 were mostly (but not all) outside (downstream of) the recirculation zone, which is why some of them were regarded as incomplete data sets (the seven-hole pressure probe, which was used to make all of the wake measurements, could not measure in regions of reverse flow). This was not the case with AR = 0.5 which showed complete data sets even at x/W = 4.

Table A.2 details the *y-z* dimensions of every grid used in the wind tunnel experiments (A-K) in terms of the flat plate's width *W*. The table also includes the number of grid points used in each experiment with the approximate testing time for each type of grid. Different grid sizes were determined and adjusted gradually with the help of the experimental information in order to find a middle ground between capturing complete velocity fields and reducing the testing time of the seven-hole probe.

Table A.2. Various grid sizes used in the present experimental research (A-K) in terms of the characteristic width of the plate (*W*), number of grid points, and the approximate testing time.

Grid Type	Height	Width		Grid points	Testing time (Hrs)
	Z+	Y+	Y-		
Type A	1.5W	4W	4W	612	2.2
Type B	1.5W	3W	3W	468	1.7
Type C	2.5W	3.5W	3.5W	720	2.6
Type D	2.5W	3.5W	4.5W	816	2.9
Type E	2.5W	4W	3.5W	768	2.8
Type F	3W	4W	4W	969	3.5
Type G	4W	2.5W	2.5W	825	3.0
Type H	4W	3W	3W	975	3.5
Type I	4W	3.5W	3.5W	1125	4.1
Type J	4W	4W	4W	1275	4.6
Type K	4.5W	5W	5W	1764	6.4